

Anisotropic structures and mechanical properties of
mixed alkali metaphosphate glasses

Jun Endo

February 2022

Anisotropic structures and mechanical properties of
mixed alkali metaphosphate glasses

Jun Endo

Doctoral Program in Engineering Sciences
Subprogram in Materials Science

Submitted to the
Degree Programs in Pure and Applied Sciences of the
Graduate School of Science and Technology
in Partial Fulfillment of the Requirements
for the Degree of Doctor of Philosophy in
Engineering

at the

University of Tsukuba

Table of Contents

Chapter 1: Introduction	1
1.1 Applications and control methods of properties of oxide glasses	1
1.2 Structures of oxide glasses	8
1.3 Previous studies on oxide glasses with anisotropic structures	12
1.3.1 Formation of anisotropic structures in oxide glasses	12
1.3.2 Huge shrinkage due to entropic elasticity of anisotropic (Li,Na,K,Cs)PO ₃ glass	13
1.4 The objective of this thesis	18
1.5 The composition of this thesis	19
References	19
Chapter 2: Structural investigation of alkali metaphosphate glasses for significant anisotropy by analysis of ³¹P MAS NMR, Raman, and FTIR spectra, and DFT calculations	23
2.1 Introduction	23
2.2 Experimental Procedure	23
2.3 Results and Discussion	27
2.3.1 Determination of local structure by analysis of ³¹ P MAS NMR spectra	27
2.3.2 Determination of local structure by analysis of Raman spectra	28
2.3.3 Determination of local structure by analysis of FTIR spectra in the mid-infrared region	32
2.3.4 Determination of the distribution of force constant (F_{M-O}) by analysis of FTIR spectra in the far-infrared region	35
2.3.5 DFT calculations of Raman and IR spectra	37
2.3.6 Structural features of mixed alkali metaphosphate glass	45
2.4 Conclusions	50
References	51
Chapter 3: Relaxation of anisotropic alkali metaphosphate glass	53
3.1 Introduction	53
3.2 Experimental procedure	53
3.3 Results and Discussion	56
3.4 Conclusions	63
References	64

Chapter 4: Unusual indentation behavior of alkali metaphosphate glass above the glass transition temperature	65
4.1 Introduction	65
4.2 Experimental procedure	65
4.3 Results	69
4.4 Discussion	71
4.5 Conclusions	77
References	77
Chapter 5: Mechanical properties of anisotropic metaphosphate glass	79
5.1 Introduction	79
5.2 Experimental Procedure	79
5.3 Results	82
5.4 Discussion	85
5.4.1 Increase in fracture strength	85
5.4.2 Increase in Young's modulus	87
5.5 Conclusions	92
References	92
Chapter 6: Summary and Conclusions	94
Achievements	102
Acknowledgment	103

Chapter 1: Introduction

1.1 Applications and control methods of properties of oxide glasses

Oxide glasses are used in a wide range of fields such as window glasses, substrates and cover materials for display devices, and optical components. The reason why oxide glasses can be applied to various applications is that the properties and shapes of oxide glasses can be controlled with a high degree of freedom.

Properties of oxide glasses are mainly controlled by optimization of glass compositions. **Table 1.1** shows examples of typical oxide glass compositions for each application that have already been put to practical use [1–5].

Table 1.1 Typical oxide glass compositions for each application that have already been put to practical use. M and M' are alkali and alkaline earth elements, respectively [1–5].

Applications	Name of glass	Main components
<ul style="list-style-type: none"> • Optical fibers • Photomasks for photolithography 	Silica glass	• SiO ₂
<ul style="list-style-type: none"> • Window glasses for buildings and vehicles 	Soda-lime glass	• SiO ₂ –CaO–Na ₂ O
<ul style="list-style-type: none"> • Cover glasses for smartphones and tablet computers 	Aluminosilicate glass	• SiO ₂ –Al ₂ O ₃ –Na ₂ O
<ul style="list-style-type: none"> • Glass substrates for liquid crystal displays 	Alumino-borosilicate glass	• SiO ₂ –Al ₂ O ₃ –B ₂ O ₃ –M'O
<ul style="list-style-type: none"> • Heat-resistant glasses • Glasses for vitrification of nuclear waste 	Borosilicate glass	• SiO ₂ –B ₂ O ₃ –Na ₂ O
<ul style="list-style-type: none"> • Sealing glasses 	Borate glass	• B ₂ O ₃ –PbO–ZnO
<ul style="list-style-type: none"> • Optical filters • Rare-earth ion host materials for laser 	Phosphate glass	• P ₂ O ₅ –Al ₂ O ₃ –M'O • P ₂ O ₅ –Al ₂ O ₃ –M ₂ O–M'O

Phosphate glasses for achromatic optical elements and dispersants in clay processing and pigment manufacturing were developed about 100 years ago and in the 1950s, respectively [6]. Phosphate glasses recently have been studied for various applications i.e., materials for laser, sealing, nuclear waste storage, and healing of the human body.

Phosphate glasses for laser: **Figure 1.1** shows the development of commercial laser glass [7]. Commercial laser glasses changed from initial silicate-based glasses to phosphate-based glasses [7]. Phosphate glasses can contain a higher concentration of laser-active rare-earth ions (Er³⁺, Yb³⁺, Nd³⁺, etc.) without clustering compared to silica glass, phosphate glass fibers are used for laser sources and amplifiers [8,9]. The clusters cause quenching of luminescence due to energy transfer between neighboring ions [10]. The use of highly-doped phosphate glasses enables the fabrication of compact devices such as amplifiers

with lengths of only a few centimeters [11]. In addition, since phosphate glasses have a large stimulated emission cross section and low nonlinear refractive index, Nd^{3+} -doped phosphate glasses are used for high-power laser applications such as inertial confinement fusion facilities [12–14].

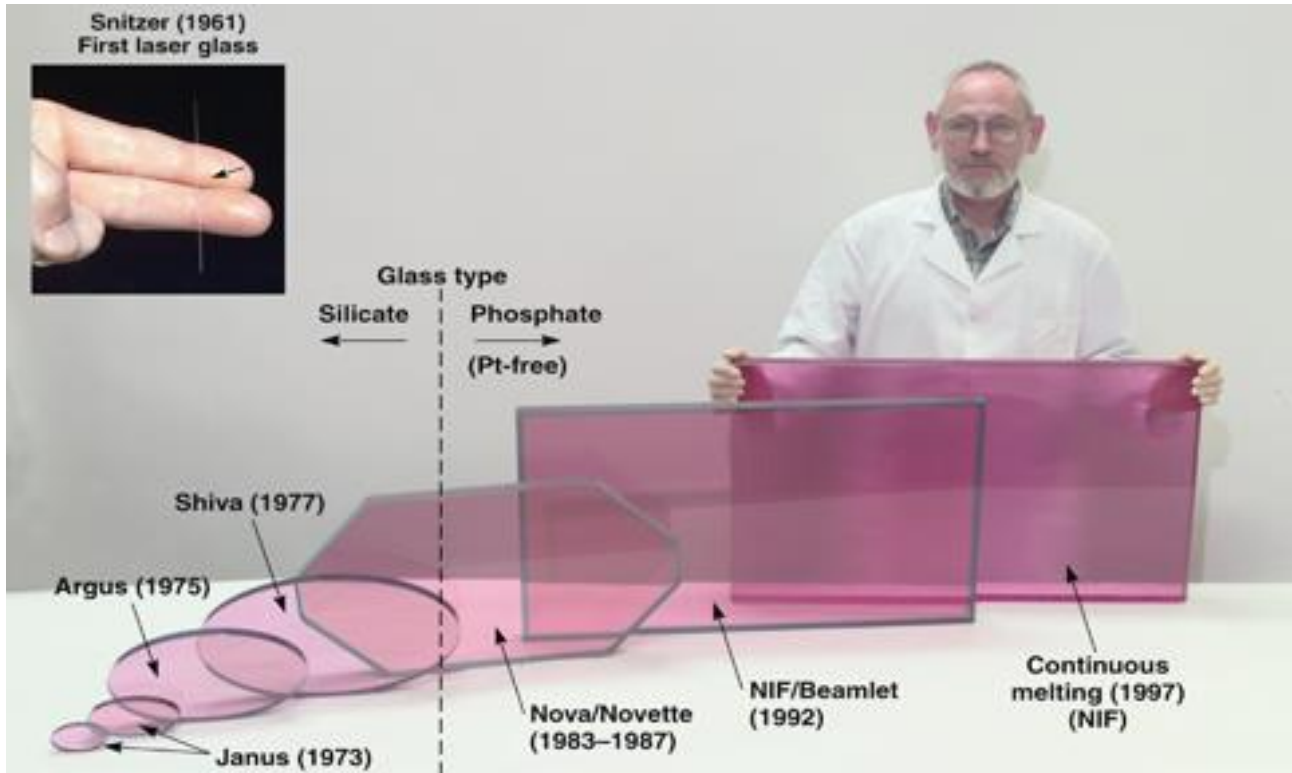


Fig. 1.1 The evolution of laser glass over roughly 40 years from the first silicate glass of Snitzer to the meter-class slabs produced for inertial confinement fusion research at the Lawrence Livermore National Laboratory. Reproduced with permission from Ref. [7]. Copyright 2010, The American Ceramic Society and Wiley Periodicals, Inc.

Phosphate glasses for sealing: Since glasses containing a large amount of lead have a low melting point, the glasses have been used as sealing materials for various commercial applications. Lead-free sealing glasses are necessary because lead deteriorates human health and the environment. Phosphate glasses such as $\text{SnO-ZnO-P}_2\text{O}_5$, $\text{SnO-MgO-P}_2\text{O}_5$, and $\text{SnO-CaO-P}_2\text{O}_5$ systems are studied as lead-free sealing glasses [15–18].

Phosphate glasses for nuclear waste storage: Borosilicate glasses are used for vitrification of nuclear waste because the glasses have excellent thermal shock resistance and chemical durability. In the vitrification process, the nuclear wastes are mixed with the borosilicate glasses, melted at a high temperature, and then sealed in a vitrification container. **Figure 1.2** shows an example of the vitrification process [19]. Iron phosphate glasses are studied for a host matrix of nuclear waste disposal process due to higher solubility of heavy metals with greater waste loadings at a lower melting temperature (950–1100°C) compared to borosilicate glasses (1150–1200°C) [20]. The low melting temperature of phosphate glasses contributes to

the reduction of volatilization of radioactive elements.

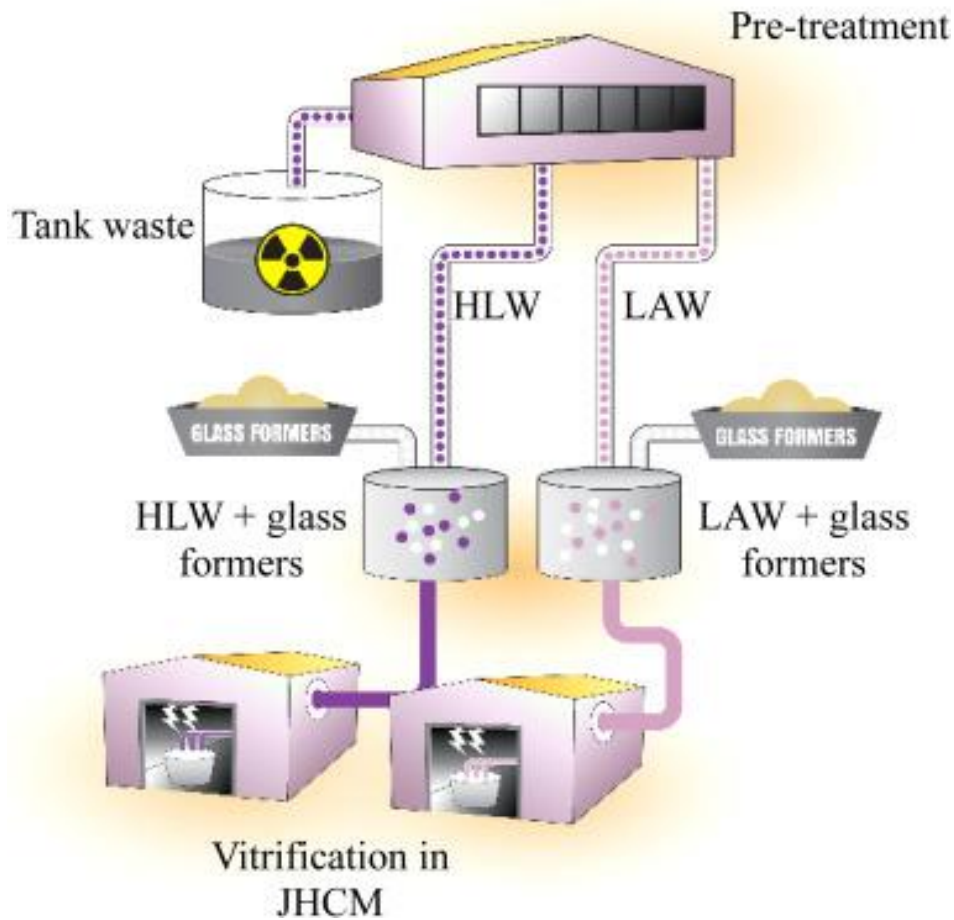


Fig. 1.2 Schematic of the vitrification process to be implemented at Hanford site. HLW, LAW, and JHCM are high-level waste, low activity waste, and Joule-heated ceramic melters, respectively. Reproduced with permission from Ref. [19]. Copyright 2019, Elsevier B.V.

Phosphate glasses for healing of the human body: Since bioactive glasses were prepared by Hench et al [21,22], silicate, borate, and phosphate bioactive glasses have been reported in the literature [23]. Standard commercialized bioactive glasses are SiO₂-based glasses. Bioactive phosphate glasses have been studied for tissue engineering such as regeneration of bones [24] and muscles [25]. **Figure 1.3** [26] shows a schematic illustration of the reaction sequence leading to hydroxy-carbonate apatite (HCA) formation according to Hench and co-workers [27,28]. The ionic components such as calcium and phosphate ions of phosphate glasses released during degradation support bone growth [29]. The high solubility of phosphate glasses compared to silicate glasses can contribute to nucleation and apatite layer formation that is the main factor of bioactivity of bioactive glasses [30]. Degradation rates of phosphate glasses can be controlled by altering glass compositions [29]. Phosphate glass fibers are studied as a scaffold for muscle regeneration [25].

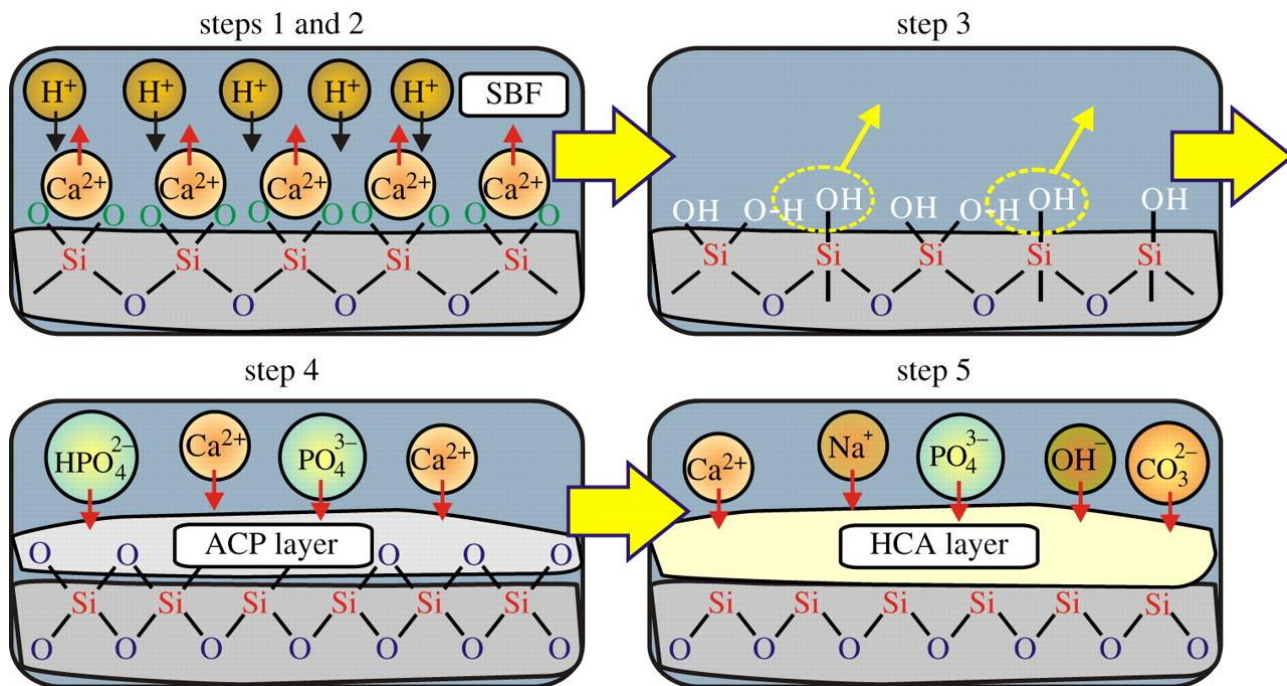


Fig. 1.3 Schematic illustration of the reaction sequence leading to hydroxy-carbonate apatite (HCA) formation according to Hench and co-workers [27,28], here assuming a melt-prepared CaO-SiO_2 glass. The first three stages involve reactions between the silicate surface and the surrounding fluid as follows: (1) $\text{Ca}^{2+} \leftrightarrow \text{H}^+$ exchange and (2) breakage of Si-O-Si bonds, leading to the formation of Si-OH groups; (3) repolymerization: $2\text{Si-OH} \rightarrow \text{Si-O-Si} + \text{H}_2\text{O}$. Next follows (4) the formation of amorphous calcium phosphate (ACP) and (5) $\text{ACP} \rightarrow \text{HCA}$ crystallization that involves uptake of additional ions, e.g. OH^- , CO_3^{2-} and Na^+ . Reproduced with permission from Ref. [26]. Copyright 2012, The Royal Society.

Properties of oxide glasses are also controlled by post-treatments. Typical post-treatments are crystallization, phase separation, and strengthening.

The stability of compositions of oxide glasses in crystal states is higher than that in amorphous states. However, oxide glasses are amorphous states which are thermodynamically metastable because oxide glasses are produced by solidifying glass melts at cooling rates faster than crystallization. When oxide glasses are heated at an appropriate temperature above the glass transition temperature (T_g), the oxide glasses gradually change to thermodynamically stable crystal states. The crystallization is used for the productions of glass-ceramics with structures in which crystal particles are dispersed in a glass matrix. There are two methods for producing glass-ceramics: volumetric crystallization in which bulk glasses are heated to generate crystals inside the glasses and sinter-crystallization in which sintered powdered glasses are heated for surface crystallization at interfaces of the glasses as shown in **Fig. 1.4** [31]. Properties of glass-ceramics are controlled by optimization of compositions of glass ceramics, types and sizes of crystal particles, and a fraction of glass matrix and crystal particles. $\text{SiO}_2\text{-Al}_2\text{O}_3\text{-Li}_2\text{O}$ and $\text{SiO}_2\text{-Al}_2\text{O}_3\text{-CaO}$ glass systems are typical compositions of glass-ceramics that have already been put to practical use. Nucleation agents such as TiO_2 may be contained in glasses for glass-ceramics to increase crystal-nucleation rates. Glass-ceramics with

small coefficients of thermal expansion about $-10 \times 10^{-7}/^{\circ}\text{C}$ are used for fire-rated windows, tableware, and cook-top panels [32]. High-strength glass-ceramics are used for building interior and exterior walls [32].

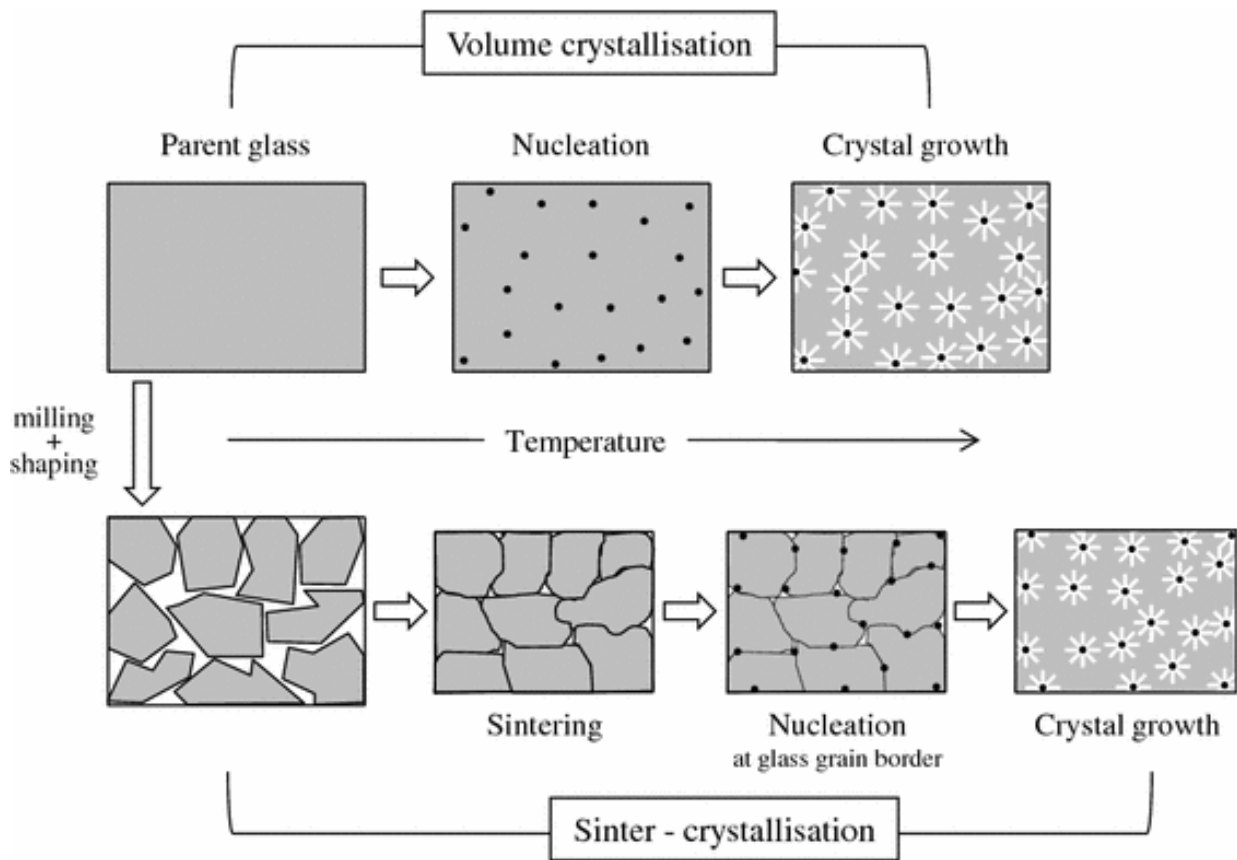


Fig. 1.4 Schematic illustration of the evolution of microstructure for glass to glass-ceramic through volume crystallization from a bulk glass or sinter-crystallization from a glass powder compact. Reproduced with permission from Ref. [31]. Copyright 2011, Springer Science Business Media, LLC.

Phase-separated glasses can be obtained when the melt of oxide glasses with the immiscible region is cooled. Even if oxide glasses have an immiscible region below the liquidus line, which is called the metastable immiscible region, homogeneous oxide glasses can be obtained because oxide glasses are produced by solidifying glass melts at cooling rates faster than phase separation. Phase-separated glasses can be obtained by keeping oxide glasses with the metastable immiscible region at an appropriate temperature above T_g . **Fig. 1.5** shows a schematic phase diagram showing metastable and stable immiscibility regions with images of phase separation texture [33]. Since $\text{SiO}_2\text{-B}_2\text{O}_3\text{-Na}_2\text{O}$ glass systems have a wide metastable immiscibility region, phase-separated glasses in this system have already been put to practical use [33]. In the case of one kind of $\text{SiO}_2\text{-B}_2\text{O}_3\text{-Na}_2\text{O}$ glass system, phase separation to SiO_2 -rich and $\text{B}_2\text{O}_3\text{-Na}_2\text{O}$ -rich phases occurs. Since the phase-separated glass obtained by spinodal decomposition forms a structure in which two phases are entangled, the $\text{B}_2\text{O}_3\text{-Na}_2\text{O}$ -rich phase is eluted when the phase-separated glass is immersed in an acid solution, and a SiO_2 porous body can be obtained. When the porous body is heat-treated, the pores disappear, and it becomes 96% silica glass [1]. Since the silica glass has a small coefficient of

thermal expansion, it is used as a heat-resistant glass. In the case of the other kind of $\text{SiO}_2\text{-B}_2\text{O}_3\text{-Na}_2\text{O}$ glass system, phase separation to SiO_2 -rich and $\text{B}_2\text{O}_3\text{-Na}_2\text{O}$ -rich phases occurs. The phase-separated glass obtained by the nucleation-growth mechanism forms a structure in which the $\text{B}_2\text{O}_3\text{-Na}_2\text{O}$ -rich phase is dispersed in the SiO_2 -rich matrix phase [1]. The phase-separated glass is used as laboratory glasses because it has a high heat resistance and chemical durability.

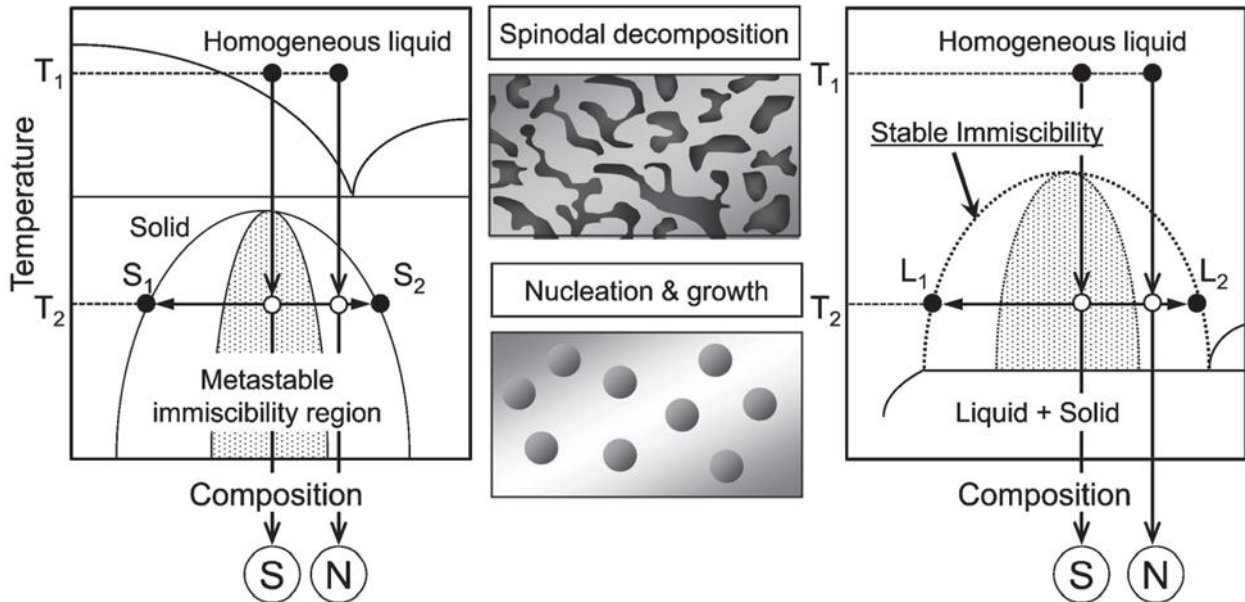


Fig. 1.5 Schematic phase diagram showing metastable and stable immiscibility regions with images of phase separation texture. The spinodal decomposition and nucleation growth mechanism are denoted, respectively, as “S” and “N”. Reproduced with permission from Ref. [33]. Copyright 2013, The Ceramic Society of Japan.

Although the theoretical strength of oxide glasses estimated from the atomic bond force is 10–20 GPa, the strength of products of oxide glasses is about 100 MPa as shown in **Fig. 1.6** [34,35]. Since flaws exist on the surface of glass products, crack propagation caused by stress concentration at the tip of cracks results in lower strength of glass products compared to theoretical strength.

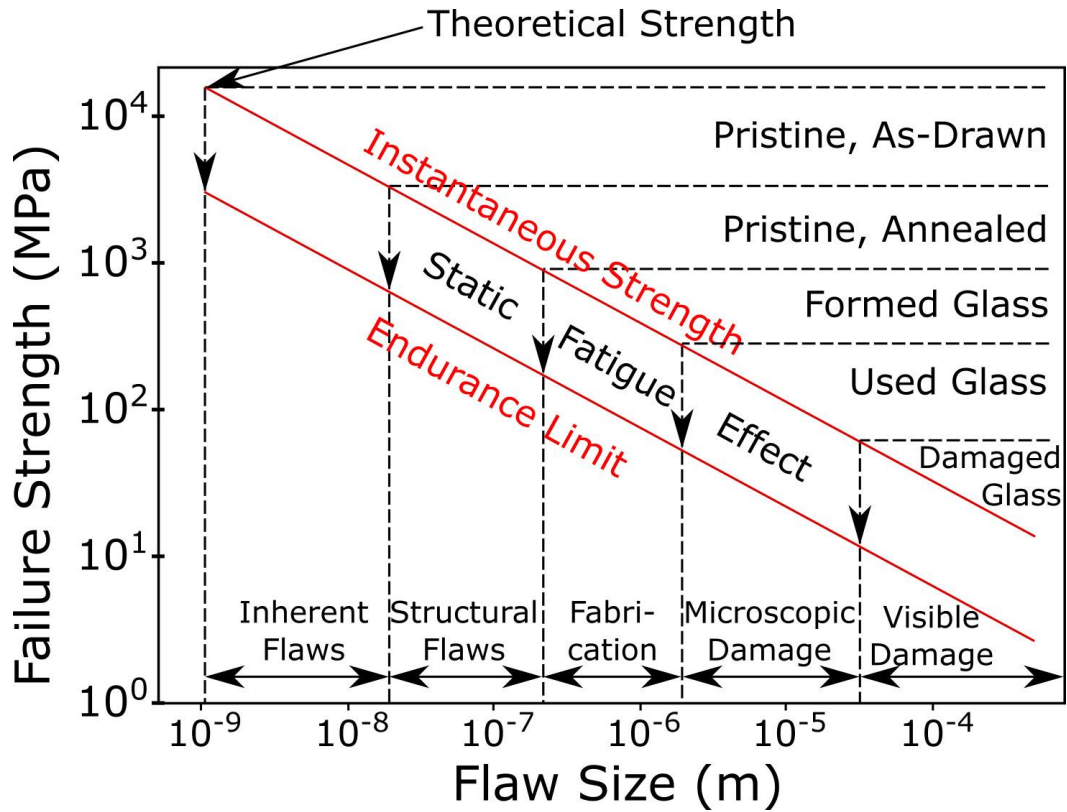


Fig. 1.6 Theoretical strength and strength of glass products. Reproduced with permission from Ref. [34,35]. Copyright 2018, The American Ceramic Society and Wiley Periodicals, Inc.

The strength of oxide glasses can be improved by forming compressive stress layers on glass surfaces that suppress crack propagation. The compressive stress layers can be formed by chemical strengthening in which smaller alkali cations in the glass surface are exchanged with larger alkali cations as shown in **Fig. 1.7** [36], and thermal tempering in which a glass heated to near softening temperature is quenched to generate residual stress on the glass surface. Chemically tempered glasses are used for cover glasses for smartphones and tablet computers. Thermally tempered glasses are used for window glass of vehicles.

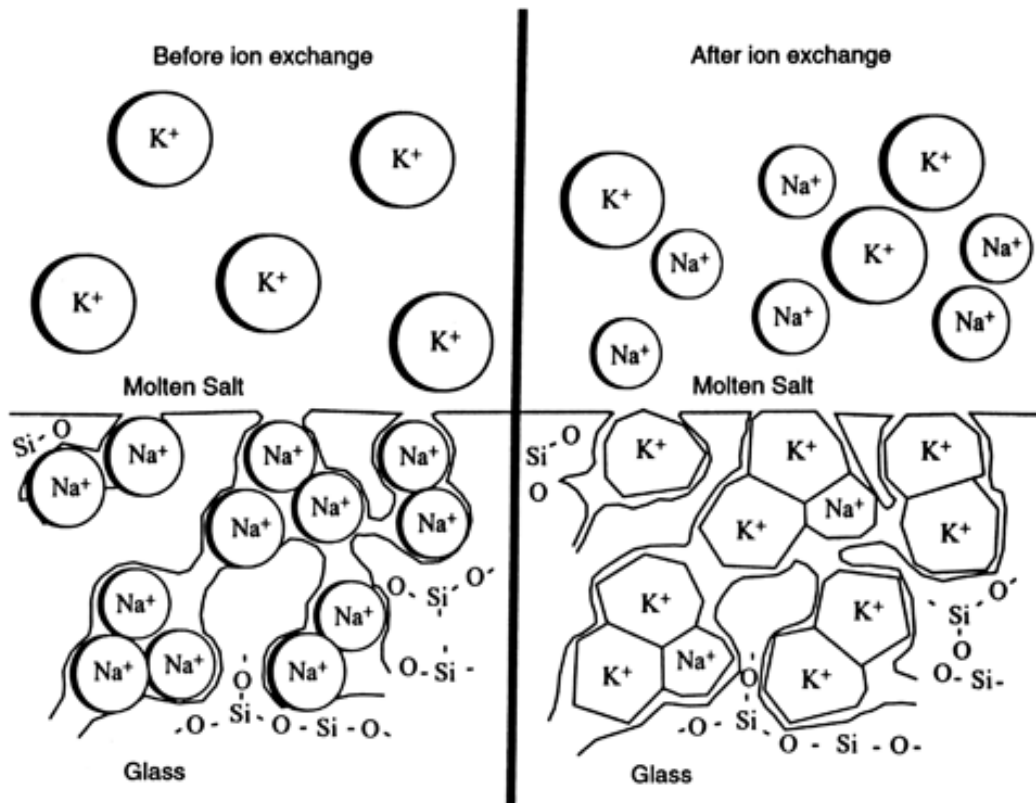
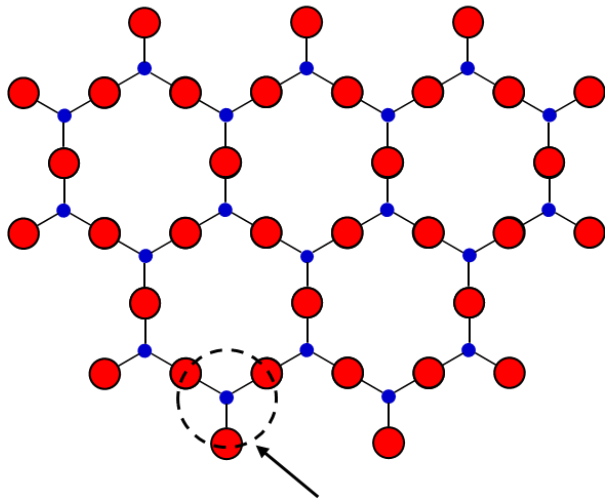


Fig. 1.7 Schematic illustration of ion exchange of alkali silicate glasses. Reproduced with permission from Ref. [36]. Copyright 2010, Saxon Glass Technologies Inc. Journal compilation, Copyright 2010, The American Ceramic Society and Wiley Periodicals, Inc.

1.2 Structures of oxide glasses

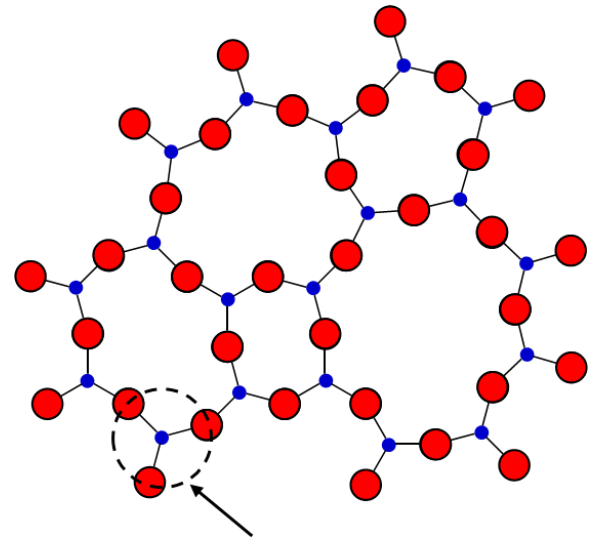
Basic structures of oxide glasses are polyhedrons in which oxygen surrounds cations, e.g. SiO_4 tetrahedral units in SiO_2 glass and PO_4 tetrahedral units in P_2O_5 glass. Three-dimensional network structures are formed by the polyhedral units sharing oxygens, called bridging oxygens, at their corners. SiO_2 , P_2O_5 , etc. are called glass network formers. **Figure 1.8 (a) and (b)** show schematic illustrations of network structures of cristobalite crystal and silica glass composed of only SiO_2 tetrahedral units. Cristobalite is composed of a network structure with long-range order, whereas silica glass is composed of a non-regular network structure without long-range order. On the other hand, alkali oxides (M_2O) and alkaline-earth oxides ($\text{M}'\text{O}$) are called glass network modifiers because they are included in the network structure formed by the glass network formers. **Figure 1.8 (c)** shows a schematic illustration of the structure of the $\text{SiO}_2\text{--M}_2\text{O}$ glass system. The addition of M_2O leads to bond breaking of some Si--O--Si bonds in the glass network structure. The oxygens that bonds are broken are called non-bridging oxygens (NBO). Properties of oxide glasses are changed by types and the amount of the glass network modifiers. Al_2O_3 , TiO_2 , ZrO_2 , etc. are called intermediates because the oxides do not form glass by themselves, but form glass network structures when coexisting with glass network formers.

(a) Cristobalite



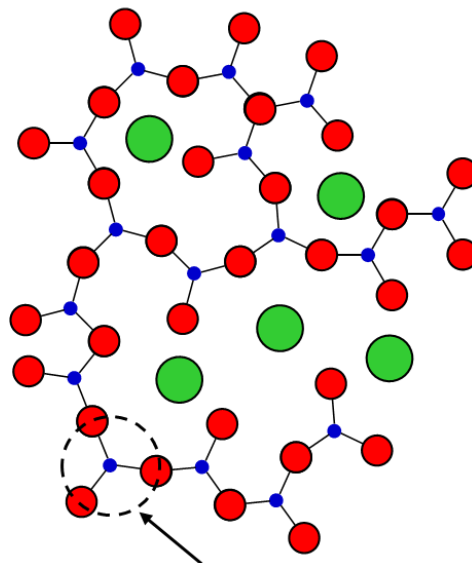
SiO₄ tetrahedral unit

(b) Silica glass



SiO₄ tetrahedral unit

(c) SiO₂-M₂O glass



SiO₄ tetrahedral unit

Fig. 1.8 Schematic illustrations of the structure of (a) cristobalite crystal, (b) silica glass, and (c) SiO₂-M₂O glass system. The illustrations are drawn according to two-dimensional representations by Zachariasen [37], and Warren and Biscob [38]. Small (blue), middle-sized (red), and large (green) closed circles represent phosphorus, oxygen, and alkali cations, respectively.

Figure 1.9 shows PO_4 tetrahedral units in phosphate glasses. An increase in the amount of M_2O in $x\text{M}_2\text{O}-(1-x)\text{P}_2\text{O}_5$ glasses (mol%) causes an increase in the number of NBOs and change of PO_4 tetrahedral units from Q^n units (PO_4 tetrahedral units with n bridging oxygens) to Q^{n-1} units (PO_4 tetrahedral units with $n-1$ bridging oxygens) ($n = 1-3$).

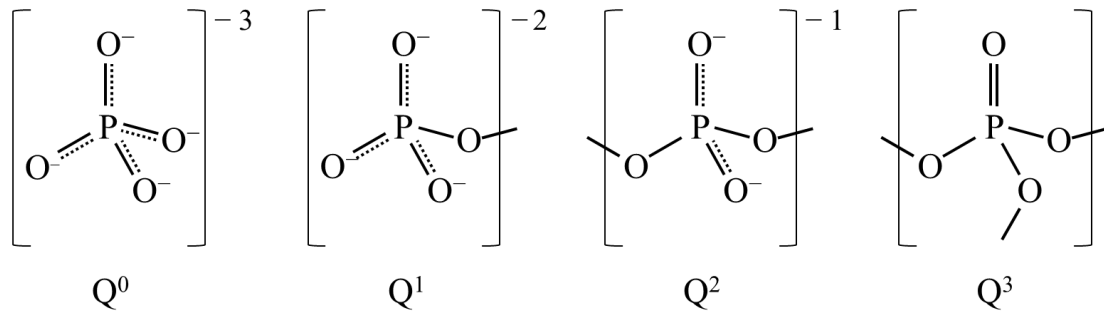


Fig. 1.9 PO_4 tetrahedral units in phosphate glasses

$50\text{M}_2\text{O}-50\text{P}_2\text{O}_5$ glasses (mol%) are called alkali metaphosphate glasses. Alkali metaphosphate glasses are composed of $-\text{P}-\text{O}-\text{P}-$ chains and rings formed by Q^2 units linked each other with two covalent bonds [6]. Two bonds between P and NBO in the Q^2 units form resonance structures with single and double bonds [39]. The chain and ring structures are connected by ionic bonds between alkali cations and oxygens as shown in **Fig. 1.10**. Alkali metaphosphate glasses have isotropic structures because the chain and ring structures are oriented in random directions. On the other hand, alkali metaphosphate crystals are also composed of chain and ring structures, but the chain structures of alkali metaphosphate crystals are oriented in the uniaxial direction as shown in **Fig. 1.11** [40–42].

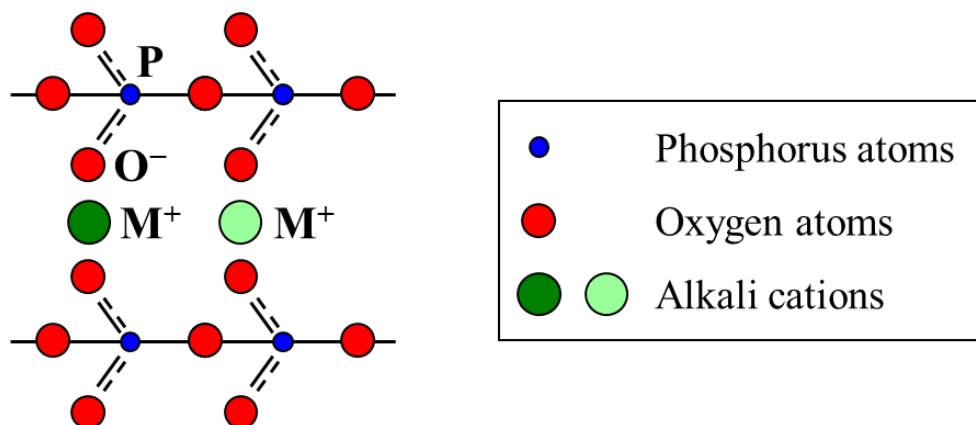
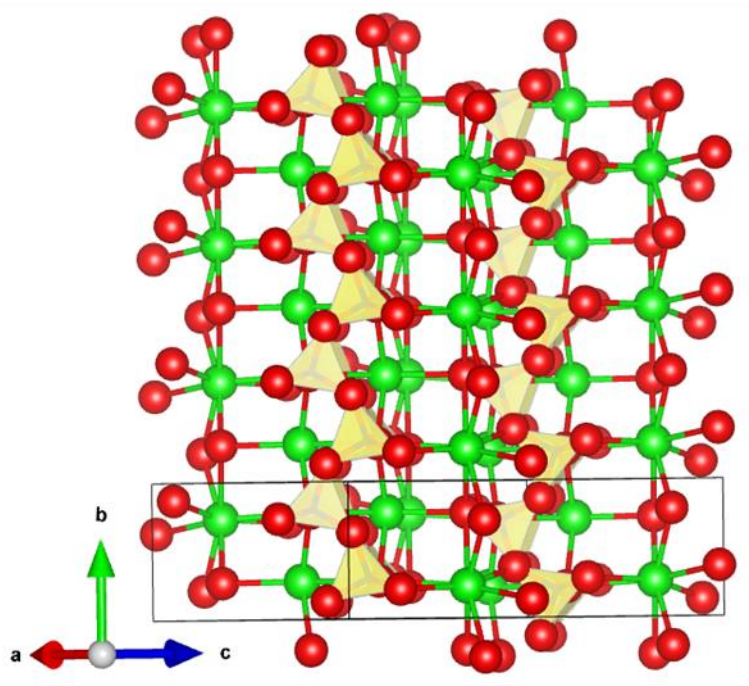


Fig. 1.10 Schematic illustration of a structure of mixed alkali metaphosphate glass. Small (blue), middle-sized (red), and large (green) closed circles represent phosphorus atoms, oxygen atoms, and alkali cations, respectively. Darker green circles represent alkali cations with a higher force constant between alkali cation and oxygen ($F_{\text{M-O}}$).

KPO₃ crystal with chain structure



KPO₃ crystal with ring structure

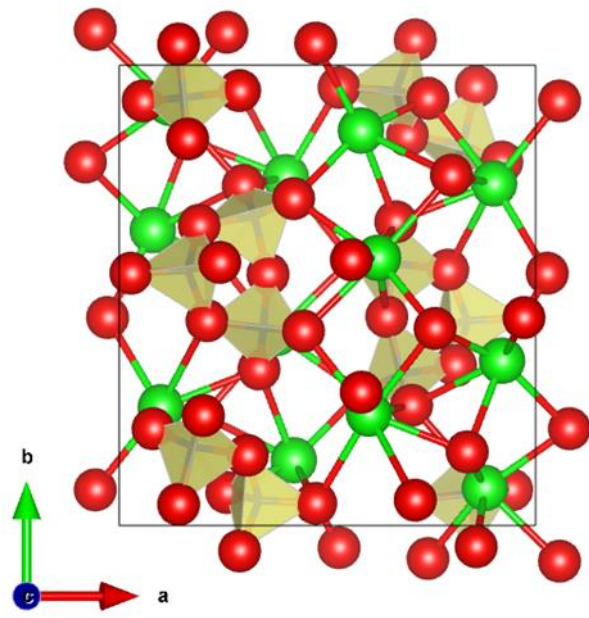


Fig. 1.11 Crystal structures of 50K₂O–50P₂O₅ (mol%, KPO₃) metaphosphate crystals with chains [40] and three-membered rings [41]. Yellow tetrahedra and red and green balls are PO₄ tetrahedra, oxygen atoms, and K⁺ cations. (Drawn by VESTA ver. 3.5.7 [42])

1.3 Previous studies on oxide glasses with anisotropic structures

1.3.1 Formation of anisotropic structures in oxide glasses

Table 1.2 shows the birefringence of glass fibers with various compositions prepared above T_g by the nozzle drawing method and the rod pulling method [43–45]. Birefringence of fibers is defined as the difference between the refractive indices observed by using light with a plane of polarization parallel and perpendicular to the fiber axis when observing the fiber from the side [46]. Birefringence is used as a measure of the degree of orientation of glass structure in the length direction of the fiber. Birefringence increases with increasing the degree of orientation. The existence of asymmetric hollows in the open silica glass structure deformed and oriented by the drawing process causes birefringence of the silica glass fiber [43]. The small birefringence of the silica glass fiber indicates the difficulty of the orientation of three-dimensional network structures for silica glass in the tensile stress direction. On the other hand, the birefringence of the alkali metaphosphate, alkaline-earth metaphosphate, and alkali metasilicate glass fibers is larger than that of the silica glass fiber. The birefringence of the metaphosphate and metasilicate glass fibers, respectively, results from a high degree of orientation of chain structures of PO_4 tetrahedral units and partial chain structures of SiO_4 tetrahedral units [44,45]. The much larger birefringence of the alkali metaphosphate glass fiber compared to the other glass fibers indicates that chains of the alkali metaphosphate glass are, especially, easily oriented in the tensile stress direction.

Table 1.2 Birefringence of glass fibers with various compositions drawn above T_g and shrinkage of the fibers in the length direction during heating.

Compositions (mol%)	Birefringence (nm/mm)	Shrinkage (%)	References
SiO_2	30	3	[43]
$25\text{Li}_2\text{O}-25\text{Na}_2\text{O}-50\text{P}_2\text{O}_5$	10000	3	[44]
$25\text{CaO}-25\text{BaO}-50\text{P}_2\text{O}_5$	400	1.5	[44]
$16.7\text{Li}_2\text{O}-16.7\text{Na}_2\text{O}-16.7\text{K}_2\text{O}-50\text{SiO}_2$	1000	11	[45]

Inaba et al. [47,48] investigated relationships between birefringence and compositions of alkali metaphosphate glass fibers deformed under uniaxial tensile stress above T_g and then rapidly cooled to room temperature (**Fig. 1.12**). The birefringence of the fibers becomes larger with increasing the number of types of alkali cations. The $16.7\text{Li}_2\text{O}-16.7\text{Na}_2\text{O}-16.7\text{K}_2\text{O}-50\text{P}_2\text{O}_5$ (mol%, $(\text{Li},\text{Na},\text{K})\text{PO}_3$) and $12.5\text{Li}_2\text{O}-12.5\text{Na}_2\text{O}-12.5\text{K}_2\text{O}-12.5\text{Cs}_2\text{O}-50\text{P}_2\text{O}_5$ (mol%, $(\text{Li},\text{Na},\text{K},\text{Cs})\text{PO}_3$) glasses, especially, have larger birefringence compared to the other alkali metaphosphate glasses. Structural investigations of the anisotropic $(\text{Li},\text{Na},\text{K})\text{PO}_3$ and $(\text{Li},\text{Na},\text{K},\text{Cs})\text{PO}_3$ glass fibers by Raman spectroscopy and high-energy X-ray diffraction showed that the anisotropic glass fibers have $-\text{P}-\text{O}-\text{P}-$ chains oriented along the deformation direction [47,48].

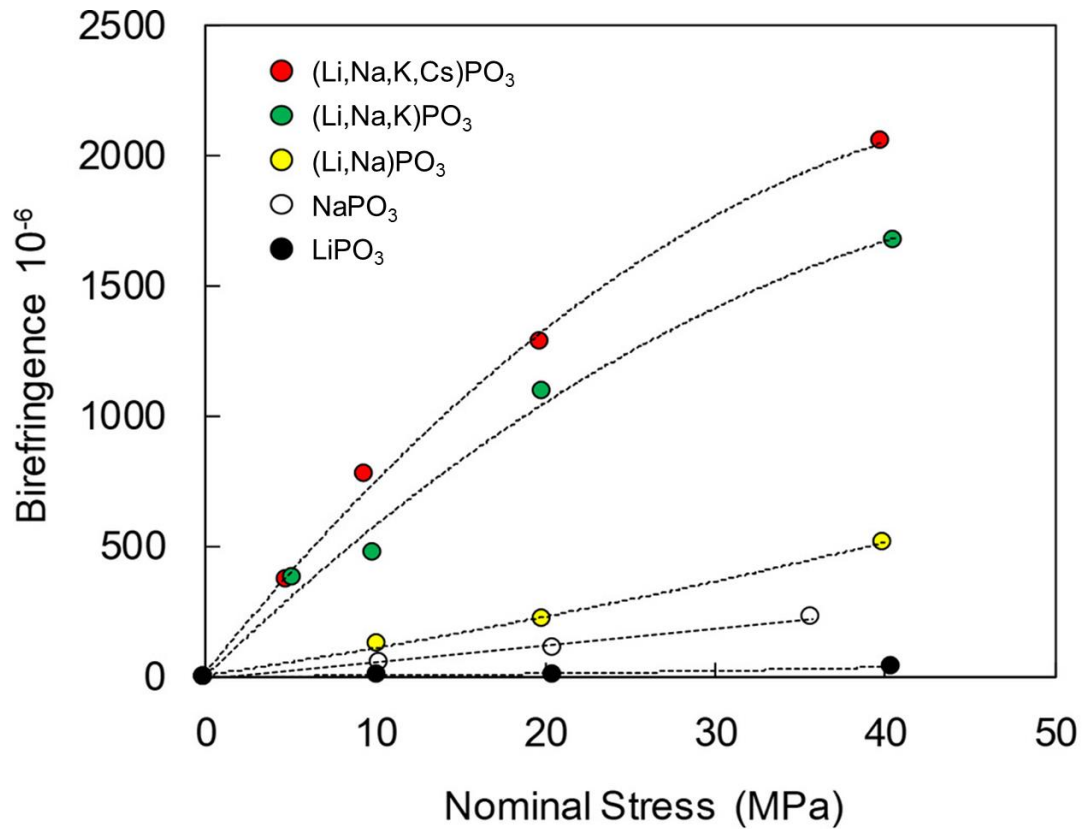














Fig. 1.12 Birefringence of alkali metaphosphate glass fibers elongated under uniaxial tensile stress above T_g and then rapidly cooled to room temperature. Reproduced with permission from Ref. [48]. Copyright 2020, The American Ceramic Society.

Difference of birefringence between the anisotropic 25Li₂O–25Na₂O–50P₂O₅ (mol%, (Li,Na)PO₃) glass fibers prepared in references [44] and [48] results from the difference of preparation methods and conditions of the fibers. If the anisotropic (Li,Na,K)PO₃ and (Li,Na,K,Cs)PO₃ glasses are prepared by the same methods and similar conditions in reference [44], the birefringence of the glasses must be higher than that shown in **Fig. 1.12**.

1.3.2 Huge shrinkage due to entropic elasticity of anisotropic (Li,Na,K,Cs)PO₃ glass

Shrinkage of the glass fibers with various compositions prepared above T_g by the nozzle drawing method and the rod pulling method during reheating up to around T_g is shown in **Table 1.2** [43–45]. The maximum value of shrinkage shown in **Table 1.2** is 11%. **Figure 1.13** shows a dimensional change of isotropic and anisotropic (Li,Na,K,Cs)PO₃ glass fibers during heating above T_g [47]. Shrinkage of the glass fibers increases with increasing birefringence. The glass fiber with birefringence of 0.0069 (= 6900 nm/mm), especially, shows huge shrinkage (35% lengthwise).

(a)

No.	Ref	1	2	3	4	5
Δn	0	0.0017	0.0029	0.0034	0.0058	0.0069
Before heat treatment						
Δn	0	0	0	0	0	0
After heat treatment						

2.5 mm

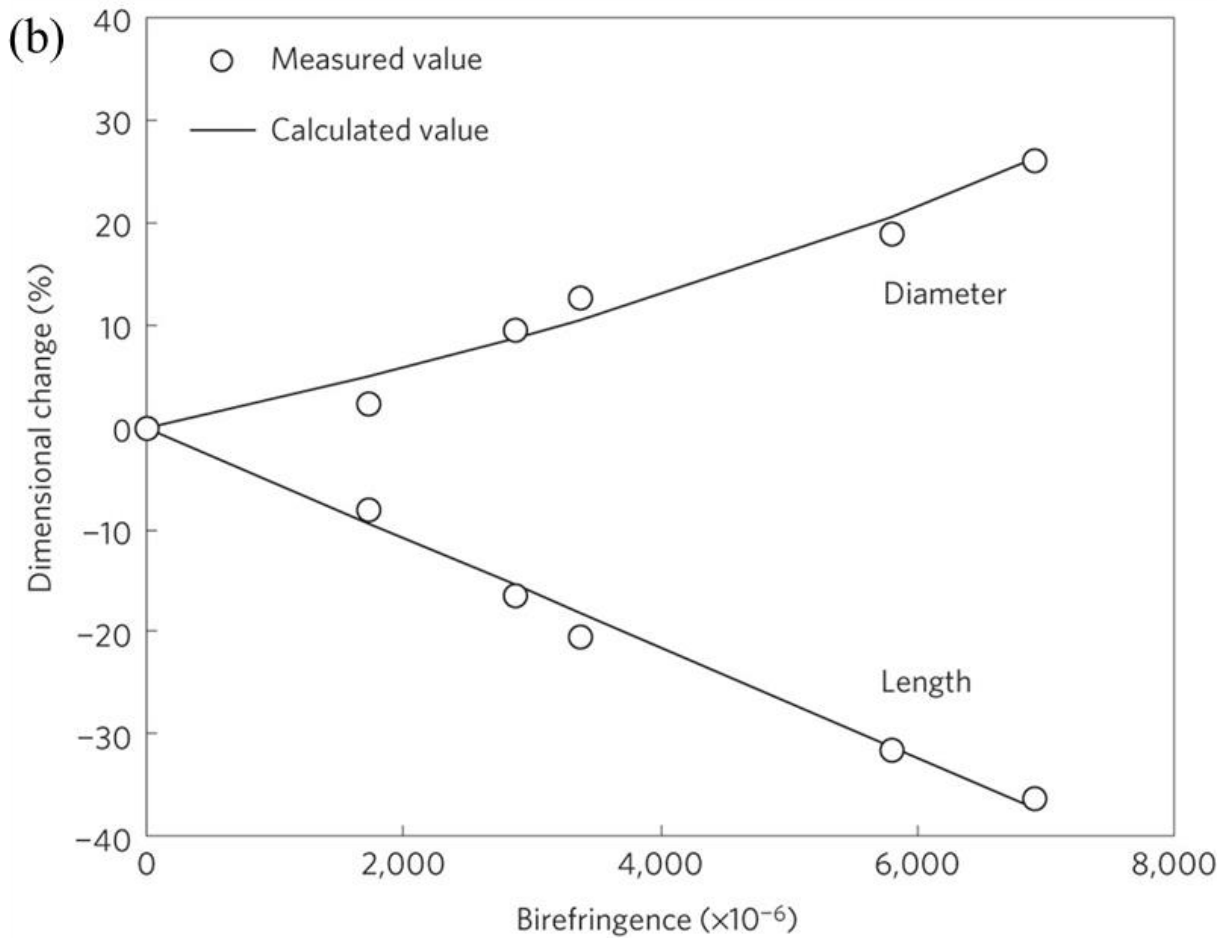


Fig. 1.13 Dimensional change of isotropic and anisotropic (Li,Na,K,Cs)PO₃ glass fibers during heating above T_g . Δn is the birefringence of the glass fibers. Reproduced with permission from Ref. [47]. Copyright 2014, Nature Publishing Group.

The huge shrinkage is interpreted as being derived from entropic elasticity because the endothermic phenomenon above T_g , which is characteristic of rubbers, is observed during differential scanning calorimetry of the anisotropic (Li,Na,K,Cs)PO₃ glass as shown in **Fig. 1.14** [47]. This is the first observation of the entropic deformation of an oxide glass [47]. Structural investigations of alkali metaphosphate glasses by high-energy X-ray diffraction show that the distance between $-P-O-P-$ chains in (Li,Na,K,Cs)PO₃ glass is larger than that in 50Li₂O–50P₂O₅ (mol%) glass [47]. This result indicates that the interchain spacing attracted by lithium ions in (Li,Na,K,Cs)PO₃ glass should be smaller than that by the other alkali ions, and the chains attracted by lithium ions should interact strongly with each other [47].

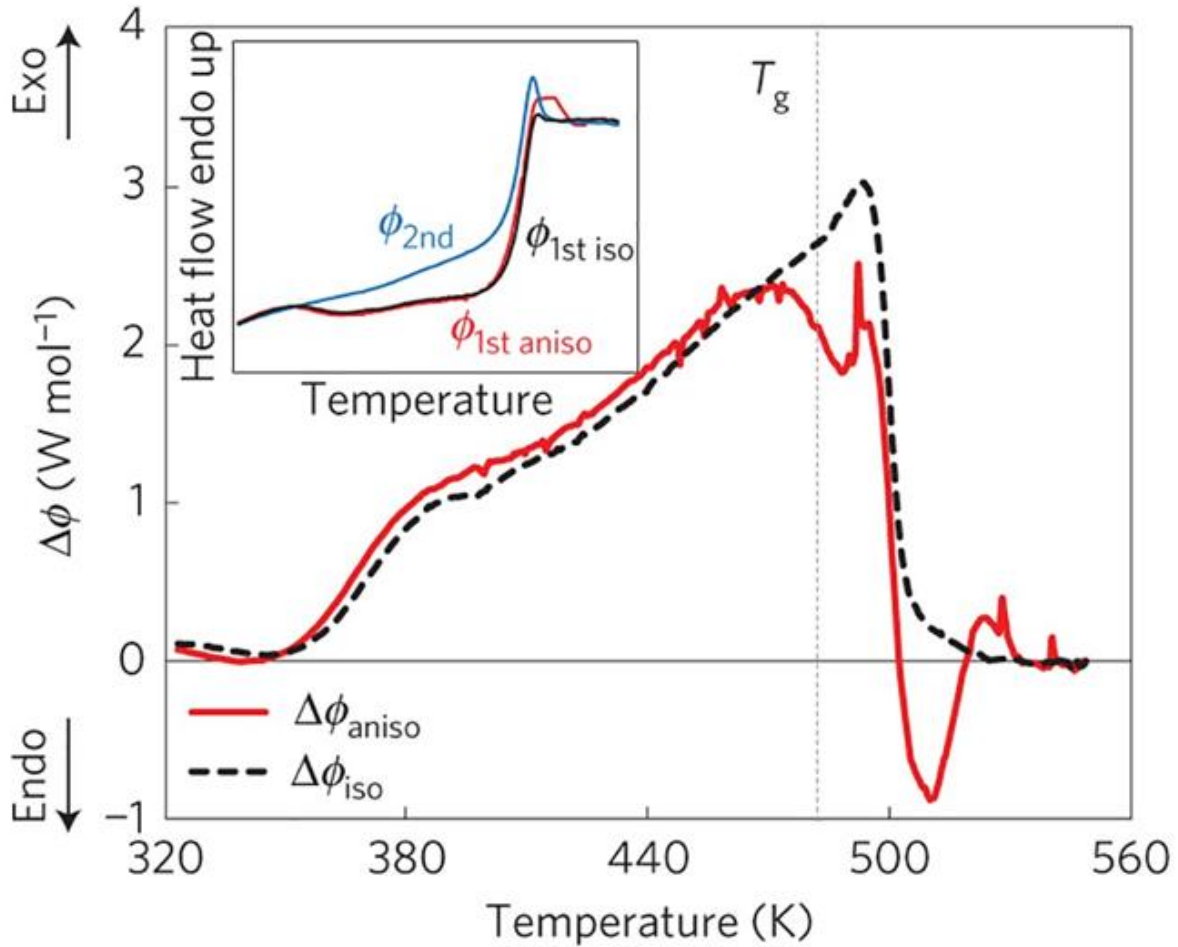


Fig. 1.14 Differential scanning calorimetry (DSC) curves of anisotropic and isotropic (Li,Na,K,Cs)PO₃ glasses. Heat flow difference $\Delta\phi (= \phi_{2nd} - \phi_{1st})$ of anisotropic and isotropic fibers as a function of temperature. Inset: DSC upscans (that is, heating scans) of anisotropic and isotropic fibers. Red and black lines are heat flows ϕ of the first upscan for anisotropic and isotropic fibers, respectively; blue lines are heat flows of second upscans for both samples. Reproduced with permission from Ref. [47]. Copyright 2014, Nature Publishing Group.

Figure 1.15 shows the model proposed by Inaba et al. as the mechanism of the orientation and relaxation of $-P-O-P-$ chains in (Li,Na,K,Cs)PO₃ glass in the temperature range where the entropic elasticity occurs [47]. According to the model, Li⁺ cations, which have higher interchain force compared to Na⁺, K⁺, and Cs⁺ cations, would act as pseudo-cross-linkage portions between chains during orientation and relaxation of local structures of $-P-O-P-$ chains being adjacent to Na⁺, K⁺, and Cs⁺ cations, which have lower interchain force, in the temperature range.

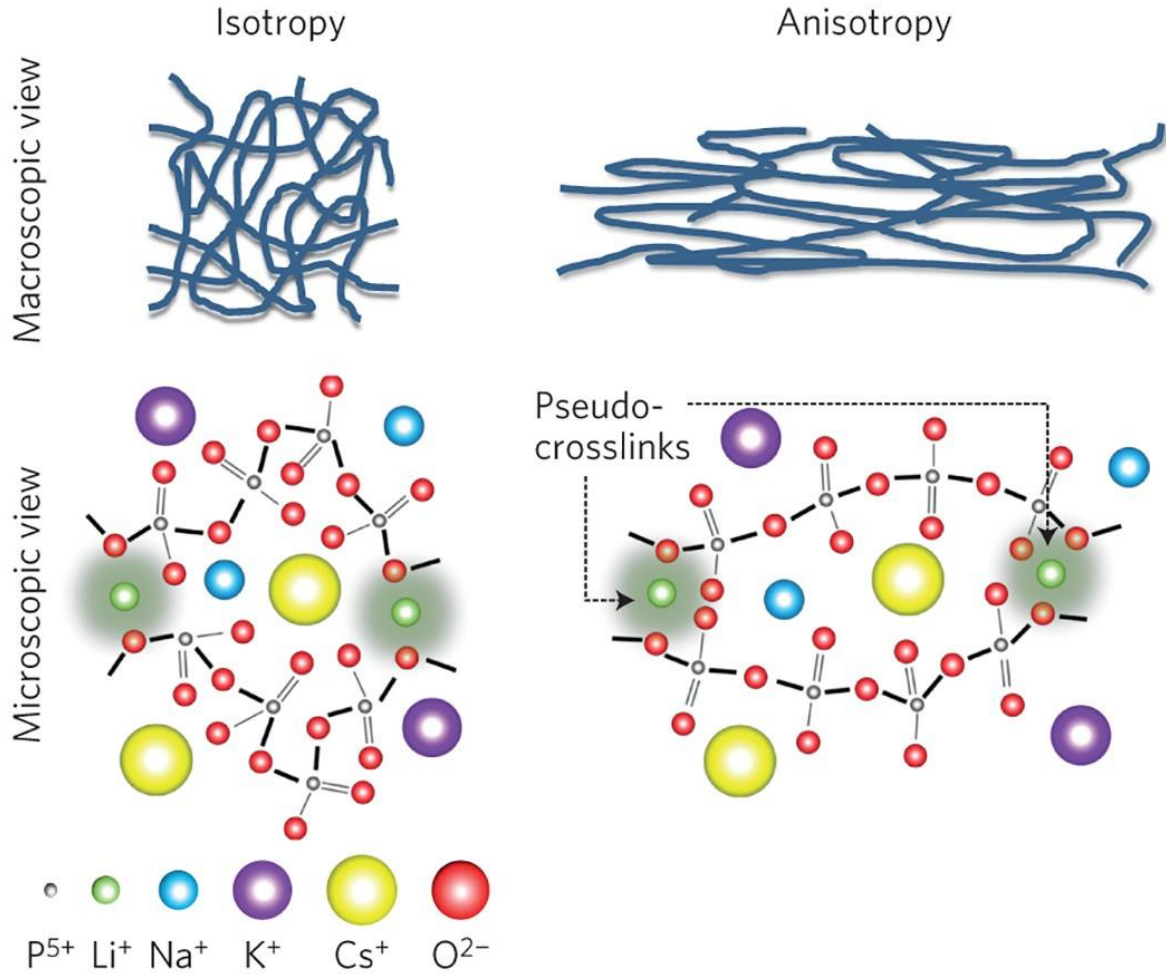


Fig. 1.15 Schematic illustrations of the model proposed by Inaba et al. as the mechanism of the orientation and relaxation of $-P-O-P-$ chains in $(Li,Na,K,Cs)PO_3$ glass. Reproduced with permission from Ref. [47]. Copyright 2014, Nature Publishing Group.

However, the coexistence of local structures with higher force constant between alkali cation and oxygen (F_{M-O}) and local structures with lower F_{M-O} in $(Li,Na,K,Cs)PO_3$ glass as the model proposed by Inaba et al. has not been proved by experiment. In addition, although chain and ring structures coexist in alkali metaphosphate glasses, effects of ratios of Q^2 units in chain structures to total Q^2 units on ease of orientation of $-P-O-P-$ chains under uniaxial tensile stress above T_g is still unknown.

The study of the formation of the anisotropic structure of alkali metaphosphate glasses by Inaba et al. [47] is used for the development of hybrid optical fibers composed of metaphosphate and silica glasses [49]. New hybrid optical fibers composed of new combinations of glasses can be obtained by the pressure-assisted melt-filling process in which glass melt for the core of the optical fiber is injected into a thin capillary of the other glass for cladding of optical fiber by the assist of pressure. Since phosphate glass can contain a high concentration of rare-earth ions, and reaction between phosphate and silica glasses is unlikely to occur during the pressure-assisted melt-filling process due to the low T_g and melting point of phosphate glasses, hybrid fiber optical waveguides composed of a core of silver metaphosphate glasses and clad of silica glass

recently are studied [49,50]. Orientation of chains for silver metaphosphate glass occurs during the pressure-assisted melt-filling process [49]. **Figure 1.16** shows cross-sectional microscopic images of a hybrid glass fiber composed of a core of silver metaphosphate glasses and clad of silica glass prepared by the pressure-assisted melt-filling process after heating [49]. A significant decrease in the degree of anisotropy due to structural relaxation occurs as T_g is approached [49]. This goes in-hand with volumetric shrinkage due to entropy-induced rearrangements of the molecular chains [49]. The optical properties of hybrid glass fibers composed of metaphosphate and silica glasses are expected to be controlled by not only compositions but also anisotropic structures of metaphosphate glasses because $-P-O-P-$ chains are oriented during the pressure-assisted melt-filling process.

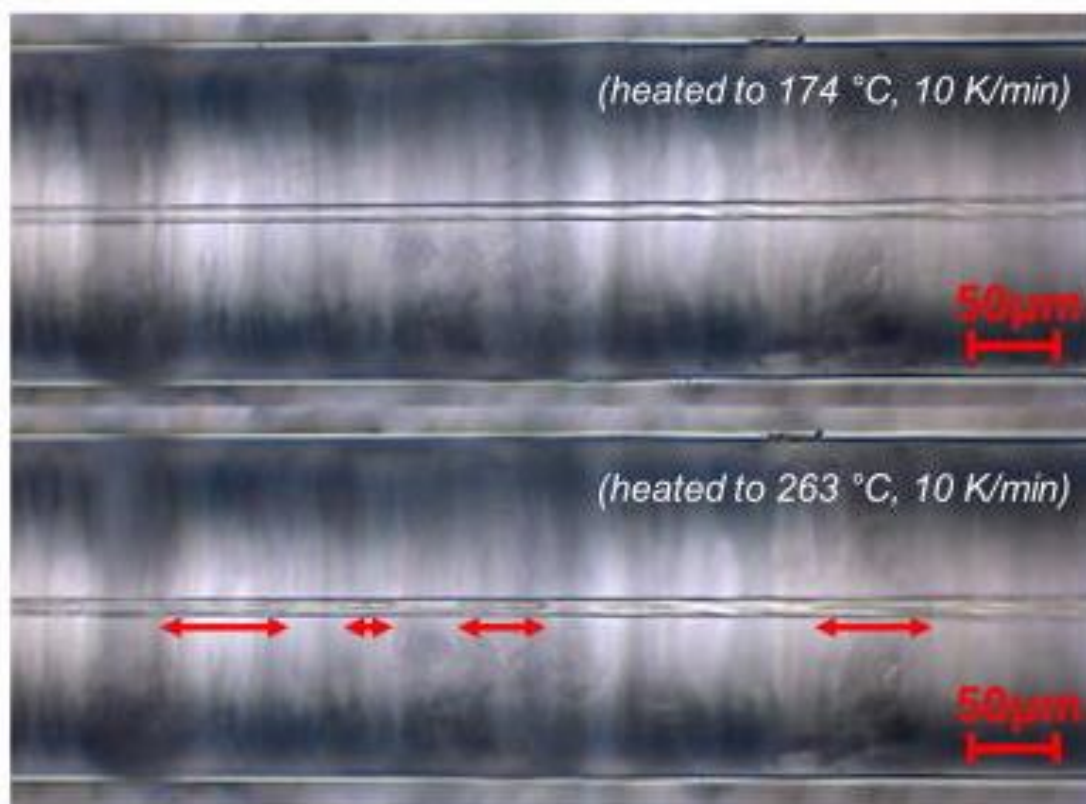


Fig. 1.16 Microscopic images of a filled sample section after heating to 174 °C (no shrinkage, top) and 263 °C (bottom), respectively (filled at 70 bar, 600 °C, 1 h, and re-heated at 10 K/min). Reproduced with permission from Ref. [49]. Copyright 2017, AIP Publishing.

1.4 The objective of this thesis

Since mechanical and thermal properties can be improved by the orientation of chain organic polymer molecules [51-56], the properties of oxide glasses should be improved by forming anisotropic structures in which chains are uniaxially oriented. In addition, unique properties not found in isotropic glasses should be obtained in the anisotropic oxide glasses. As mentioned above, it has been reported that birefringence and entropy elasticity occur due to the orientation and relaxation of chains in $(Li,Na,K,Cs)PO_3$ mixed alkali

metaphosphate glass [47]. However, the effects of the anisotropic structures with uniaxially oriented chains in oxide glasses on properties are still poorly understood.

The objective of this thesis is the clarification of important structural factors for the formation of significant anisotropy above T_g and the effect of the anisotropic structures on the mechanical properties of alkali metaphosphate glasses for the development of new anisotropic oxide glasses with new properties not reported in oxide glasses and new methods to improve mechanical properties of oxide glasses.

1.5 The composition of this thesis

In this thesis, study results about structural factors for the formation of significant anisotropy above T_g and the effect of the anisotropic structures with uniaxially oriented chains on the mechanical properties of alkali metaphosphate glasses are described. This thesis is composed of six chapters. The outline of each chapter is described below.

Chapter 1: The background and objective of this thesis were described.

Chapter 2: Since (A) there is not enough evidence of the large distribution of F_{M-O} for (Li,Na,K)PO₃ and (Li,Na,K,Cs)PO₃ glasses as the model proposed by Inaba et al. and (B) difference of the number of Q² units in –P–O–P– chains for alkali metaphosphate glasses is still unknown, structural features of (Li,Na,K)PO₃ glass for the formation of highly oriented –P–O–P– chains under uniaxial tensile stress above T_g was investigated because clarification of the structural features will be useful knowledge for the development of anisotropic glasses.

Chapter 3: Since (A) there is not enough evidence of the relaxation of the local structures with small F_{M-O} under coexistence with the local structures with large F_{M-O} which act as pseudo-cross-linked structures in anisotropic (Li,Na,K,Cs)PO₃ glass above T_g as the model proposed by Inaba et al. and (B) the relaxation mechanism of anisotropic (Li,Na,K,Cs)PO₃ glass below T_g is still unknown, relaxation mechanisms of anisotropic (Li,Na,K,Cs)PO₃ glass in the range from room temperature to above T_g were investigated.

Chapter 4: Since deformation behavior of (Li,Na,K,Cs)PO₃ glass under compressive stress above T_g is still unknown, the deformation behavior of (Li,Na,K,Cs)PO₃ glass under compressive stress above T_g was investigated because clarification of the behavior will be useful knowledge for the development of applications of the glass which shows entropic elasticity above T_g .

Chapter 5: Since the increase in fracture strength and Young's modulus by anisotropic structures in oxide glasses as with chain organic polymers has not been reported previously, the effect of orientation of –P–O–P– chains on fracture strength and Young's modulus of (Li,Na,K,Cs)PO₃ glass was investigated for the development of a new method to improve fracture strength and Young's modulus of oxide glasses.

Chapter 6: The important results and discussion of this thesis were summarized.

References

1. M. Yamane, I. Yasui, M. Wada, Y. Kokubu, R. Terai, T. Kondo, and S. Ogawa, Glass Kougaku Handbook, Asakura Publishing Co., Ltd. (1999) (in Japanese).
2. S. Sakka, Tokoton yasashii garasuno hon, Nikkan Kogyo Shimbun, Ltd. (2004) (in Japanese).

3. T. Einishi, The optional component which used phosphate glass, *New Glass* **22** 27–32 (2007) (in Japanese).
4. C. M. Jantzen, Systems approach to nuclear waste glass development, *J. Non-Cryst. Solids* **84** 215–225 (1986).
5. J. H. Campbell, T. I. Suratwala, C. B. Thorsness, J. S. Hayden, A. J. Thorne, J. M. Cimino, A. J. Marker III, K. Takeuchi, M. Smolley, and G. F. Ficini-Dorn, Continuous melting of phosphate laser glasses, *J. Non-Cryst. Solids* **263&264** 342–357 (2000).
6. R. K. Brow, Review: the structure of simple phosphate glasses, *J. Non-Cryst. Solids* **263&264** 1–28 (2000).
7. H. Li, M. J. Davis, A. J. Marker III, and J. S. Hayden, Glass and light, *Int. J. Appl. Glass Sci.* **1** 63–73 (2010).
8. N. G. Boetti, D. Pugliese, E. Ceci-Ginistrelli, J. Lousteau, D. Janner, and D. Milanese, Highly doped phosphate glass fibers for compact lasers and amplifiers: a review, *Appl. Sci.* **7** 1295 (2017).
9. N. G. Boetti, G. C. Scarpignato, J. Lousteau, D. Pugliese, L. Bastard, J.-E. Broquin, and D. Milanese, High concentration Yb-Er co-doped phosphate glass for optical fiber amplification, *J. Optics* **17** 065705 (2015).
10. N. O. Dantas, E. O. Serqueira, A. C. A. Silva, A. A. Andrade, and S. A. Lourenço, High quantum efficiency of Nd³⁺ ions in a phosphate glass system using the Judd–Ofelt theory, *Braz. J. Phys.* **43** 230–238 (2013).
11. A. Tervonen, B. R. West, and S. Honkanen, Ion-exchanged glass waveguide technology: a review, *Opti. Eng.* **50** 071107 (2011).
12. M. Guo, Y. Yue, J. Yu, C. Shao, J. Ren, X. Wang, and L. Hu, Effect of Li₂O substitution on structures and properties of Nd³⁺-doped Al(PO₃)₃-Li₂O glasses, *Int. J. Appl. Glass Sci.* **11** 66–77 (2020).
13. D. He, S. Kang, L. Zhang, L. Chen, Y. Ding, Q. Yin, and L. L. Hu, Research and development of new neodymium laser glasses, *High Power Laser Sci. Eng.* **5** e1 (2017).
14. J. H. Campbell and T. I. Suratwala, Nd-doped phosphate glasses for high-energy/high-peak-power lasers, *J. Non-Cryst. Solids* **263&264** 318–341 (2000).
15. R. Morena, Phosphate glasses as alternatives to Pb-based sealing frits, *J. Non-Cryst. Solids* **263&264** 382–387 (2000).
16. J. J. Shyu and C. H. Yeh, Formation and properties of SnO–MgO–P₂O₅ glasses, *J. Mater. Sci.* **42** 4772–4777 (2007).
17. J. J. Shyu and C. H. Yeh, Sintering, crystallization, and properties of a low-viscosity SnO–MgO–P₂O₅ glass, *J. Mater. Sci.* **44** 2985–2991 (2009).
18. J. Hong, D. Zhao, J. Gao, M. He, H. Li, and G. He, Lead-free low-melting point sealing glass in SnO–CaO–P₂O₅ system, *J. Non-Cryst. Solids* **356** 1400–1403 (2010).
19. A. Goel, J. S. McCloy, R. Pokorny, and A. A. Kruger, Challenges with vitrification of Hanford High-Level Waste (HLW) to borosilicate glass – An overview, *J. Non-Cryst. Solids: X* **4** 100033 (2019).
20. A. C. Joshi, M. Roy, D. P. Dutta, R. K. Mishra, S. S. Meena, R. Kumar, D. Bhattacharyya, R. Alexander,

- C. P. Kaushik, and A. K. Tyagi, Effect on the structure and stability of iron phosphate glass with Sb and Te-ion loading for nuclear waste storage application, *J. Non-Cryst. Solids* **570** 121016 (2021).
21. L. L. Hench, R. J. Splinter, W. C. Allen, and T. K. Greenlee, Bonding mechanisms at the interface of ceramic prosthetic materials, *J. Biomed. Mater. Res.* **5** 117–141 (1971).
 22. L. L. Hench, The story of bioglass, *J. Mater. Sci.: Mater. Med.* **17** 967–978 (2006).
 23. Q. Fu, J. C. Mauro, and M. N. Rahaman, Bioactive glass innovations through academia-industry collaboration, *Int. J. Appl. Glass Sci.* **7** 139–146 (2016).
 24. N. J. Lakhkar, J.-H. Park, N. J. Mordan, V. Salih, I. B. Wall, H.-W. Kim, S. P. King, J. V. Hanna, R. A. Martin, O. Addison, J. F. W. Mosselmans, and J. C. Knowles, Titanium phosphate glass microspheres for bone tissue engineering, *Acta Biomater.* **8** 4181–4190 (2012).
 25. R. Shah, A. C. M. Sinanan, J. C. Knowles, N. P. Hunt, and M. P. Lewis, Craniofacial muscle engineering using a 3-dimensional phosphate glass fibre construct, *Biomaterials* **26** 1497–1505 (2005).
 26. P. N. Gunawidjaja, R. Mathew, A. Y. H. Lo, I. Izquierdo-Barba, A. García, D. Arcos, M. Vallet-Regí, and M. Edén, Local structures of mesoporous bioactive glasses and their surface alterations in vitro: inferences from solid-state nuclear magnetic resonance, *Phil. Trans. R. Soc. A* **370** 1376–1399 (2012).
 27. L. L. Hench, Bioceramics: from concept to clinic, *J. Am. Ceram. Soc.* **74** 1487–1510 (1991).
 28. A. E. Clark, C. G. Pantano, and L. L. Hench, Auger spectroscopic analysis of bioglass corrosion films, *J. Am. Ceram. Soc.* **59** 37–39 (1976).
 29. C. Zhu, I. Ahmed, A. Parsons, Y. Wang, C. Tan, J. Liu, C. Rudd, and X. Liu, Novel bioresorbable phosphate glass fiber textile composites for medical applications, *Polym. Compos.* **39** E140–E151 (2018).
 30. E. A. A. Neel, D. M. Pickup, S. P. Valappil, R. J. Newport, and J. C. Knowles, Bioactive functional materials: a perspective on phosphate-based glasses, *J. Mater. Chem.* **19** 690–701 (2009).
 31. R. Casasola, J. M. Rincón, and M. Romero, Glass–ceramic glazes for ceramic tiles: a review, *J. Mater. Sci.* **47** 553–582 (2012).
 32. A. Sakamoto and S. Yamamoto, Glass-ceramics: engineering principles and applications, *Int. J. Appl. Glass Sci.* **1** 237–247 (2010).
 33. A. Yasumori, Preparation of functional glasses and glass ceramics using stable immiscibility, *J. Ceram. Soc. Jpn.* **121** 471–479 (2013).
 34. R. E. Mould, The strength of inorganic glasses, In: L. J. Bonis, J. J. Duga, and J. J. Gilman, eds, *Fundamental Phenomena in the Materials Sciences* **4** 119–149 (1967), New York, NY, Plenum Press.
 35. A. K. Varshneya, Stronger glass products: Lessons learned and yet to be learned, *Int. J. Appl. Glass Sci.* **9** 140–155 (2018).
 36. A. K. Varshneya, Chemical strengthening of glass: Lessons learned and yet to be learned, *Int. J. Appl. Glass Sci.* **1** 131–142 (2010).
 37. W. H. Zachariasen, The atomic arrangement in glass, *J. Am. Chem. Soc.* **54** 3841–3851 (1932).
 38. B. E. Warren and J. Biscob, Fourier analysis of X-ray patterns of soda-silica glass, *J. Am. Ceram. Soc.* **21** 259–265 (1938).

39. J. J. Hudgens and S. W. Martin, Glass transition and infrared spectra of low-alkali, anhydrous lithium phosphate glasses, *J. Am. Ceram. Soc.* **76** 1691–1696 (1993).
40. D. E. C. Corbridge, Crystallographic data on some Kurrol salts, *Acta Crystallogr.* **8** 520 (1955).
41. M. Bagieu-Beucher, I. Tordjman, A. Durif, and J. C. Guitel, Structure cristalline du trimétaphosphate de potassium $K_3P_3O_9$, *Acta Crystallogr. B* **32** 1427–1430 (1976).
42. K. Momma and F. Izumi, VESTA 3 for three-dimensional visualization of crystal, volumetric and morphology data, *J. Appl. Crystallogr.* **44** 1272–1276 (2011).
43. J. Murach and R. Brückner, Preparation and structure-sensitive investigations on silica glass fibers, *J. Non-Cryst. Solids* **211** 250–261 (1997).
44. H. Stockhorst and R. Brückner, Structure sensitive measurements on phosphate glass fibers, *J. Non-Cryst. Solids* **85** 105–126 (1986).
45. J. Murach and R. Brückner, Structure-sensitive investigations on alkali metasilicate glass fibers, *J. Non-Cryst. Solids* **204** 282–293 (1996).
46. K. Kikutani and W. Takarada, Methods of birefringence measurement and examples of data analysis, *Sen'i Gakkaishi* **66** 39–44 (2010) (in Japanese).
47. S. Inaba, H. Hosono, and S. Ito, Entropic shrinkage of an oxide glass, *Nat. Mater.* **14** 312–317 (2015).
48. S. Inaba, Y. Benino, S. Kohara, H. Hosono, and S. Ito, Anisotropic structure of alkali metaphosphate glasses, *J. Am. Ceram. Soc.* **103** 3631–3641 (2020).
49. X. Yang, G. Scannell, C. Jain, B. P. Rodrigues, M. A. Schmidt, and L. Wondraczek, Permanent structural anisotropy in a hybrid fiber optical waveguide, *Appl. Phys. Lett.* **111** 201901 (2017).
50. C. Jain, B. P. Rodrigues, T. Wieduwilt, J. Kobelke, L. Wondraczek, and M. A. Schmidt, Silver metaphosphate glass wires inside silica fibers—a new approach for hybrid optical fibers, *Opt. Express* **24** 3258–3267 (2016).
51. R. Schellekens and C. Bastiaansen, The drawing behavior of polyvinylalcohol fibers, *J. Appl. Polym. Sci.* **43** 2311–2315 (1991).
52. P. Smith and P. J. Lemstra, Ultra-high-strength polyethylene filaments by solution spinning/drawing, *J. Mater. Sci.* **15** 505–514 (1980).
53. P. R. Pinnock and I. M. Ward, Mechanical and optical anisotropy in polyethylene terephthalate fibres, *Br. J. Appl. Phys.* **15** 1559–1568 (1964).
54. C. L. Choy, Y. W. Wong, G. W. Yang, and T. Kanamoto, Elastic modulus and thermal conductivity of ultradrawn polyethylene, *J. Polym. Sci., Part B: Polym. Phys.* **37** 3359–3367 (1999).
55. C. L. Choy, W. H. Luk, and F. C. Chen, Thermal conductivity of highly oriented polyethylene, *Polymer* **19** 155–162 (1978).
56. V. Singh, T. L. Bougher, A. Weathers, Y. Cai, K. Bi, M. T. Pettes, S. A. McMenamin, W. Lv, D. P. Resler, T. R. Gattuso, D. H. Altman, K. H. Sandhage, L. Shi, A. Henry, and B. A. Cola, High thermal conductivity of chain-oriented amorphous polythiophene, *Nat. Nanotechnol.* **9** 384–390 (2014).

Chapter 2: Structural investigation of alkali metaphosphate glasses for significant anisotropy by analysis of ^{31}P MAS NMR, Raman, and FTIR spectra, and DFT calculations

2.1 Introduction

Mixed alkali metaphosphate glasses of $16.7\text{Li}_2\text{O}-16.7\text{Na}_2\text{O}-16.7\text{K}_2\text{O}-50\text{P}_2\text{O}_5$ (mol%, $(\text{Li,Na,K})\text{PO}_3$) and $12.5\text{Li}_2\text{O}-12.5\text{Na}_2\text{O}-12.5\text{K}_2\text{O}-12.5\text{Cs}_2\text{O}-50\text{P}_2\text{O}_5$ (mol%, $(\text{Li,Na,K,Cs})\text{PO}_3$) show much larger birefringence (significant anisotropic structures) compared to $50\text{Li}_2\text{O}-50\text{P}_2\text{O}_5$ (mol%, LiPO_3) and $50\text{Na}_2\text{O}-50\text{P}_2\text{O}_5$ (mol%, NaPO_3) metaphosphate glasses due to highly oriented $-\text{P}-\text{O}-\text{P}-$ chains when the glasses were deformed under uniaxial tensile stress above the glass transition temperature (T_g) [1,2]. As a mechanism for the formation of the significant anisotropic structures in $(\text{Li,Na,K,Cs})\text{PO}_3$ glass, Inaba et al. proposed a model that orientation of local structures with small force constant between alkali cation and oxygen ($F_{\text{M-O}}$) adjacent to Na^+ , K^+ , and Cs^+ cations occurs during the suppression of shear flow between chains by local structures with large $F_{\text{M-O}}$ adjacent to Li^+ cations which act as pseudo-cross-linked structures [1,2]. However, there is not enough evidence of the large distribution of $F_{\text{M-O}}$ for $(\text{Li,Na,K})\text{PO}_3$ and $(\text{Li,Na,K,Cs})\text{PO}_3$ glasses. In addition, although Q^2 units form chain and ring arrangement of PO_4 tetrahedra, ratios of Q^2 units in chains to total Q^2 units for alkali metaphosphate glasses are still unknown. In this study, structures for alkali metaphosphate glasses were investigated by analyzing ^{31}P magic angle spinning nuclear magnetic resonance (MAS NMR), Raman, and Fourier transform infrared (FTIR) spectra to clarify structural features causing the easy orientation of $-\text{P}-\text{O}-\text{P}-$ chains of $(\text{Li,Na,K})\text{PO}_3$ glass because clarification of the structural features will be useful knowledge for the development of anisotropic glasses. Assignments of peaks in these spectra are important to accurately understand the glass structures. The relationships between structure and peak wavenumbers of phosphate crystals were used for assignments of peaks of IR spectra of phosphate glasses [3,4]. In this study, we also investigated vibration modes of alkali metaphosphate and pyrophosphate crystals by density functional theory (DFT) calculations of Raman and infrared (IR) spectra to verify the interpretation of peak assignments reported in previous studies.

2.2 Experimental Procedure

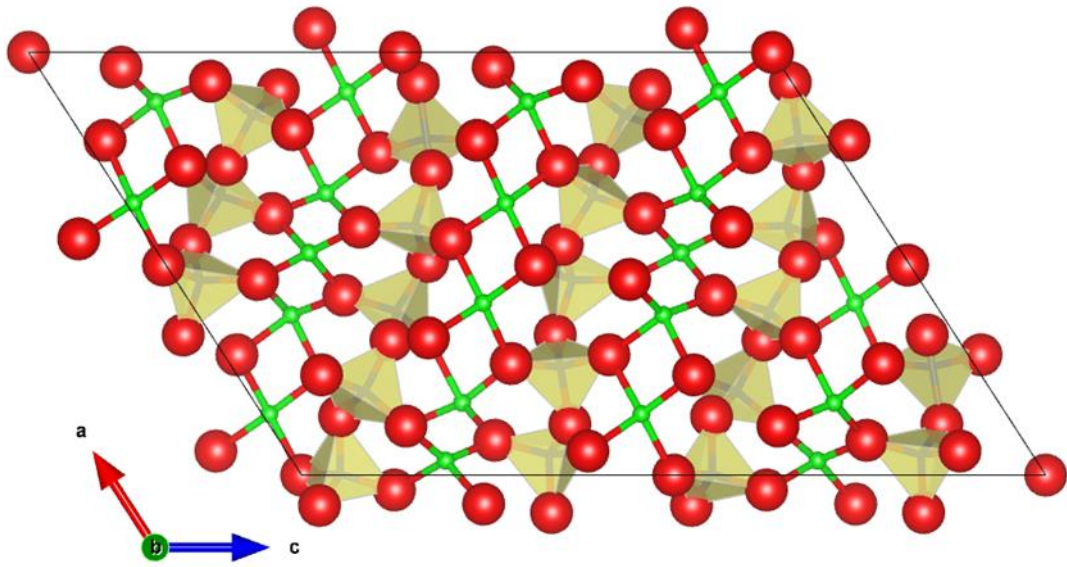
Starting materials of $50\text{Li}_2\text{O}-50\text{P}_2\text{O}_5$ (mol%, LiPO_3), $50\text{Na}_2\text{O}-50\text{P}_2\text{O}_5$ (mol%, NaPO_3), and $50\text{K}_2\text{O}-50\text{P}_2\text{O}_5$ (mol%, KPO_3) (> 99.7%, Rasa Industries, Japan) were weighted and mixed to obtain batches with compositions of either LiPO_3 , NaPO_3 , $(\text{Li,Na})\text{PO}_3$, or $(\text{Li,Na,K})\text{PO}_3$. The powder batches were melted in a platinum crucible at 1000°C for 1 h. The melts were cast in a graphite mold. The glass plates of LiPO_3 , $(\text{Li,Na})\text{PO}_3$, or $(\text{Li,Na,K})\text{PO}_3$ were annealed at 349 , 266 , or 237°C , respectively, (i.e., $T_g + 15^\circ\text{C}$) for 1 h and then cooled gradually to room temperature. The glass plate of NaPO_3 was annealed at 250°C (i.e., $T_g - 42^\circ\text{C}$) for 1 h and then cooled gradually to room temperature to prevent crystallization of NaPO_3 glass. The T_g of the annealed glasses was measured by differential thermal analysis using a thermal analyzer (TG/DTA 6300,

Seiko Instrument Inc.) at a heating rate of 10 °C min⁻¹. The annealed glasses were analyzed by ³¹P MAS NMR, Raman, and FTIR spectra.

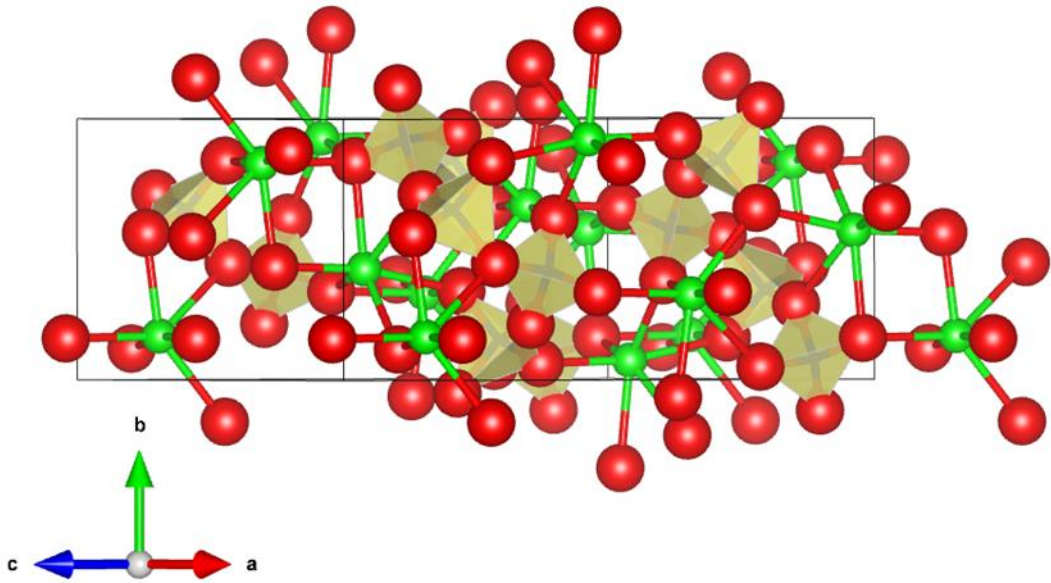
The ³¹P MAS NMR spectra were obtained with a solid-state NMR spectrometer (JNM-ECA600, JEOL, Japan). Chemical shifts were referenced to (NH₄)₂HPO₄ at 1.6 ppm versus H₃PO₄ 85% solution. All spectra were acquired at a magic angle spinning speed of 22 kHz and 64 scans were accumulated using a 30° pulse width and a 240 s pulse delay. The Raman spectra were obtained with a Raman spectrometer (LabRAM HR Evolution, Horiba, Japan), using a backscattering geometry. The wavelength of the excitation laser was 532 nm. The FTIR spectra were obtained with an FTIR spectrometer (Nicolet 6700, Thermo Fisher Scientific, MA) in reflectance mode at quasinormal incidence (10°). The reflectance spectra were analyzed by the Kramers–Kronig transformation to obtain absorption coefficient spectra [5]. The Raman and FTIR spectra were deconvoluted by a least square method using the Gaussian function.

Calculations of plane wave DFT of LiPO₃, NaPO₃, and KPO₃ metaphosphate crystals with chains composed of Q² units, and 67Na₂O–33P₂O₅ (mol%, Na₄P₂O₇) pyrophosphate crystal with dimers composed of Q¹ units were performed using the Quantum ESPRESSO (v6.6) package [6,7]. The Perdew-Zunger exchange-correlation functional of the local density approximation (LDA) was used. Pseudopotentials were norm-conserving scalar relativistic types. The pseudopotentials (Li.pz-n-vbc.UPF, Na.pz-n-vbc.UPF, K.pz-n-vbc.UPF, P.pz-bhs.UPF, and O.pz-mt.UPF) are listed in the pseudopotential table at www.quantum-espresso.org under the sub-category “original QE PP table.” LDA is known to reproduce frequencies of Raman and IR spectra for oxides in good agreement with experiments [8]. The plane-wave energy cutoffs (ecutwfc) for the wave functions and the charge density (ecutrho) were set at 150 Rydberg and 600 Rydberg (4 × ecutwfc), respectively. The k-point mesh was 2×2×2. A structure relaxation including optimization of the lattice parameters and the atomic positions in a cell with keeping the Bravais lattice of experimental crystals [9–11] was carried out. **Figure 2.1** shows structures of the experimental crystals [9–11]. Raman and IR spectra were calculated using the relaxed structures. The calculated spectra were analyzed using Winmostar v10.5.4 software (X-Ability Co., Ltd., Japan).

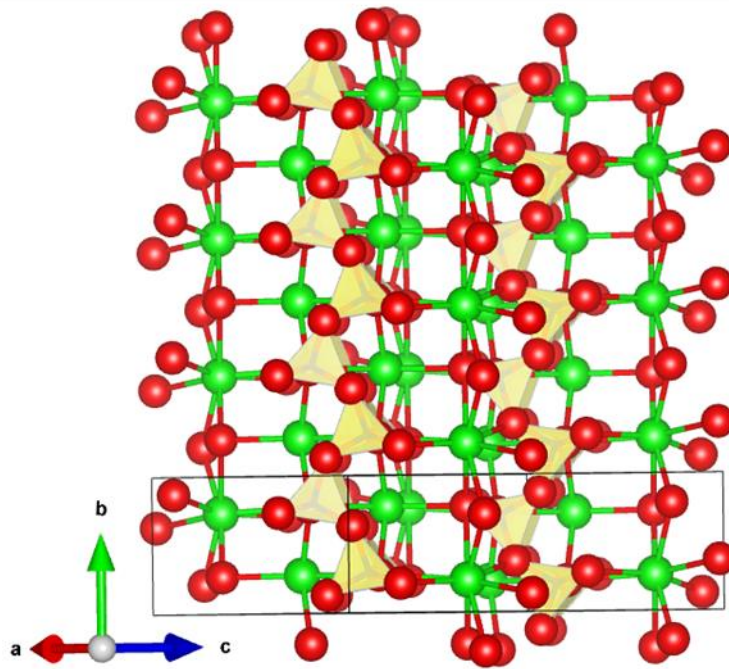
LiPO₃ crystal with chain



NaPO₃ crystal with chain



KPO₃ crystal with chain



Na₄P₂O₇ crystal with dimer

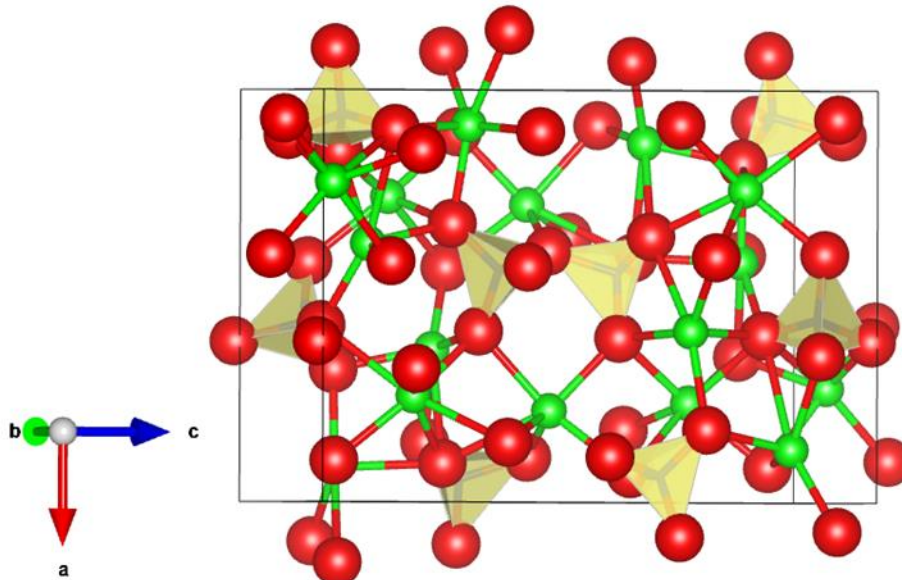
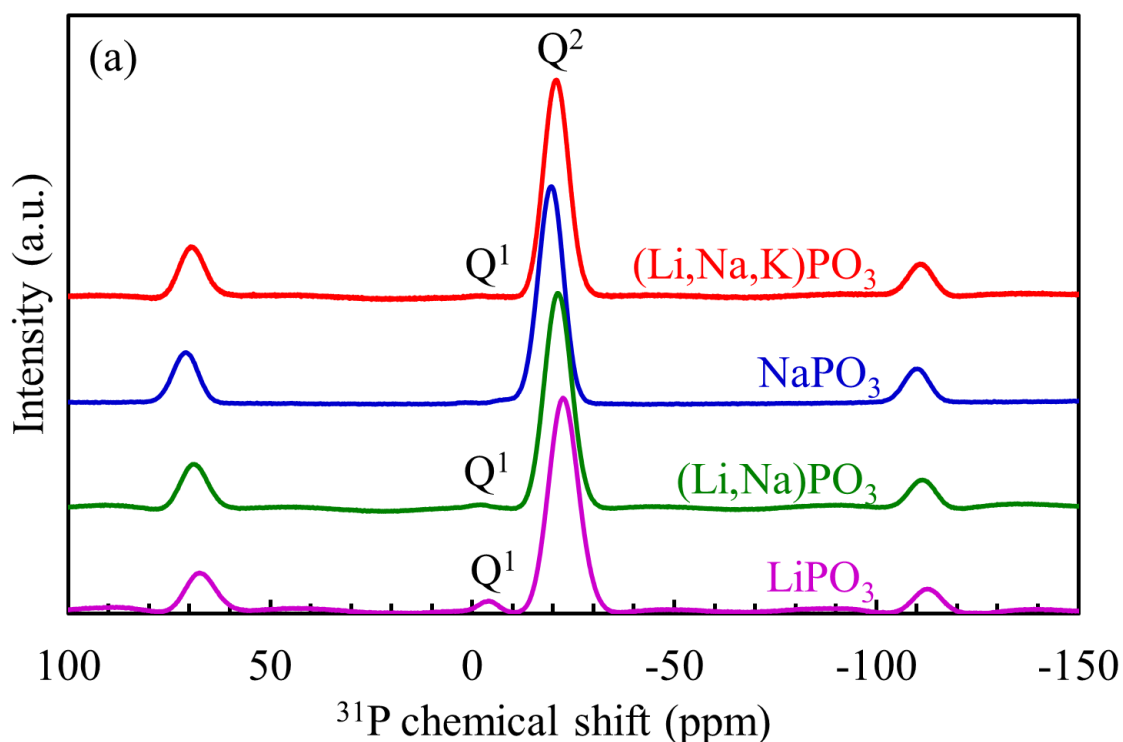


Fig. 2.1 Crystal structures of LiPO₃, NaPO₃, KPO₃ metaphosphate glasses with chains, and Na₄P₂O₇ pyrophosphate crystal with dimers [9–11]. Yellow tetrahedra and red and green balls are PO₄ tetrahedra, oxygen atoms, and alkali cations. (Drawn by VESTA ver. 3.5.7 [12])

2.3 Results and Discussion

2.3.1 Determination of local structure by analysis of ^{31}P MAS NMR spectra

Figure 2.2 shows ^{31}P MAS NMR spectra of LiPO_3 , NaPO_3 , $(\text{Li,Na})\text{PO}_3$, and $(\text{Li,Na,K})\text{PO}_3$ metaphosphate glasses. The NMR spectra of LiPO_3 , $(\text{Li,Na})\text{PO}_3$, and $(\text{Li,Na,K})\text{PO}_3$ glasses in **Fig. 2.2** are reported in our previous study [1]. Prominent peaks observed around -20 ppm and low-intensity peaks observed around -2 ppm are assigned to Q^2 and Q^1 units, respectively [13]. The NMR spectra suggest that Q^2 units are the majority units building the network structure of the alkali metaphosphate glasses. There was no detectable Q^1 peak for NaPO_3 glass. Since Q^3 units do not exist in alkali metaphosphate glasses because of pseudo-reaction represented as $2\text{Q}^2 + \text{R}_2\text{O} \rightarrow 2\text{Q}^1$ [13,14], no peak derived from Q^3 units was observed in the ^{31}P MAS NMR spectra in this study. **Table 2.1** summarizes the relative peak area of Q^1 and Q^2 peaks in the NMR spectra. The number of Q^2 units, therefore, increases in the order of LiPO_3 , $(\text{Li,Na})\text{PO}_3$, $(\text{Li,Na,K})\text{PO}_3$, and NaPO_3 glasses because the glasses are composed of the same number of PO_4 units and relative fraction of Q^2 units increases in the order of LiPO_3 , $(\text{Li,Na})\text{PO}_3$, $(\text{Li,Na,K})\text{PO}_3$, and NaPO_3 glasses.



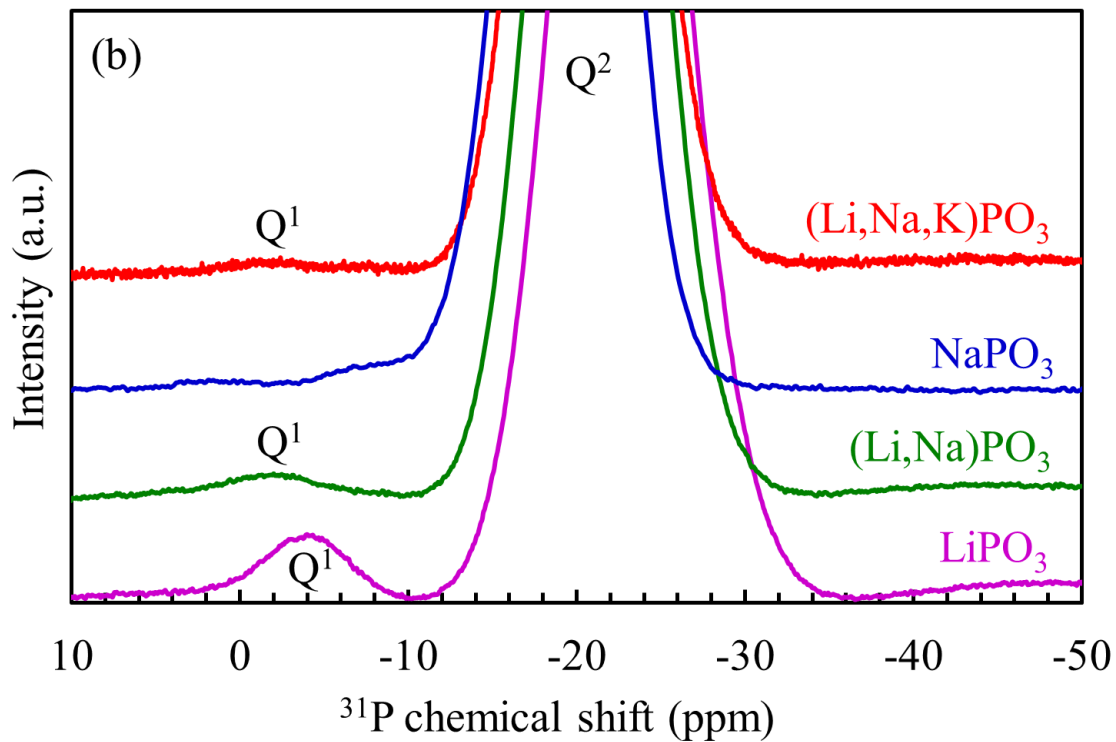


Fig. 2.2 (a) ^{31}P MAS NMR spectra of LiPO_3 , NaPO_3 , $(\text{Li,Na})\text{PO}_3$, and $(\text{Li,Na,K})\text{PO}_3$ metaphosphate glasses. (b) The enlarged figure of (a). Peaks observed around 70 ppm and -110 ppm are spinning sidebands. Reproduced with permission from Ref. [1]. Copyright 2014, Nature Publishing Group.

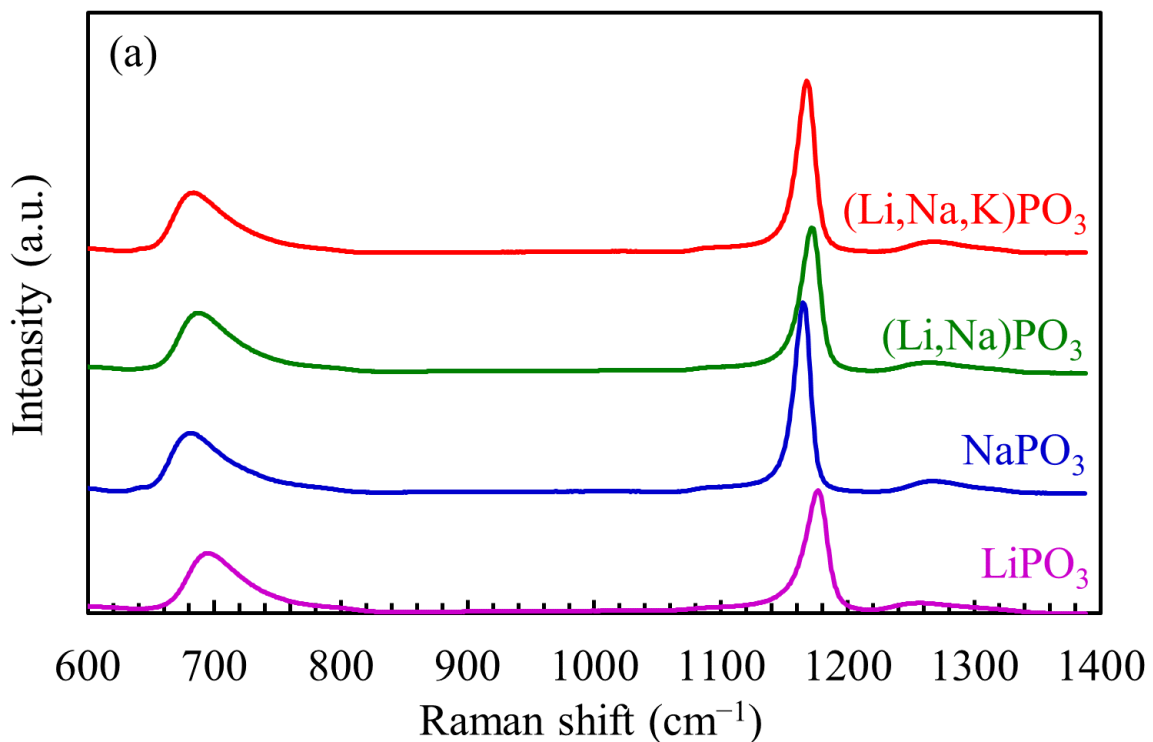
Table 2.1 Relative peak area of Q^1 and Q^2 peaks in NMR spectra for LiPO_3 , NaPO_3 , $(\text{Li,Na})\text{PO}_3$, and $(\text{Li,Na,K})\text{PO}_3$ glasses.

	LiPO_3	NaPO_3	LiNaPO_3	LiNaKPO_3
Q^1 units	3.4%	0%	2.7%	1.3%
		(Not detected)		
Q^2 units	96.6%	100%	97.3%	98.7%

2.3.2 Determination of local structure by analysis of Raman spectra

Raman spectra normalized by the intensity of peaks in the range $620\text{--}820\text{ cm}^{-1}$ of LiPO_3 , NaPO_3 , $(\text{Li,Na})\text{PO}_3$, and $(\text{Li,Na,K})\text{PO}_3$ glasses are shown in **Fig. 2.3 (a)**. The peaks in the range $620\text{--}820\text{ cm}^{-1}$ and $1070\text{--}1220\text{ cm}^{-1}$ are assigned to symmetric stretching vibrations of $-\text{P}-\text{O}-\text{P}-$ and $\text{NBO}-\text{P}-\text{NBO}$ bonds, respectively (**Fig. 2.4**) [15]. **Figure 2.3 (b)** shows measured spectrum and deconvoluted peaks of $(\text{Li,Na,K})\text{PO}_3$ glass in the range $600\text{--}850\text{ cm}^{-1}$. The measured spectrum is deconvoluted into three peaks

assigned to symmetric stretching vibrations of $-P-O-P-$ bonds in chains, large rings, and small rings in ascending order of Raman shift [16]. **Figure 2.3 (c)** shows measured spectrum and deconvoluted peaks of $(Li,Na,K)PO_3$ glass in the range $1050-1250\text{ cm}^{-1}$. The measured spectrum is deconvoluted into three peaks assigned to symmetric stretching vibrations of NBO-P-NBO bonds of small rings, large rings, and chains in ascending order of Raman shift [16]. In addition, peaks associated with Q^1 units appear near 760 cm^{-1} and 1050 cm^{-1} in Raman spectra of phosphate glasses [17,18]. The influence of the peaks associated with Q^1 units for $LiPO_3$, $(Li,Na)PO_3$, and $(Li,Na,K)PO_3$ glasses on deconvolution of Raman spectra was quite small because the relative fraction of Q^2 units was much larger than that of Q^1 units for the glasses as shown in **Table 2.1**.



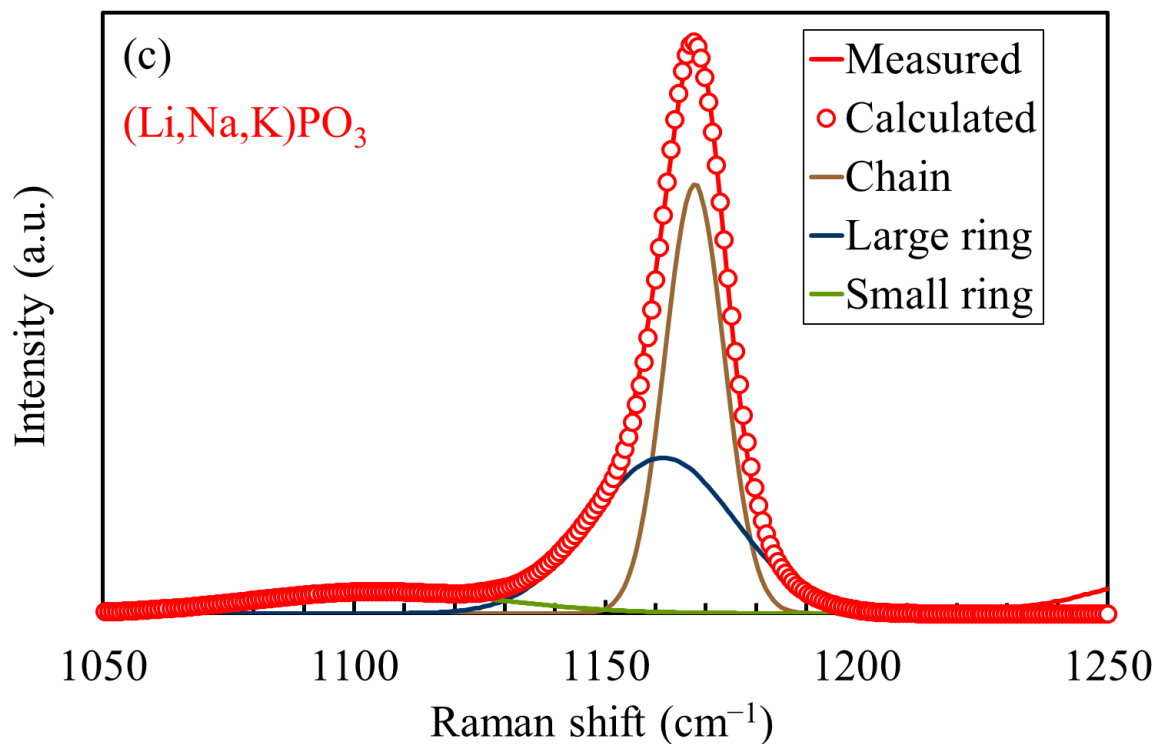
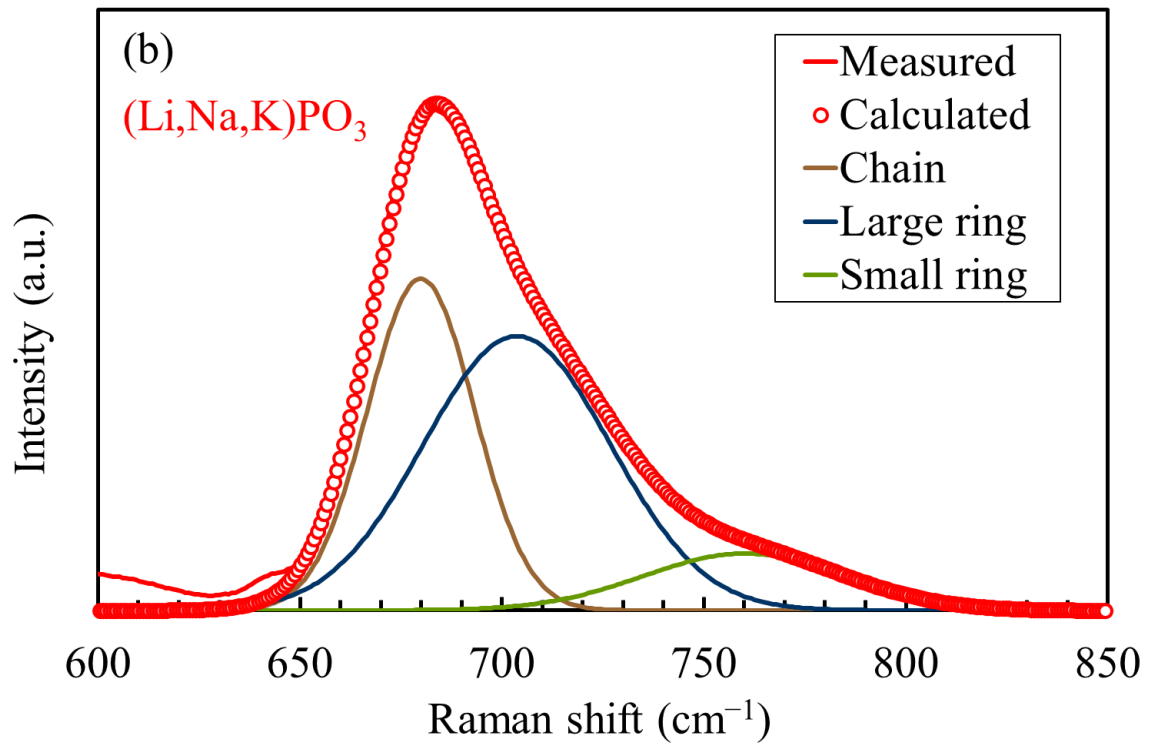
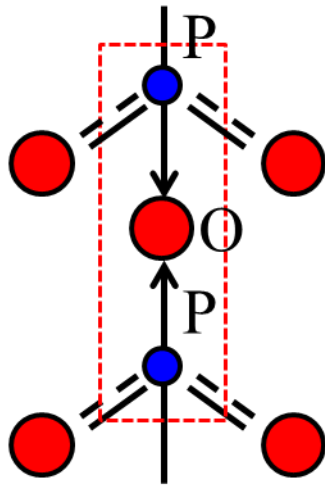
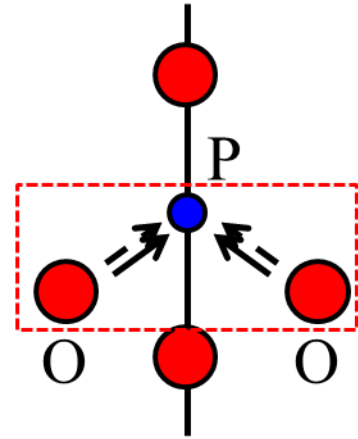


Fig. 2.3 (a) Raman spectra of LiPO₃, NaPO₃, (Li,Na)PO₃, and (Li,Na,K)PO₃ metaphosphate glasses. Raman spectrum and deconvoluted peaks of (Li,Na,K)PO₃ metaphosphate glass in the range (b) 600–850 cm⁻¹ and (c) 1050–1250 cm⁻¹.



Symmetric stretching vibration
of $-P-O-P-$ bond



Symmetric stretching vibration
of $NBO-P-NBO$ bond

Fig. 2.4 Symmetric stretching vibrations of $-P-O-P-$ and $NBO-P-NBO$ bonds

From deconvoluted peaks in the range $600-850\text{ cm}^{-1}$ and $1070-1220\text{ cm}^{-1}$, relative peak area (A_R), which is relative fraction of Q^2 units in chains to total Q^2 units, was calculated using the following equation:

$$A_R = \frac{A_C}{A_C + A_{LR} + A_{SR}} \times 100 \quad (2.1)$$

where A_C , A_{LR} , and A_{SR} are peak areas assigned to symmetric stretching vibrations of $-P-O-P-$ bonds in chains, large rings, and small rings, respectively, and symmetric stretching vibrations of $NBO-P-NBO$ bonds in chains, large rings, and small rings, respectively. **Figure 2.5** shows A_R of $LiPO_3$, $NaPO_3$, $(Li,Na)PO_3$, and $(Li,Na,K)PO_3$ metaphosphate glasses. A_R of $NaPO_3$ and $(Li,Na,K)PO_3$ glasses is larger than that of $LiPO_3$ and $(Li,Na)PO_3$ glasses.

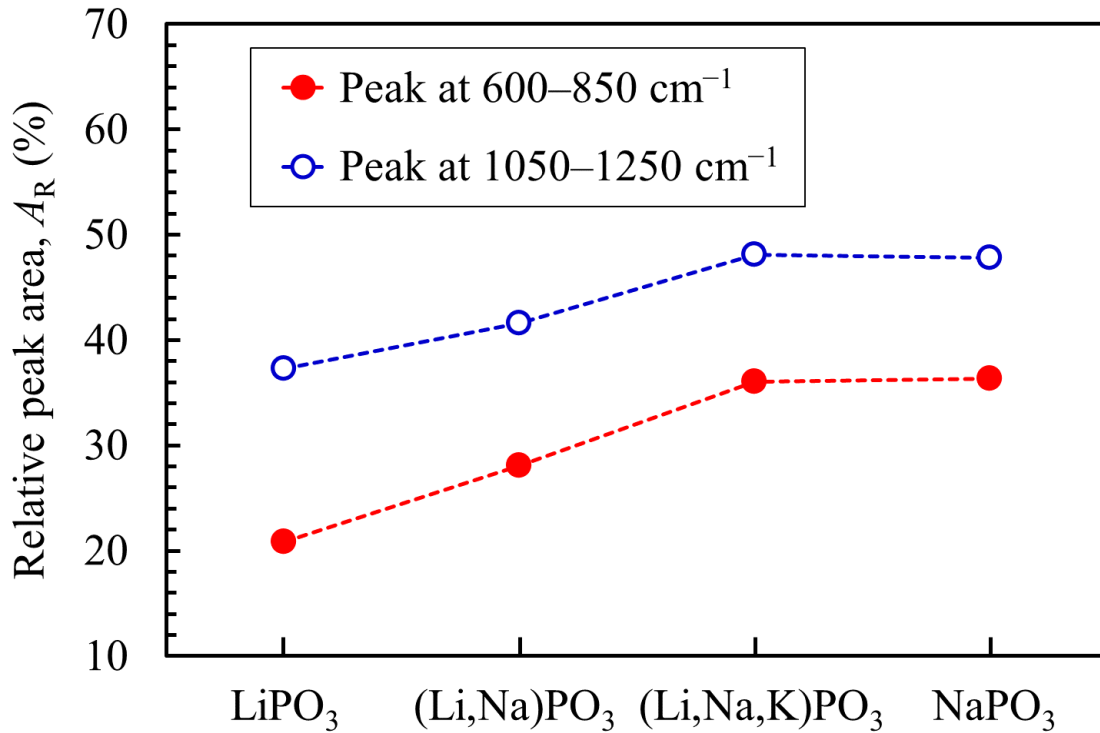


Fig. 2.5 Relative peak area (A_R) calculated by deconvoluted peaks of Raman spectra for LiPO_3 , NaPO_3 , $(\text{Li,Na})\text{PO}_3$, and $(\text{Li,Na,K})\text{PO}_3$ metaphosphate glasses.

2.3.3 Determination of local structure by analysis of FTIR spectra in the mid-infrared region

Figure 2.6 (a) shows absorption coefficient spectra of LiPO_3 , NaPO_3 , $(\text{Li,Na})\text{PO}_3$, and $(\text{Li,Na,K})\text{PO}_3$ metaphosphate glasses in the range $800\text{--}1400\text{ cm}^{-1}$. **Figure 2.6 (b)** shows the absorption coefficient spectrum and deconvoluted peaks of $(\text{Li,Na,K})\text{PO}_3$ glass. The measured spectrum is deconvoluted into seven peaks assigned to vibration of Q^n units ($n = 1\text{--}3$) according to peak assignment in literature [19,20]. **Table 2.2** summarizes assignments for the deconvoluted peaks. Since Q^3 units do not exist in LiPO_3 , NaPO_3 , $(\text{Li,Na})\text{PO}_3$, and $(\text{Li,Na,K})\text{PO}_3$ metaphosphate glasses as mentioned above [13,14], peak 7 in **Table 2.2** was not used for the deconvolution.

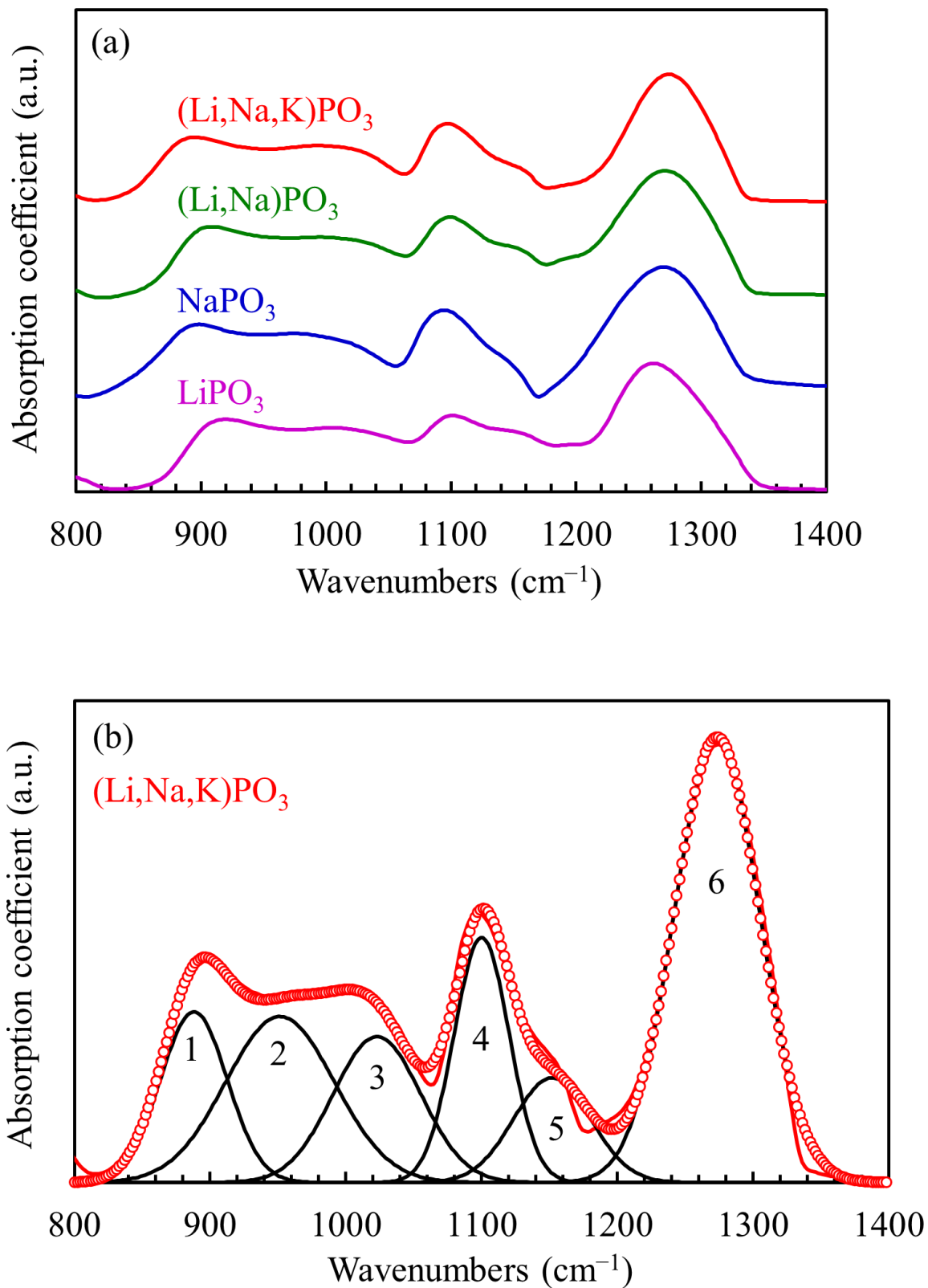


Fig. 2.6 (a) Absorption coefficient spectra of LiPO₃, NaPO₃, (Li,Na)PO₃, and (Li,Na,K)PO₃ metaphosphate glasses in the range 800–1400 cm^{-1} . (b) Absorption coefficient spectrum and deconvoluted peaks of (Li,Na,K)PO₃ metaphosphate glass in the range 800–1400 cm^{-1} . Open circles represent values of summation of deconvoluted peaks.

Table 2.2 Assignments of deconvoluted peaks of absorption coefficient spectra of LiPO₃, NaPO₃, (Li,Na)PO₃, and (Li,Na,K)PO₃ metaphosphate glasses in the range 800–1400 cm⁻¹.

Peak	Assignment
1	$\nu_{as}(\text{P-O-P})$, Q ² units in chains
2	$\nu_{as}(\text{P-O-P})$, Q ² units in large rings
3	$\nu_{as}(\text{P-O-P})$, Q ² units in small rings
4	$\nu_{as}(\text{PO}_3^{2-})$, end group of Q ¹ units
5	$\nu_s(\text{PO}_2^-)$, Q ² units
6	$\nu_{as}(\text{PO}_2^-)$, Q ² units
7	$\nu(\text{P=O})$, Q ³ units

Relative peak area (A_R), which is the relative fraction of Q² units in chains to total Q² units, was calculated using the following equation:

$$A_R = \frac{A_1}{A_1 + A_2 + A_3} \times 100 \quad (2.2)$$

where A_1 , A_2 , and A_3 , respectively, are peak areas assigned to asymmetric stretching vibrations of Q² units in chains (deconvoluted peak 1), large rings (deconvoluted peak 2), and small rings (deconvoluted peak 3).

Figure 2.7 shows A_R of LiPO₃, NaPO₃, (Li,Na)PO₃, and (Li,Na,K)PO₃ metaphosphate glasses. A_R of NaPO₃ and (Li,Na,K)PO₃ glasses is larger than that of LiPO₃ and (Li,Na)PO₃ glasses.

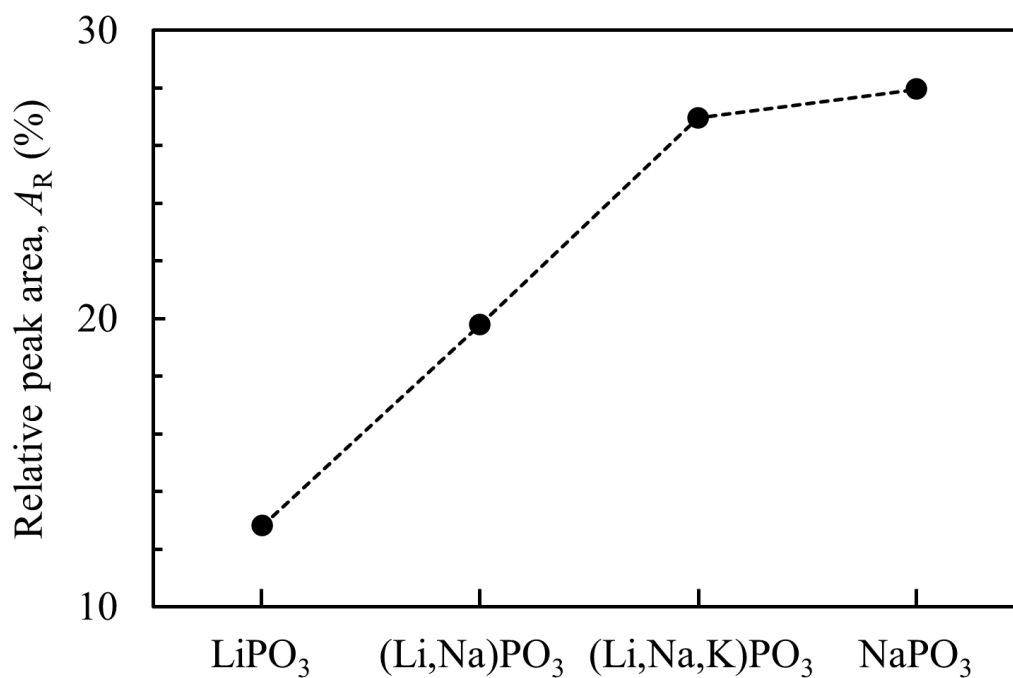
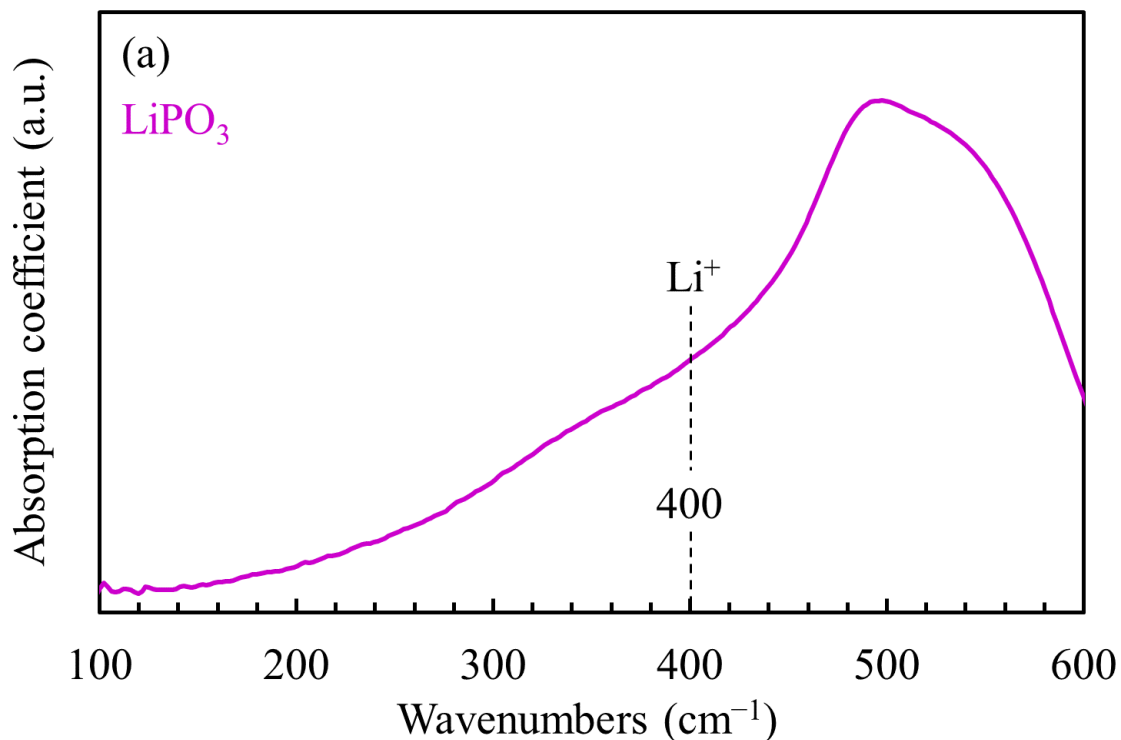


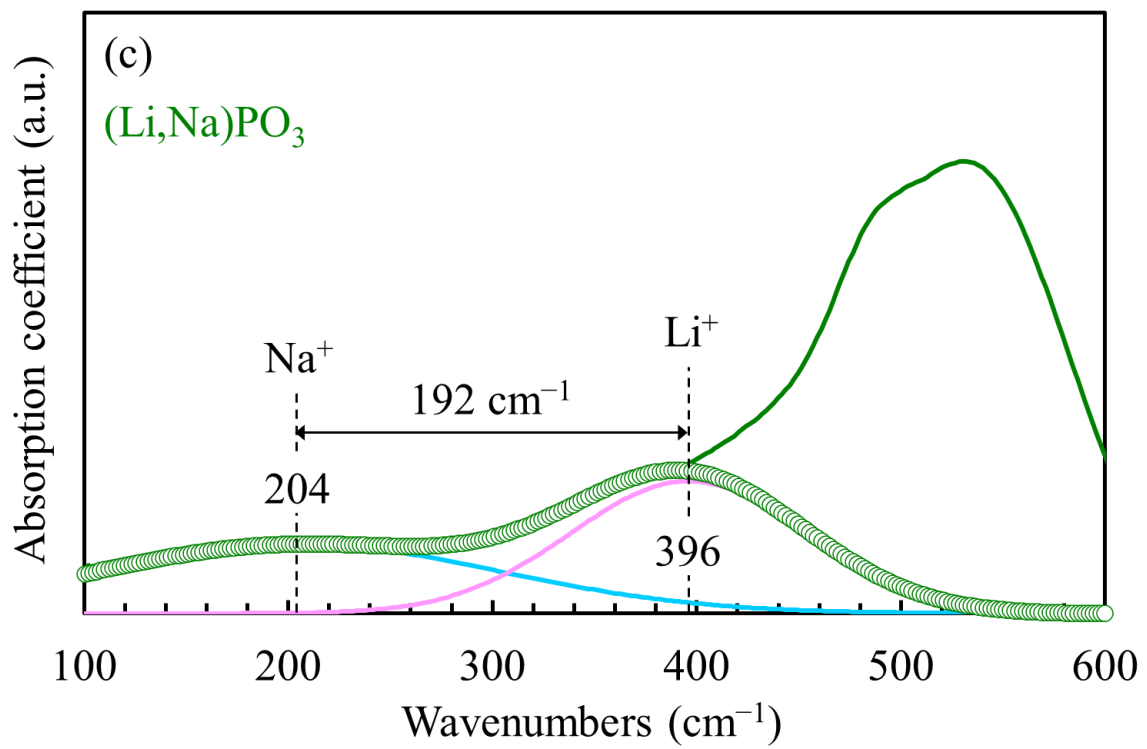
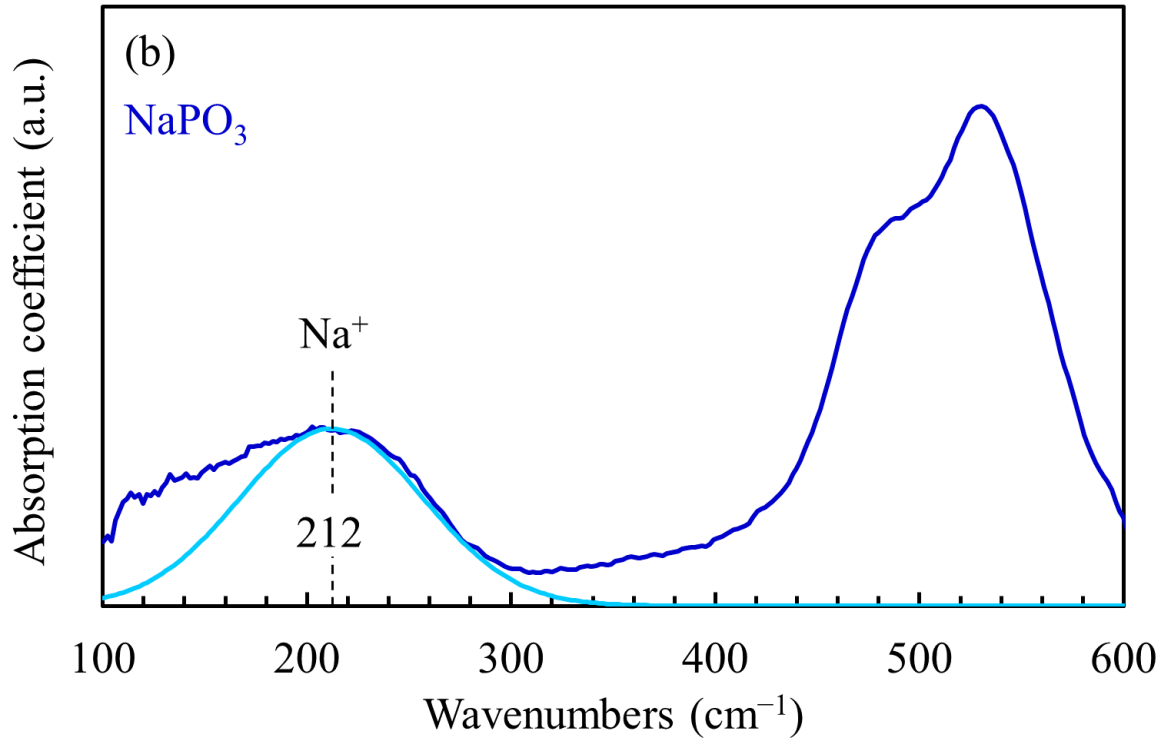
Fig. 2.7 Relative peak area (A_R) calculated by deconvoluted peaks of absorption coefficient spectra of LiPO₃, NaPO₃, (Li,Na)PO₃, and (Li,Na,K)PO₃ metaphosphate glasses.

From the analysis of ^{31}P MAS NMR, Raman, and FTIR spectra, the number of Q^2 units in chains for NaPO_3 and $(\text{Li,Na,K})\text{PO}_3$ glasses is equivalent because the number of Q^2 units and A_R for those glasses are comparable.

2.3.4 Determination of the distribution of force constant ($F_{\text{M-O}}$) by analysis of FTIR spectra in the far-infrared region

Since peaks in far-infrared absorption spectra are sensitive to the force constant between alkali cation and oxygen ($F_{\text{M-O}}$), the peaks were analyzed to investigate compositional dependence of the distribution of $F_{\text{M-O}}$. Wavenumbers of cation motion peaks become higher with increasing $F_{\text{M-O}}$, and those of LiPO_3 , NaPO_3 , and KPO_3 metaphosphate glasses are around 400, 212, and 147 cm^{-1} , respectively [21]. **Figure 2.8 (a)–(d)** show absorption coefficient spectra of LiPO_3 , NaPO_3 , $(\text{Li,Na})\text{PO}_3$, and $(\text{Li,Na,K})\text{PO}_3$ glasses, respectively. The cation motion peaks of LiPO_3 and NaPO_3 glasses are composed of one peak assigned to Li and Na motions, respectively. On the other hand, deconvoluted cation motion peaks of $(\text{Li,Na})\text{PO}_3$ and $(\text{Li,Na,K})\text{PO}_3$ glasses are composed of two peaks assigned to Li and Na motions and three peaks assigned to Li, Na, and K motions, respectively. This result is consistent with the tendency of previous studies that cation motion peaks in far-infrared absorption spectra of metaphosphate glasses containing alkaline earth cation and one kind of other modifier-cations are composed of multiple peaks [19,20,22]. In addition, a difference of peak wavenumbers between a peak originated from Li–O motion and a peak observed below 300 cm^{-1} for $(\text{Li,Na,K})\text{PO}_3$ glass ($\Delta_{\text{PW}} = 210 \text{ cm}^{-1}$) is larger than that for $(\text{Li,Na})\text{PO}_3$ glass ($\Delta_{\text{PW}} = 192 \text{ cm}^{-1}$). These observations indicate that the distribution of $F_{\text{M-O}}$ becomes larger with increasing the number of types of alkali cations in alkali metaphosphate glasses.





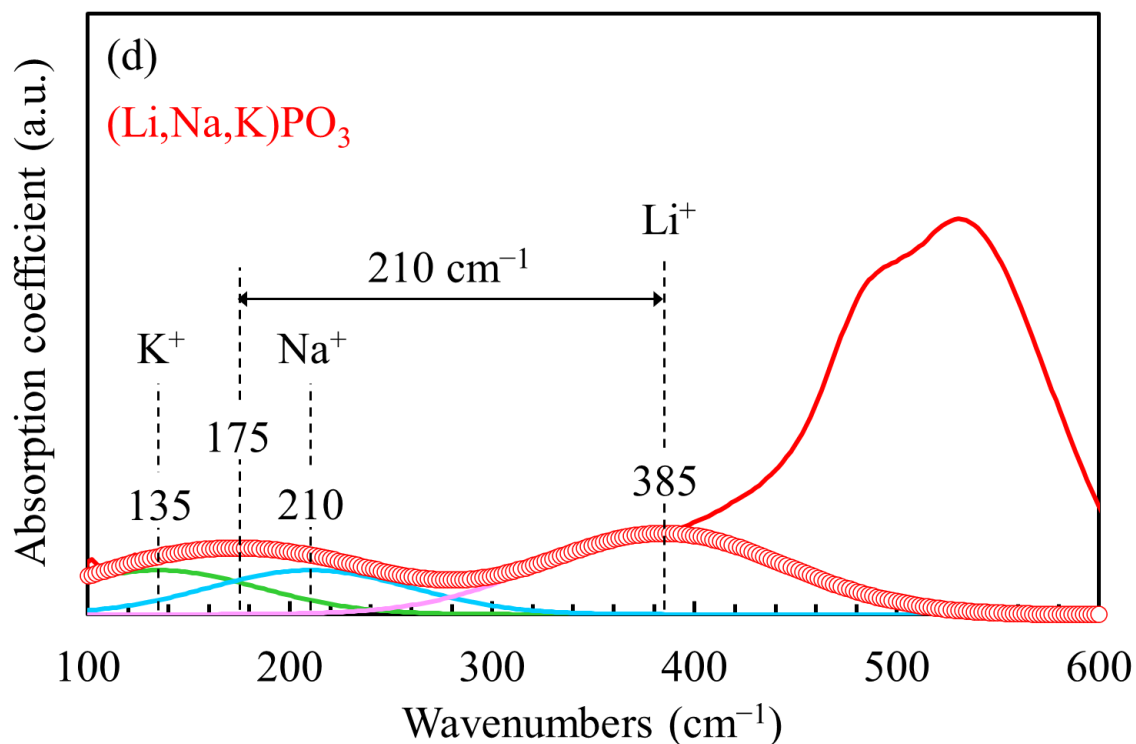


Fig. 2.8 Absorption coefficient spectra and deconvoluted peaks of (a) LiPO_3 and (b) NaPO_3 , (c) $(\text{Li,Na})\text{PO}_3$, and (d) $(\text{Li,Na,K})\text{PO}_3$ metaphosphate glasses in the range 100–600 cm^{-1} . Open circles represent values of summation of deconvoluted peaks.

2.3.5 DFT calculations of Raman and IR spectra

Although analysis of the ^{31}P MAS spectra for LiPO_3 , NaPO_3 , $(\text{Li,Na})\text{PO}_3$, and $(\text{Li,Na,K})\text{PO}_3$ glasses showed that amount of Q^1 units for the glasses were equal to or less than 3.4% as shown in **Table 2.1**, distinct peaks assigned to Q^1 units (Peak 4 in **Table 2.2**) were observed in the absorption coefficient spectra for the glasses. The interpretation of the assignments of the Raman and absorption coefficient spectra were verified by DFT calculation of Raman and IR spectra for LiPO_3 , NaPO_3 , and KPO_3 metaphosphate crystals with chains, and $\text{Na}_4\text{P}_2\text{O}_7$ pyrophosphate crystal. Deviations of lattice parameters between the experimental and relaxed structures were equal to or less than 3.2% as shown in **Table 2.3**.

Table 2.3 Lattice parameters of experimental [9–11] and relaxed structures of LiPO₃, NaPO₃, and KPO₃ metaphosphate crystals with chains, and Na₄P₂O₇ pyrophosphate crystals

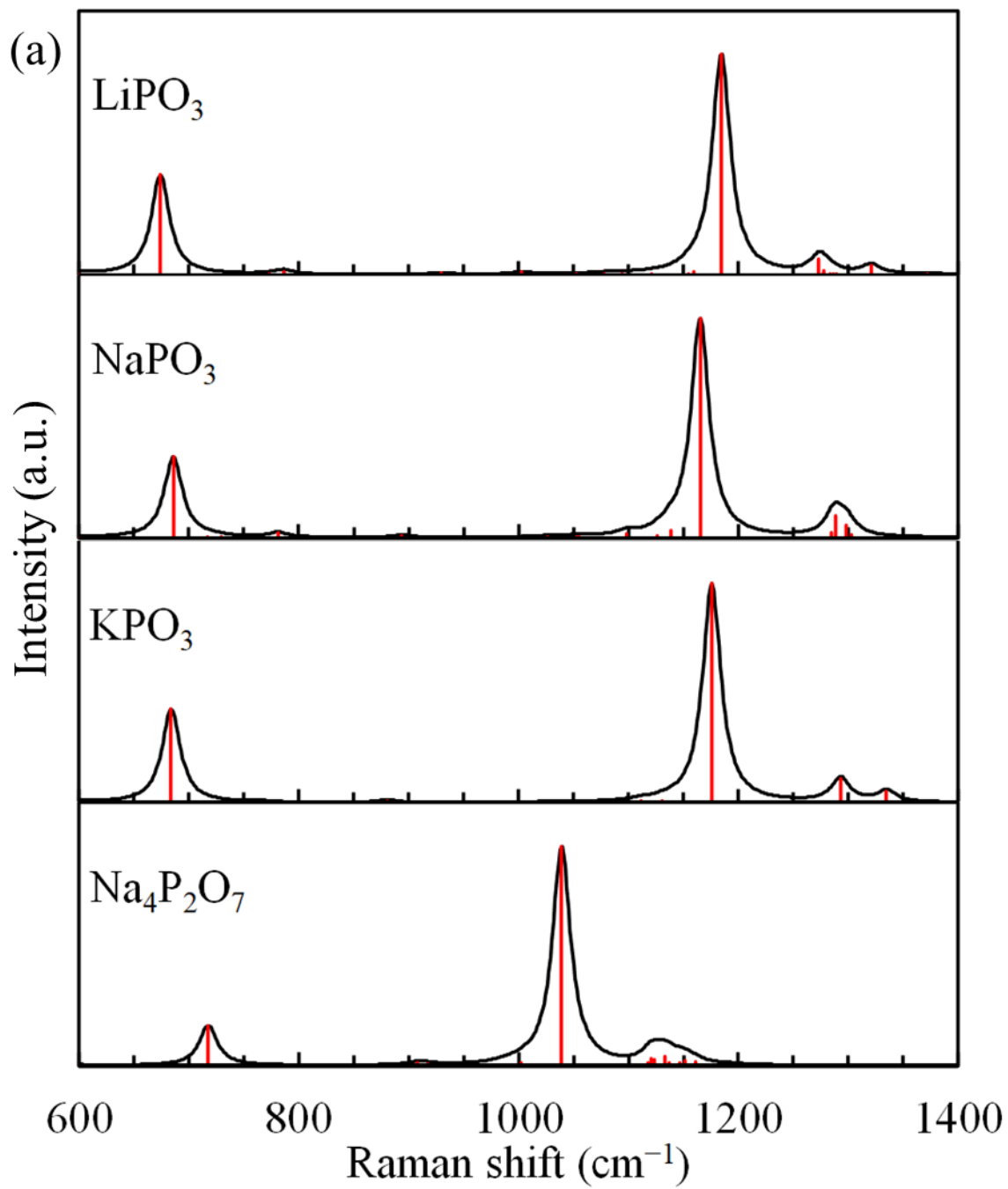
Crystal	Lattice parameters	Experimental structure	Relaxed structure	Deviation (%)
LiPO ₃ Chain	<i>a</i> (Å)	13.086	12.905	−1.4
	<i>b</i> (Å)	5.405	5.274	−2.4
	<i>c</i> (Å)	19.356	19.057	−1.5
	<i>α</i> (°)	90.000	90.000	0.0
	<i>β</i> (°)	122.905	122.852	0.0
	<i>γ</i> (°)	90.000	90.000	0.0
NaPO ₃ Chain	<i>a</i> (Å)	7.640	7.770	1.7
	<i>b</i> (Å)	6.020	6.069	0.8
	<i>c</i> (Å)	13.249	13.597	2.6
	<i>α</i> (°)	90.000	90.000	0.0
	<i>β</i> (°)	121.118	120.881	−0.2
	<i>γ</i> (°)	90.000	90.000	0.0
KPO ₃ Chain	<i>a</i> (Å)	10.280	10.310	0.3
	<i>b</i> (Å)	4.540	4.547	0.2
	<i>c</i> (Å)	14.020	14.200	1.3
	<i>α</i> (°)	90.000	90.000	0.0
	<i>β</i> (°)	101.500	101.035	−0.5
	<i>γ</i> (°)	90.000	90.000	0.0
Na ₄ P ₂ O ₇	<i>a</i> (Å)	9.367	9.663	2.4
	<i>b</i> (Å)	5.390	5.522	3.2
	<i>c</i> (Å)	13.480	13.728	1.8
	<i>α</i> (°)	90.000	90.000	0.0
	<i>β</i> (°)	90.000	90.000	0.0
	<i>γ</i> (°)	90.000	90.000	0.0

Figure 2.9 shows the calculated Raman and IR spectra of the crystals. Assignments of peaks of the calculated Raman and IR spectra are listed in **Table 2.4**. **Figure 2.10 and 2.11** show schematic illustrations of stretching vibrations of Q² and Q¹ units, respectively. Three or four peaks were observed in the Raman spectra of the alkali metaphosphate crystals. The peaks around 680 cm^{−1} in the Raman spectra were assigned to symmetric stretching vibrations of –P–O–P– bonds ($\nu_s(\text{P–O–P})$) with symmetric stretching vibrations of –O–P–O– bonds ($\nu_s(\text{O–P–O})$). The peaks around 1175 cm^{−1} and 1300 cm^{−1} in the Raman spectra, respectively, were assigned to symmetric ($\nu_s(\text{PO}_2^-)$) and asymmetric ($\nu_{as}(\text{PO}_2^-)$) stretching vibrations of P–NBO bonds of Q² units. On the other hand, three peaks were observed in the Raman spectrum of the pyrophosphate crystal. The peak at 718 cm^{−1} in the Raman spectrum was assigned to symmetric stretching vibrations of –P–O–P– bonds ($\nu_s(\text{P–O–P})$). The peaks at 1039 cm^{−1} and 1133 cm^{−1} in the Raman spectrum, respectively, were assigned to symmetric ($\nu_s(\text{PO}_3^{2-})$) and asymmetric ($\nu_{as}(\text{PO}_3^{2-})$) stretching vibrations of P–NBO bonds of Q¹ units.

Six or eight peaks were observed in the IR spectra of the alkali metaphosphate crystals. The peaks in the range 676–725 cm^{−1} were assigned to symmetric stretching vibrations of –P–O–P– bonds ($\nu_s(\text{P–O–P})$)

with symmetric stretching vibrations of $-\text{O}-\text{P}-\text{O}-$ bonds ($\nu_s(\text{O}-\text{P}-\text{O})$). The peaks around 780 cm^{-1} were assigned to symmetric stretching vibrations of $-\text{P}-\text{O}-\text{P}-$ bonds ($\nu_s(\text{P}-\text{O}-\text{P})$) with asymmetric stretching vibrations of $-\text{O}-\text{P}-\text{O}-$ bonds ($\nu_{as}(\text{O}-\text{P}-\text{O})$). The peaks around 900 cm^{-1} and at 1011 cm^{-1} were assigned to asymmetric stretching vibrations of $-\text{P}-\text{O}-\text{P}-$ bonds ($\nu_{as}(\text{P}-\text{O}-\text{P})$) with asymmetric stretching vibrations of $-\text{O}-\text{P}-\text{O}-$ bonds ($\nu_{as}(\text{O}-\text{P}-\text{O})$). The peaks at 1018 cm^{-1} and 1032 cm^{-1} were assigned to asymmetric stretching vibrations of $-\text{P}-\text{O}-\text{P}-$ bonds ($\nu_{as}(\text{P}-\text{O}-\text{P})$) with symmetric stretching vibrations of $-\text{O}-\text{P}-\text{O}-$ bonds ($\nu_s(\text{O}-\text{P}-\text{O})$). The peaks around 1100 cm^{-1} were assigned to symmetric stretching vibrations of $\text{P}-\text{NBO}$ bonds ($\nu_s(\text{PO}_2^-)$) and asymmetric stretching vibrations of $-\text{P}-\text{O}-\text{P}-$ bonds ($\nu_{as}(\text{P}-\text{O}-\text{P})$) with symmetric stretching vibrations of $-\text{O}-\text{P}-\text{O}-$ bonds ($\nu_s(\text{O}-\text{P}-\text{O})$). The peaks around 1160 cm^{-1} and 1290 cm^{-1} were, respectively, assigned to symmetric ($\nu_s(\text{PO}_2^-)$) and asymmetric ($\nu_{as}(\text{PO}_2^-)$) stretching vibrations of $\text{P}-\text{NBO}$ bond of Q^2 units. On the other hand, three peaks were observed in the IR spectrum of the pyrophosphate crystal. The peak at 717 cm^{-1} and 918 cm^{-1} in the IR spectrum were, respectively, assigned to symmetric ($\nu_s(\text{P}-\text{O}-\text{P})$) and asymmetric ($\nu_{as}(\text{P}-\text{O}-\text{P})$) stretching vibrations of $-\text{P}-\text{O}-\text{P}-$ bonds. The peak at 1142 cm^{-1} in the IR spectrum was assigned to asymmetric stretching vibrations of $\text{P}-\text{NBO}$ bonds of Q^1 units ($\nu_{as}(\text{PO}_3^{2-})$).

Reported assignments of peaks of Raman and IR spectra of phosphate crystals and glasses are listed in **Table 2.4** [3,17,22–25]. The assignments of peaks of the calculated Raman and IR spectra are consistent with reported assignments of phosphate crystals and glasses except for the assignment of the peaks around 1100 cm^{-1} of the calculated IR spectra for the alkali metaphosphate crystals. Peaks around 1100 cm^{-1} of IR spectra for phosphate crystals and glasses have been assigned to $\nu_{as}(\text{PO}_3^{2-})$ of Q^1 units. However, the calculated IR spectra showed that the peaks around 1100 cm^{-1} result from not only $\nu_{as}(\text{PO}_3^{2-})$ of Q^1 units but also $\nu_s(\text{PO}_2^-)$ and $\nu_{as}(\text{P}-\text{O}-\text{P})$ with $\nu_s(\text{O}-\text{P}-\text{O})$ of Q^2 units. Peak 4 around 1100 cm^{-1} in the absorption coefficient spectra for LiPO_3 , NaPO_3 , $(\text{Li},\text{Na},\text{K})\text{PO}_3$, and $(\text{Li},\text{Na},\text{K})\text{PO}_3$ glasses, therefore, must mainly result from stretching vibrations of Q^2 units because Q^2 units are majority units building network structure of the alkali metaphosphate glasses as shown in **Table 2.1**.



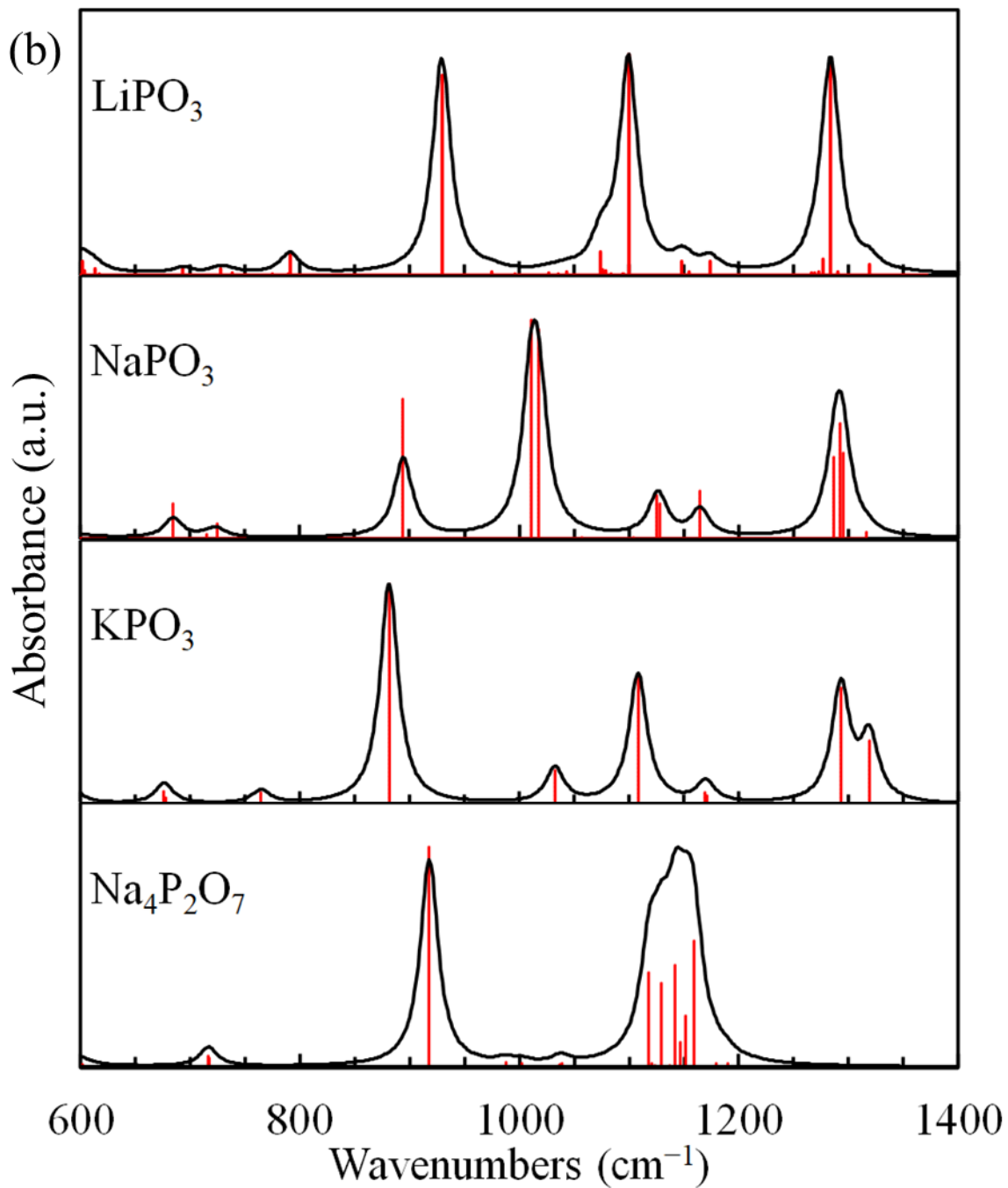
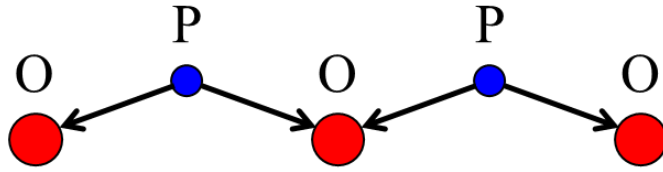


Fig. 2.9 Calculated (a) Raman and (b) infrared spectra of LiPO₃, NaPO₃, and KPO₃ metaphosphate crystals with chains, and Na₄P₂O₇ pyrophosphate crystal

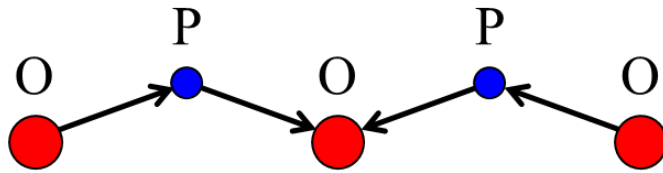
Table 2.4 Assignments of calculated Raman and infrared (IR) spectra of LiPO_3 , NaPO_3 , and KPO_3 metaphosphate crystals with chains, and $\text{Na}_4\text{P}_2\text{O}_7$ pyrophosphate crystal, and reported assignments of Raman and IR spectra of phosphate crystals and glasses [3,17,22–25]. ν_s and ν_{as} in the assignment are symmetric and asymmetric stretching vibrations, respectively.

LiPO ₃ crystal		NaPO ₃ crystal		KPO ₃ crystal		Na ₄ P ₂ O ₇ crystal		Phosphate glasses and crystals (Assignments in literature)			
Raman (cm ⁻¹)	IR (cm ⁻¹)	Raman (cm ⁻¹)	IR (cm ⁻¹)	Raman (cm ⁻¹)	IR (cm ⁻¹)	Raman (cm ⁻¹)	IR (cm ⁻¹)	Assignment	Raman (cm ⁻¹)	IR (cm ⁻¹)	Assignment
674		686	685 725	684	676			$\nu_s(\text{P-O-P})$ with $\nu_s(\text{O-P-O})$, Q ²	635– 835	650– 850	$\nu_s(\text{P-O-P})$, Q ² , Q ¹
						718	717	$\nu_s(\text{P-O-P})$, Q ¹			
	791				764			$\nu_s(\text{P-O-P})$ with $\nu_{as}(\text{O-P-O})$, Q ²			
	929		894 1011		881			$\nu_{as}(\text{P-O-P})$ with $\nu_{as}(\text{O-P-O})$, Q ²		850– 1055	$\nu_{as}(\text{P-O-P})$, Q ²
							918	$\nu_{as}(\text{P-O-P})$, Q ¹		900– 950	$\nu_{as}(\text{P-O-P})$, Q ¹
						1039		$\nu_s(\text{PO}_3^{2-})$, Q ¹	1006– 1048		$\nu_s(\text{PO}_3^{2-})$, Q ¹
			1018		1032			$\nu_{as}(\text{P-O-P})$ with $\nu_s(\text{O-P-O})$, Q ²		850– 1055	$\nu_{as}(\text{P-O-P})$, Q ²
	1099		1125		1108			$\nu_s(\text{PO}_2^-)$ and $\nu_{as}(\text{P-O-P})$ with $\nu_s(\text{O-P-O})$, Q ²	Not reported	Not reported	Not reported
						1133	1142	$\nu_{as}(\text{PO}_3^{2-})$, Q ¹	1090– 1107	1070– 1145	$\nu_{as}(\text{PO}_3^{2-})$, Q ¹
1184	1148 1174	1165	1165	1176	1169			$\nu_s(\text{PO}_2^-)$, Q ²	1134– 1245	1134– 1245	$\nu_s(\text{PO}_2^-)$, Q ²
1273 1321	1284	1289	1292	1293 1335	1293 1319			$\nu_{as}(\text{PO}_2^-)$, Q ²	1167– 1286	1194– 1293	$\nu_{as}(\text{PO}_2^-)$, Q ²

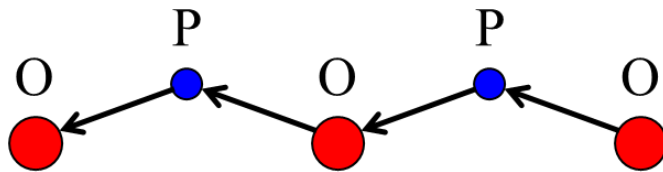
$v_s(\text{P-O-P})$ with $v_s(\text{O-P-O})$



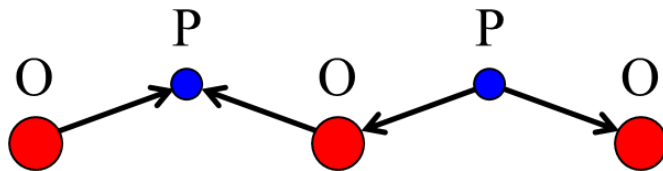
$v_s(\text{P-O-P})$ with $v_{as}(\text{O-P-O})$



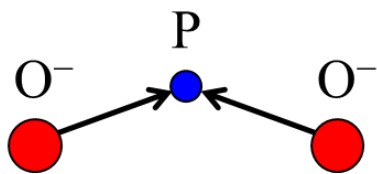
$v_{as}(\text{P-O-P})$ with $v_{as}(\text{O-P-O})$



$v_{as}(\text{P-O-P})$ with $v_s(\text{O-P-O})$



$v_s(\text{PO}_2^-)$



$v_{as}(\text{PO}_2^-)$

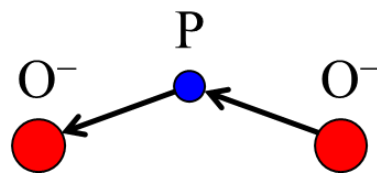


Fig. 2.10 Schematic illustrations of stretching vibrations of Q^2 units.

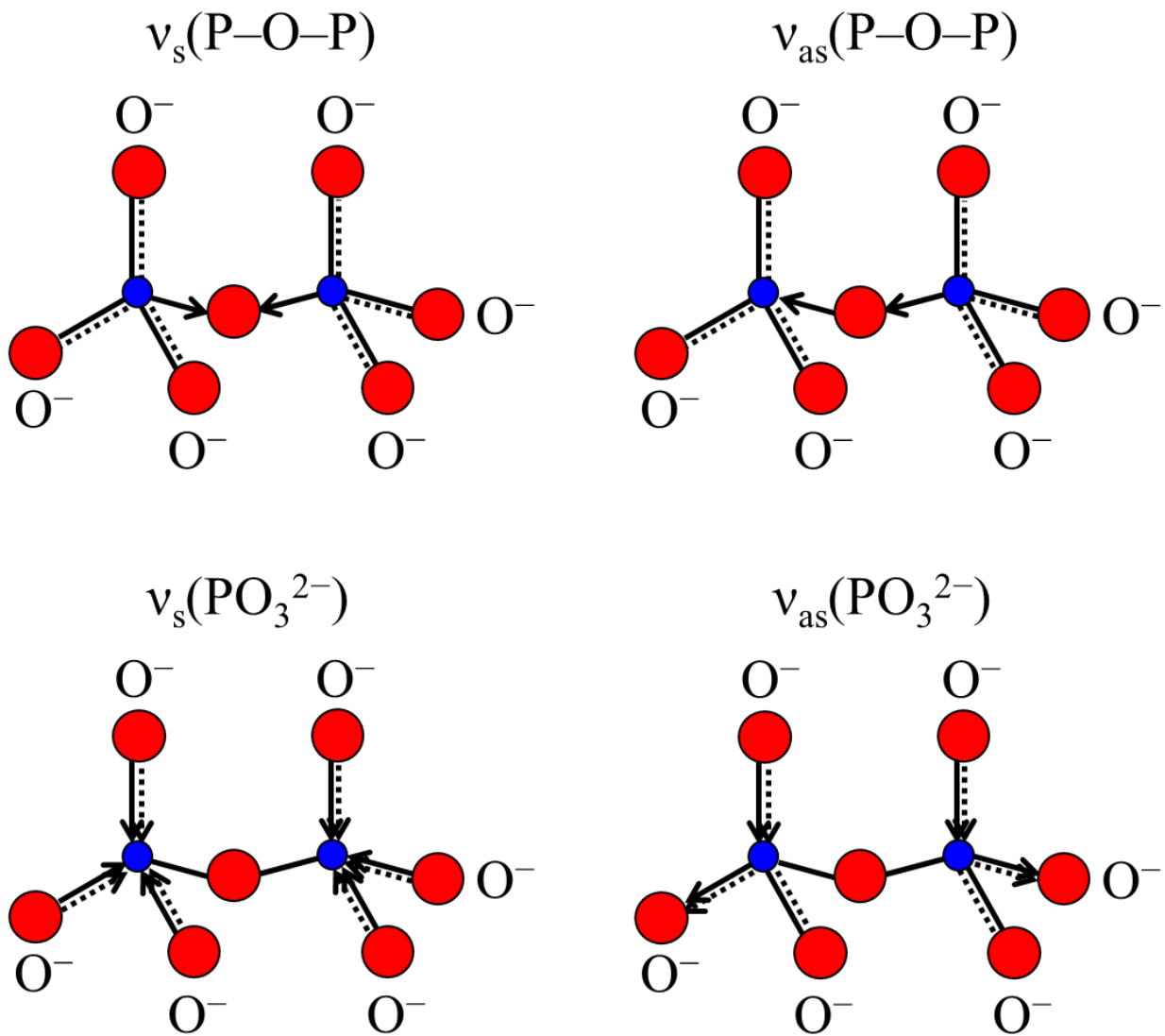


Fig. 2.11 Schematic illustrations of stretching vibrations Q^1 units.

2.3.6 Structural features of mixed alkali metaphosphate glass

Table 2.5 summarizes values related to glass structure for LiPO_3 , NaPO_3 , $(\text{Li,Na})\text{PO}_3$, and $(\text{Li,Na,K})\text{PO}_3$ glasses. Although the birefringence of $(\text{Li,Na,K})\text{PO}_3$ glass is much larger than that of NaPO_3 glass, only T_g and Δ_{PW} notably differ between NaPO_3 and $(\text{Li,Na,K})\text{PO}_3$ glasses. According to Gibbs-DiMarzio theory, T_g of alkali metaphosphate glasses decreases with decreasing intermolecular force between chains, which is associated with average F_{M-O} , and/or increasing flexibility of chains [26]. The flexibility of chain for $(\text{Li,Na,K})\text{PO}_3$ glass is higher than that for NaPO_3 glass because (A) T_g of $(\text{Li,Na,K})\text{PO}_3$ glass (222°C) is lower than that of NaPO_3 glass (292°C) and (B) average F_{M-O} of $(\text{Li,Na,K})\text{PO}_3$ glass is equivalent to that of NaPO_3 glass. It has been reported that higher flexibility of chains for $(\text{Li,Na})\text{PO}_3$ glass compared to NaPO_3 glass is caused by weakening of Na–O bonds in Li–NBO–Na pairs due to the greater field strength of Li^+ ions (**Fig. 2.12**) [2], hence the higher flexibility of chains in $(\text{Li,Na,K})\text{PO}_3$ glass compared to NaPO_3 glass can result from weakening of Na–O bonds in Li–NBO–Na pairs and K–O bonds in Li–NBO–K pairs.

From the above discussion, notable structural differences between $(\text{Li,Na,K})\text{PO}_3$ and NaPO_3 glasses are chain flexibility and distribution of F_{M-O} . The effect of chain flexibility and distribution of F_{M-O} on the development of anisotropy is considered below. **Fig. 2.13 and 2.14**, respectively, show schematic illustrations of chain structures for NaPO_3 and $(\text{Li,Na,K})\text{PO}_3$ glasses before and after application of uniaxial tensile stress above T_g . In the case of NaPO_3 glass under uniaxial tensile stress above T_g , chain orientation is small because of the low flexibility of chains and shear flow between chains due to the small distribution of F_{M-O} . In the case of $(\text{Li,Na,K})\text{PO}_3$ glass above T_g , PO_4 units with high F_{M-O} which act as pseudo-cross-linked structures suppress shear flow between chains during application of uniaxial tensile stress because the distribution of F_{M-O} for $(\text{Li,Na,K})\text{PO}_3$ glass is large. In addition, highly flexible chains composed of connected PO_4 units with low F_{M-O} for $(\text{Li,Na,K})\text{PO}_3$ glass are easily oriented by uniaxial tensile stress above T_g . The pseudo-cross-linked structures and high flexibility of chains, therefore, result in remarkable chain orientation of $(\text{Li,Na,K})\text{PO}_3$ glass under uniaxial tensile stress above T_g .

Chain flexibility for $(\text{Li,Na})\text{PO}_3$ glass is higher than that for NaPO_3 glass as mentioned above [2]. In addition, PO_4 units with high F_{M-O} which act as pseudo-cross-linked structures suppress shear flow between chains in $(\text{Li,Na})\text{PO}_3$ glass during application of uniaxial tensile stress as with $(\text{Li,Na,K})\text{PO}_3$ glass. The higher flexibility of chain and the pseudo-cross-linked structures, therefore, result in higher chain orientation of $(\text{Li,Na})\text{PO}_3$ glass compared to NaPO_3 glass when applying uniaxial tensile stress above T_g .

Metaphosphates are composed of not only chains, but also P_3O_9 , P_4O_{12} , P_6O_{18} , and P_8O_{24} rings [3]. As with rings in silica glass [28] and silica nanotube [29], the surface of rings in alkali metaphosphate glasses may tend to orient and/or deform parallel to stress direction during applying uniaxial tensile stress above T_g . Hence rings in alkali metaphosphate glasses may contribute to the development of anisotropy. The flexibility of rings in silica nanotube increases with increasing members of rings [29]. The deformation of rings in alkali metaphosphate glasses may be much smaller than that of chains because the deformation behavior of chains may be similar to that of infinite huge rings. The contribution of rings to the development anisotropy, therefore, may be much smaller than that of chains.

Table 2.5 Birefringence, T_g , average force constant between alkali cation and oxygen (F_{M-O}), the difference of peak wavenumbers between a peak originated from Li–O motion and a peak observed below 300 cm^{-1} (Δ_{PW}), the relative fraction of Q^2 units, and relative fraction of Q^2 units in chains to total Q^2 units (A_R) for LiPO_3 , NaPO_3 , $(\text{Li,Na})\text{PO}_3$, and $(\text{Li,Na,K})\text{PO}_3$ metaphosphate glasses.

		LiPO_3	NaPO_3	$(\text{Li,Na})\text{PO}_3$	$(\text{Li,Na,K})\text{PO}_3$
Birefringence (nm/mm)	Glass fiber elongated at tensile stress of 40MPa above T_g	39 ^a	233 ^a	519 ^a	1679 ^a
T_g (°C)		334	292	251	222
Average F_{M-O} (N/cm)		0.269 ^b	0.177 ^b	0.223 ^b	0.186 ^b
Δ_{PW} (cm^{-1})	Absorption coefficient spectra in the range $100\text{--}600\text{ cm}^{-1}$	0	0	192	210
Relative fraction of Q^2 units (%)	^{31}P MAS NMR Spectra	96.6	100 (no detectable Q^1 peak)	97.3	98.7
A_R (%)	Raman spectra in the range $600\text{--}850\text{ cm}^{-1}$	21	36	28	36
A_R (%)	Raman spectra in the range $1050\text{--}1250\text{ cm}^{-1}$	37	48	42	48
A_R (%)	Absorption coefficient spectra in the range $800\text{--}1400\text{ cm}^{-1}$	13	28	20	27

^aBirefringence are values reported in the literature [2].

^b F_{M-O} for $(\text{Li,Na})\text{PO}_3$ and $(\text{Li,Na,K})\text{PO}_3$ glasses was calculated by using F_{M-O} values for LiPO_3 (0.269 N/cm), NaPO_3 (0.177 N/cm), and KPO_3 (0.112 N/cm) metaphosphate glasses reported in the literature [21].

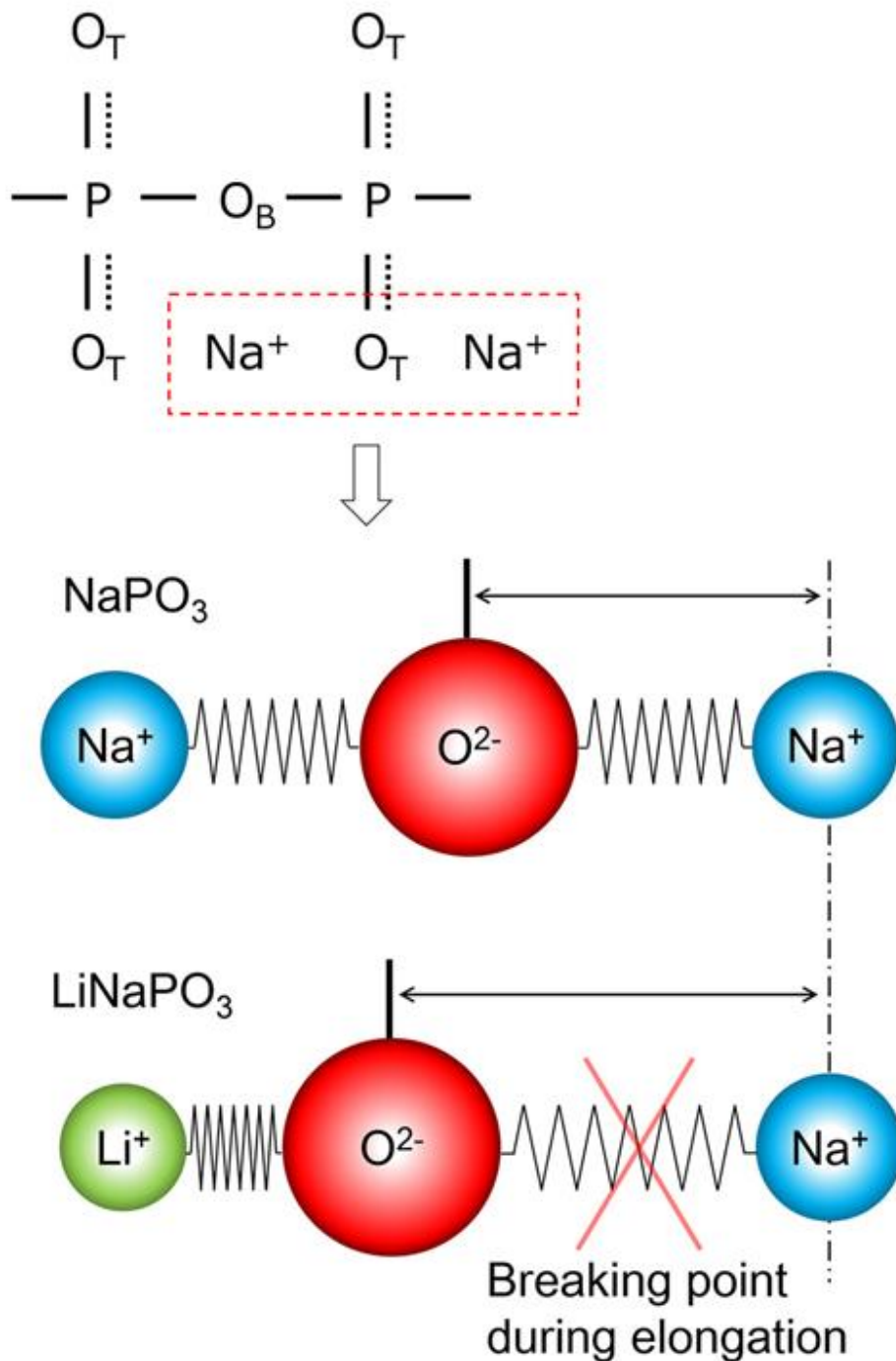


Fig. 2.12 Schematic description of mixed alkali effect in lithium sodium metaphosphate glass based on Dietzel's model [27]. The $Na^+ \dots O_T \dots Na^+$ distance changes by replacing one Na^+ with Li^+ , which leads to the induction of a breakable weaker bond during elongation. Reproduced with permission from Ref. [2]. Copyright 2020, The American Ceramic Society.

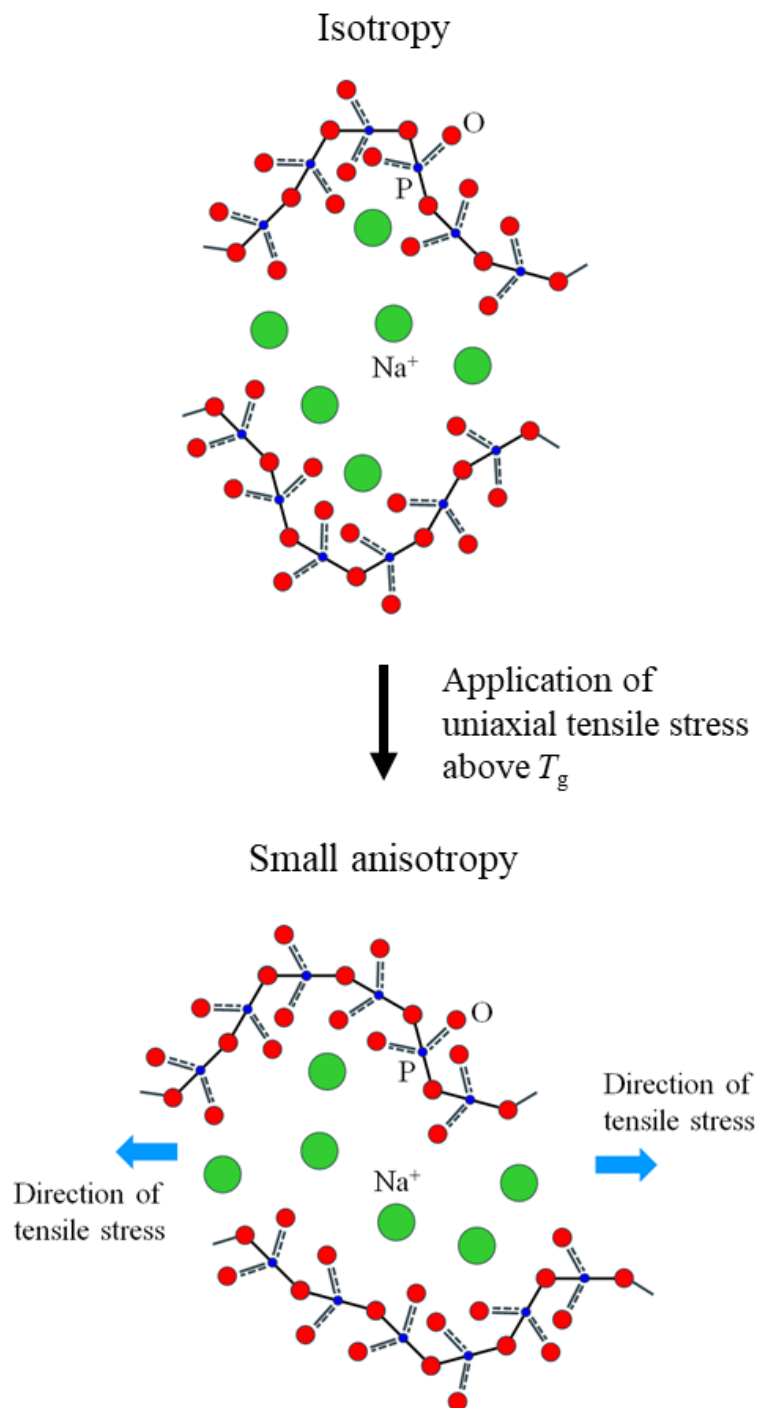


Fig. 2.13 Schematic illustration of chain structures for NaPO_3 glass. Small deep blue, middle-sized red, and large green represent phosphorus, oxygen, and sodium cation, respectively.

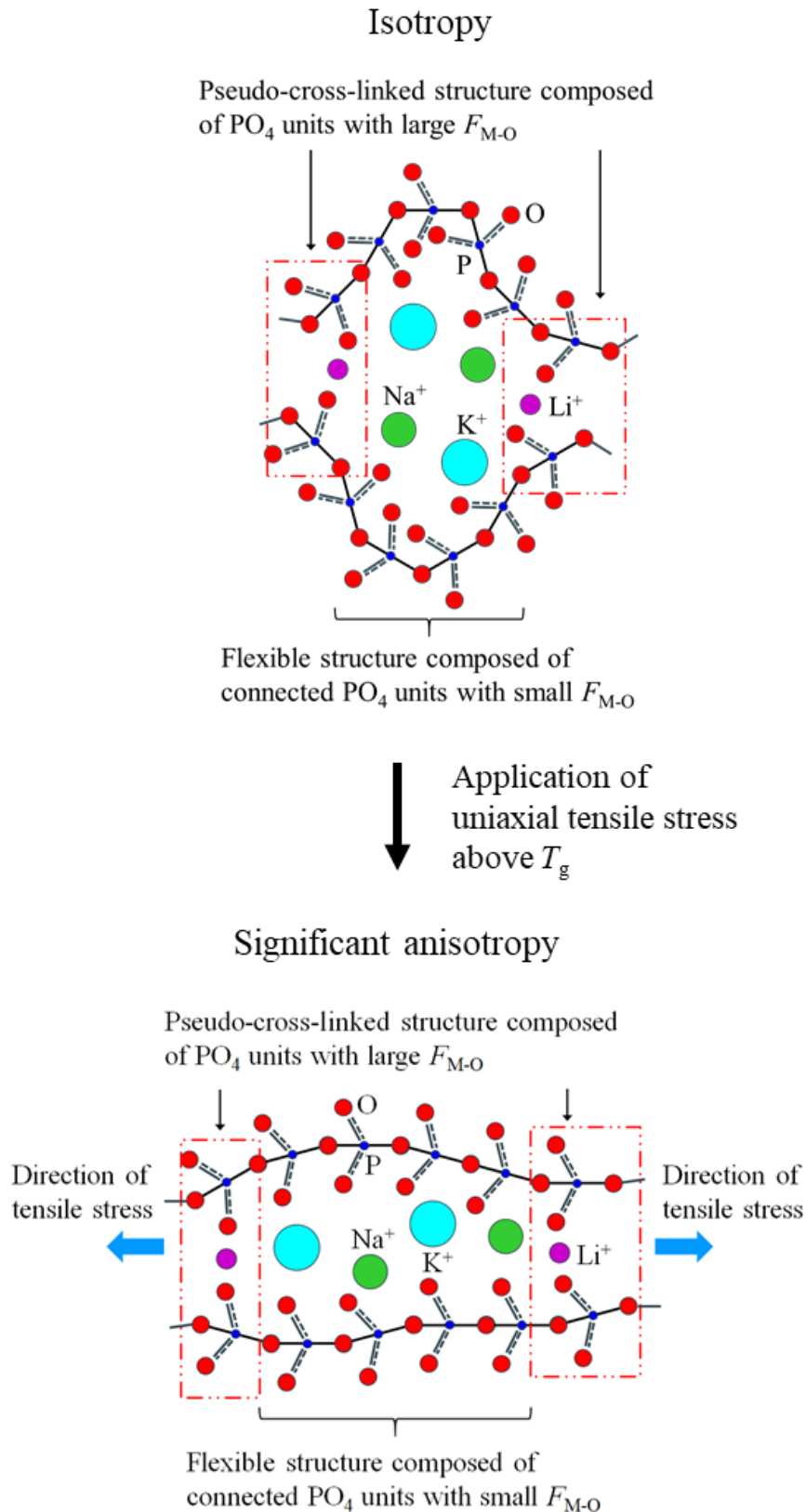


Fig. 2.14 Schematic illustration of chain structures for $(\text{Li,Na,K})\text{PO}_3$ glasses. Small deep blue, middle-sized red, middle-sized purple, large green, and large light blue circles represent phosphorus, oxygen, lithium cation, sodium cation, and potassium cation, respectively.

2.4 Conclusions

(Li,Na,K)PO₃ glass applied uniaxial tensile stress above T_g has remarkably oriented chain structures. Structural features causing the formation of the significant anisotropic structure in (Li,Na,K)PO₃ glass were investigated by analyzing ³¹P MAS NMR, Raman, and FTIR spectra. We also investigated vibration modes of alkali metaphosphate and pyrophosphate crystals by DFT calculations of Raman and IR spectra to verify the interpretation of peak assignments reported in previous studies.

The assignments of peaks of the calculated Raman and IR spectra were consistent with reported assignments of phosphate crystals and glasses except for the assignment of the peaks around 1100 cm⁻¹ of the calculated IR spectra for the alkali metaphosphate crystals. The calculated IR spectra showed that the peaks around 1100 cm⁻¹ result from not only asymmetric stretching vibrations of P–NBO bonds of Q¹ units but also symmetric stretching vibrations of P–NBO bonds and asymmetric stretching vibrations of –P–O–P– bonds of Q² units.

The analysis of ³¹P MAS NMR, Raman, and FTIR spectra showed that (A) the number of Q² units in chains for NaPO₃ and (Li,Na,K)PO₃ glasses is equivalent because the number of Q² units and A_R for NaPO₃ and (Li,Na,K)PO₃ glasses are comparable, and (B) an increase in the number of types of alkali cations for alkali metaphosphate glasses results in larger distribution of F_{M-O} . According to Gibbs-DiMarzio theory, T_g of alkali metaphosphate glasses decreases with decreasing intermolecular force between chains and/or increasing flexibility of chains. The flexibility of chain for (Li,Na,K)PO₃ glass is higher than that for NaPO₃ glass because T_g of (Li,Na,K)PO₃ glass is lower than that of NaPO₃ glass and F_{M-O} of (Li,Na,K)PO₃ glass is equivalent to that of NaPO₃ glass. Formation of the significant anisotropic structure of (Li,Na,K)PO₃ glass under uniaxial tensile stress above T_g , therefore, results from orientation of highly flexible local structures with small F_{M-O} during the suppression of shear flow between chains by local structures with large F_{M-O} . The results support the adequacy of the model of the orientation of chains under uniaxial tensile stress above T_g proposed by Inaba et al.

References

1. S. Inaba, H. Hosono, and S. Ito, Entropic shrinkage of an oxide glass, *Nat. Mater.* **14** 312–317 (2015).
2. S. Inaba, Y. Benino, S. Kohara, H. Hosono, and S. Ito, Anisotropic structure of alkali metaphosphate glasses, *J. Am. Ceram. Soc.* **103** 3631–3641 (2020).
3. A. Rulmont, R. Cahay, M. Liegeois-Duyckaerets, and P. Tarte, Vibrational spectroscopy of phosphates: some general correlations between structure and spectra, *Eur. J. Solid State Inorg. Chem.* **28** 207–219 (1991).
4. E. I. Kamitsos, J. A. Kapoutsis, G. D. Chryssikos, J. M. Hutchinson, A. J. Pappin, M. D. Ingram, and J. A. Duffy, Infrared study of AgI containing superionic glasses, *Phys. Chem. Glasses* **36** 141–149 (1995).
5. K. Yamamoto and H. Ishida, Optical theory applied to infrared spectroscopy, *Vib. Spectrosc.* **8** 1–36 (1994).
6. P. Giannozzi, S. Baroni, N. Bonini, M. Calandra, R. Car, C. Cavazzoni, D. Ceresoli, G. L. Chiarotti, M. Cococcioni, and I. Dabo, QUANTUM ESPRESSO: a modular and open-source software project for quantum simulations of materials, *J. Phys.: Condens. Matter* **21** 395502 (2009).
7. P. Giannozzi, O. Andreussi, T. Brumme, O. Bunau, M. B. Nardelli, M. Calandra, R. Car, C. Cavazzoni, D. Ceresoli, M. Cococcioni, N. Colonna, I. Carnimeo, A. D. Corso, S. de Gironcoli, P. Delugas, R. A. DiStasio Jr., A. Ferretti, A. Floris, G. Fratesi, G. Fugallo, R. Gebauer, U. Gerstmann, F. Giustino, T. Gorni, J. Jia, M. Kawamura, H.-Y. Ko, A. Kokalj, E. Küçükbenli, M. Lazzeri, M. Marsili, N. Marzari, F. Mauri, N. L. Nguyen, H.-V. Nguyen, A. Otero-de-la-Roza, L. Paulatto, S. Poncé, D. Rocca, R. Sabatini, B. Santra, M. Schlipf, A. P. Seitsonen, A. Smogunov, I. Timrov, T. Thonhauser, P. Umari, N. Vast, X. Wu, and S. Baroni, Advanced capabilities for materials modelling with Quantum ESPRESSO, *J. Phys.: Condens. Matter* **29** 465901 (2017).
8. L. He, F. Liu, G. Hautier, M. J. T. Oliveira, M. A. L. Marques, F. D. Vila, J. J. Rehr, G.-M. Rignanese, and A. Zhou, Accuracy of generalized gradient approximation functionals for density-functional perturbation theory calculations, *Phys. Rev. B* **89** 064305 (2014).
9. J. C. Guitel and I. Tordjman, Structure cristalline de polyphosphate de lithium LiPO_3 , *Acta Crystallogr. B* **32** 2960–2966 (1976).
10. D. E. C. Corbridge, Crystallographic data on some Kurrol salts, *Acta Crystallogr.* **8** 520 (1955).
11. K. Y. Leung and C. Calvo, The Structure of $\text{Na}_4\text{P}_2\text{O}_7$ at 22 °C, *Can. J. Chem.* **50** 2519–2526 (1972).
12. K. Momma and F. Izumi, VESTA 3 for three-dimensional visualization of crystal, volumetric and morphology data, *J. Appl. Crystallogr.* **44** 1272–1276 (2011).
13. R. K. Brow, R. J. Kirkpatrick, and G. L. Turner, The short range structure of sodium phosphate glasses I. MAS NMR studies, *J. Non-Cryst. Solids* **116** 39–45 (1990).
14. L. V. Wüllen, H. Eckert, and G. Schwering, Structure-property correlations in lithium phosphate glasses: new insights from $^{31}\text{P} \leftrightarrow ^7\text{Li}$ double-resonance NMR, *Chem. Mater.* **12** 1840–1846 (2000).
15. B. N. Nelson and G. J. Exarhos, Vibrational spectroscopy of cation-site interactions in phosphate glasses, *J. Chem. Phys.* **71** 2739–2747 (1979).
16. A. Mandal, V. K. Gogi, C. Mohanty, R. Chbeir, and P. Boolchand, Emerging role of local and extended

- range molecular structures on functionalities of topological phases of $(\text{Na}_2\text{O})_x(\text{P}_2\text{O}_5)_{100-x}$ glasses using Raman scattering and modulated DSC, *Int. J. Appl. Glass Sci.* **12** 89–110 (2021).
17. R. K. Brow, D. R. Tallant, S. T. Myers, and C. C. Phifer, The short-range structure of zinc polyphosphate glass, *J. Non-Cryst. Solids* **191** 45–55 (1995).
 18. R. K. Brow, Review: the structure of simple phosphate glasses, *J. Non-Cryst. Solids* **263&264** 1–28 (2000).
 19. K. Griebenow, E. I. Kamitsos, and L. Wondraczek, Mixed-modifier effect in (Ca,Mg) metaphosphate glasses, *J. Non-Cryst. Solids* **468** 74–81 (2017).
 20. I. Konidakis, C. P. E. Varsamis, E. I. Kamitsos, D. Möncke, and D. Ehrt, Structure and properties of mixed strontium-manganese metaphosphate glasses, *J. Phys. Chem. C* **114** 9125–9138 (2010).
 21. G. J. Exarhos, P. J. Miller, and W. M. Risen Jr., Interionic vibrations and glass transitions in ionic oxide metaphosphate glasses, *J. Chem. Phys.* **60** 4145–4155 (1974).
 22. K. Griebenow, U. Hoppe, D. Möncke, E. I. Kamitsos, and L. Wondraczek, Transition-metal incorporation and Co-Sr/Mn-Sr mixed-modifier effect in metaphosphate glasses, *J. Non-Cryst. Solids* **460** 136–145 (2017).
 23. L. L. Velli, C. P. E. Varsamis, E. I. Kamitsos, D. Möncke, and D. Ehrt, Structural investigation of metaphosphate glasses, *Phys. Chem. Glasses* **46** 178–181 (2005).
 24. K. Griebenow, C. B. Bragatto, E. I. Kamitsos, and L. Wondraczek, Mixed-modifier effect in alkaline earth metaphosphate glasses, *J. Non-Cryst. Solids* **481** 447–456 (2018).
 25. G. L. Saoût, P. Simon, F. Fayon, A. Blin, and Y. Vaills, Raman and infrared study of $(\text{PbO})_x(\text{P}_2\text{O}_5)_{(1-x)}$ glasses, *J. Raman Spectrosc.* **33** 740–746 (2002).
 26. A. Eisenberg and S. Saito, Possible experimental equivalence of the Gibbs-DiMarzio and free-volume theories of the glass transition, *J. Chem. Phys.* **45** 1673–1678 (1966).
 27. A. H. Dietzel, On the so-called mixed alkali effect, *Phys. Chem. Glasses* **24** 172–180 (1983).
 28. X. Bidault, S. Chaussedent, W. Blanc, and D. R. Neuville, Deformation of silica glass studied by molecular dynamics: Structural origin of the anisotropy and non-Newtonian behavior, *J. Non-Cryst. Solids* **433** 38–44 (2016).
 29. K. Muralidharan, J. Torras, and S. B. Trickey, Energetics and mechanical properties of silica nanotubes, *J. Phys. Condens. Matter.* **19** 386238 (2007).

Chapter 3: Relaxation of anisotropic alkali metaphosphate glass

3.1 Introduction

Anisotropic 12.5Li₂O–12.5Na₂O–12.5K₂O–12.5Cs₂O–50P₂O₅ (mol%, (Li,Na,K,Cs)PO₃) metaphosphate glass prepared by elongation above the glass transition temperature (T_g) and rapid cooling from above T_g to room temperature shows huge shrinkage when the anisotropic glass is heated above T_g [1]. The huge shrinkage results from relaxation of oriented –P–O–P– chains to disordered –P–O–P– chains due to entropic elasticity because endotherm is observed during the huge shrinkage [1]. As a mechanism for the huge shrinkage of anisotropic (Li,Na,K,Cs)PO₃ glass, Inaba et al. proposed a model that relaxation of local structures with small force constant between alkali cation and oxygen (F_{M-O}) adjacent to Na⁺, K⁺, and Cs⁺ cations in oriented –P–O–P– chains occur during the suppression of shear flow between chains by local structures with large F_{M-O} adjacent to Li⁺ cations which act as pseudo-cross-linked structures [1]. However, there is not enough evidence of the relaxation of the local structures with small F_{M-O} under coexistence with the local structures with large F_{M-O} which act as pseudo-cross-linked structures above T_g . In addition, the relaxation mechanism of anisotropic (Li,Na,K,Cs)PO₃ glass below T_g is still unknown. In this chapter, the relaxation mechanism of anisotropic (Li,Na,K,Cs)PO₃ glass in the range from room temperature to above T_g was investigated.

3.2 Experimental procedure

The (Li,Na,K,Cs)PO₃ metaphosphate glass was prepared by melting a mixture of 50Li₂O–50P₂O₅, 50Na₂O–50P₂O₅, 50K₂O–50P₂O₅ (mol%) (>99.7%, Rasa Industries), Cs₂CO₃ (>95%, FUJIFILM Wako Pure Chemical Corporation), and NH₄H₂PO₄ (>99%, FUJIFILM Wako Pure Chemical Corporation) in a 95%Pt–5%Au crucible at 1000 °C for 1 h. An isotropic (Li,Na,K,Cs)PO₃ glass fiber was prepared by quickly drawing up a silica rod inserted into the glass melt. To prepare an anisotropic (Li,Na,K,Cs)PO₃ glass fiber, the as-drawn isotropic glass fiber was elongated under an initial nominal tensile stress of 5 MPa at 230 °C for about 10 min and then cooled rapidly from 230 °C to room temperature.

Birefringence (Δn) of the fibers was determined from phase retardation measured with a polarization microscope using a quartz wedge and a de Sénarmont compensator. The birefringence is given by

$$\Delta n = \frac{\lambda \delta}{\pi d} \quad (3.1)$$

where d , δ , and λ are the fiber diameter, the phase retardation, and the light wavelength, respectively. The T_g of the fibers was measured by differential thermal analysis using a thermal analyzer (TG/DTA 6300, Seiko Instrument Inc.) at a heating rate of 10 °C min⁻¹. The T_g for the isotropic and anisotropic glasses was 209 and 207 °C, respectively.

When a sine wave strain ($\varepsilon = \varepsilon_0 \sin \omega t$) is applied to materials, the stresses of the elastic, viscoelastic, and viscous bodies, respectively, are expressed by the following equations:

$$\text{Elastic body} \quad \sigma = \sigma_0 \sin \omega t \quad (3.2)$$

$$\text{Viscoelastic body} \quad \sigma = \sigma_0 \sin(\omega t + \delta) \quad (0 < \delta < \frac{\pi}{2}) \quad (3.3)$$

$$\text{Viscous body} \quad \sigma = \sigma_0 \sin(\omega t + \frac{\pi}{2}) \quad (3.4)$$

where $\omega = 2\pi f$ and f is the frequency of periodic strain.

The phase difference between a strain and stress of the elastic, viscoelastic, and viscous bodies, respectively, are 0, δ ($0 < \delta < \pi/2$), and $\pi/2$ radian. **Figure 3.1** shows the relationship between a sine wave strain and stress of the elastic, viscoelastic, and viscous bodies.

Equation (3.3) can be converted to the following equation.

$$\sigma = \left(\frac{\sigma_0}{\varepsilon_0} \cos \delta\right) \varepsilon_0 \sin \omega t + \left(\frac{\sigma_0}{\varepsilon_0} \sin \delta\right) \varepsilon_0 \sin\left(\omega t + \frac{\pi}{2}\right) \quad (3.5)$$

Storage modulus (E'), loss modulus (E''), and loss factor ($\tan \delta$), respectively, are defined as the following equations:

$$E' = \frac{\sigma_0}{\varepsilon_0} \cos \delta \quad (3.6)$$

$$E'' = \frac{\sigma_0}{\varepsilon_0} \sin \delta \quad (3.7)$$

$$\tan \delta = \frac{\sin \delta}{\cos \delta} = \frac{E''}{E'} \quad (3.8)$$

The temperature dependence of storage moduli (E') and loss factors ($\tan \delta$) were evaluated by dynamic mechanical analysis (DMA) using a dynamic viscoelastic analyzer (DVA-200, IT Keisoku Seigyo, Japan) at 10 Hz with a longitudinal dynamic tensile strain of 0.01%. Glass fibers with a diameter of 300–340 μm and length of 1.3 mm were heated from room temperature to 250 $^{\circ}\text{C}$ at a rate of 5 $^{\circ}\text{C min}^{-1}$.

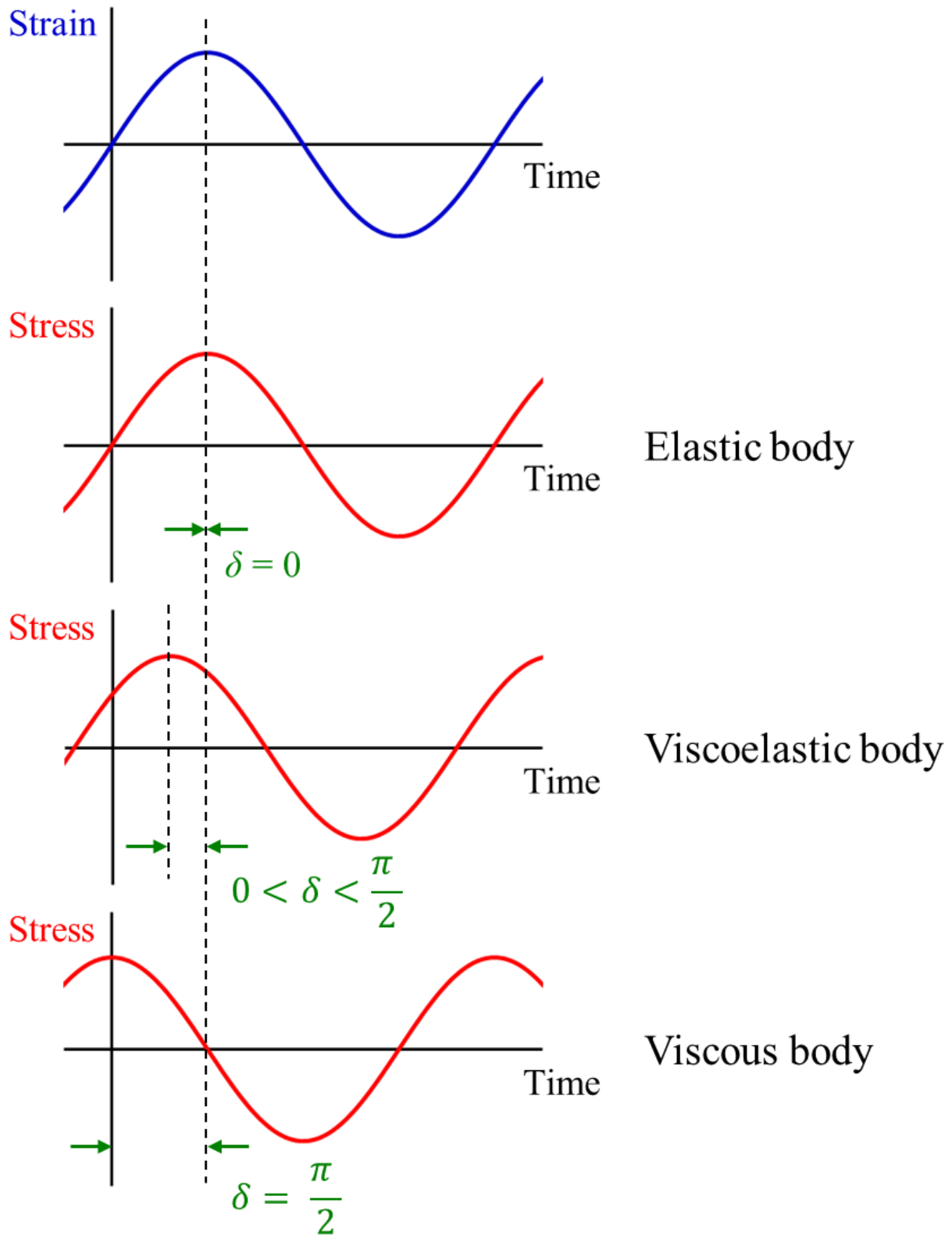


Fig. 3.1 Stress response and phase difference during application of a sine wave strain.

Temperature dependence of Raman spectra in the range from room temperature (25 °C) to 260 °C was evaluated by a micro Raman spectrometer (LabRAM HR, Horiba, Ltd., Japan) using a backscattering geometry. The wavelength of the excitation laser was 457 nm. The polarization direction of the excitation laser and length direction of the glass fibers was parallel as shown in Fig. 3.2.

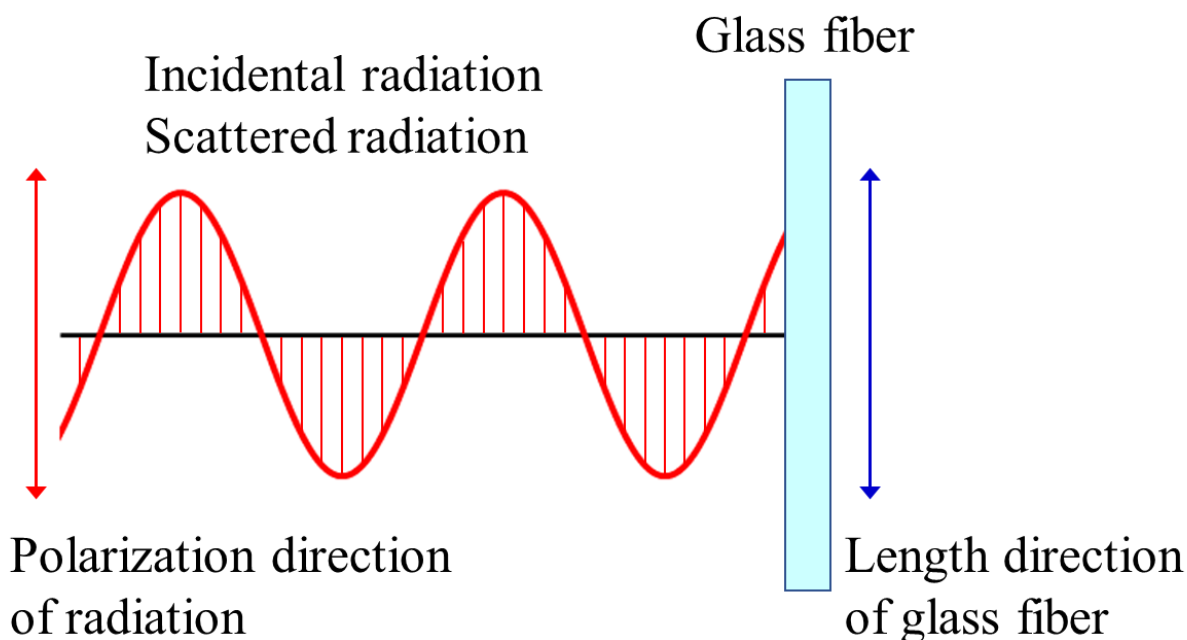


Fig. 3.2 Polarization direction of incident and scattered radiation and the length direction of glass fiber

3.3 Results and Discussion

Figure 3.3 shows the temperature dependence of E' and $\tan\delta$ for the anisotropic and isotropic glasses. The former has a Δn of $3200 \text{ nm}\cdot\text{mm}^{-1}$, which suggests partially oriented $-\text{P}-\text{O}-\text{P}-$ chains. Both glasses were confirmed not to crystallize below 270 °C using differential scanning calorimetry. Although both glasses showed nearly the same T_g and dynamic mechanical properties below 160 °C (Region 0), significant differences were observed in the range from 160 to 225 °C (Regions 1 and 2). The E' for the isotropic glass monotonically decreased with increasing temperature, whereas for the anisotropic glass it dropped quickly in the range from 160 °C to T_g (Region 1), and thereafter increased to the value of the isotropic glass in the range from T_g to 225 °C (Region 2). Such unusual E' behavior has not been observed in oxide glasses. The $\tan\delta$ for the isotropic glass monotonically increased with increasing temperature, whereas for the anisotropic glass it increased in the lower temperature range (Region 1) to a much larger value than that the isotropic glass, remained approximately constant throughout region 2, and tracked the increase of the isotropic glass above 225 °C (Region 3).

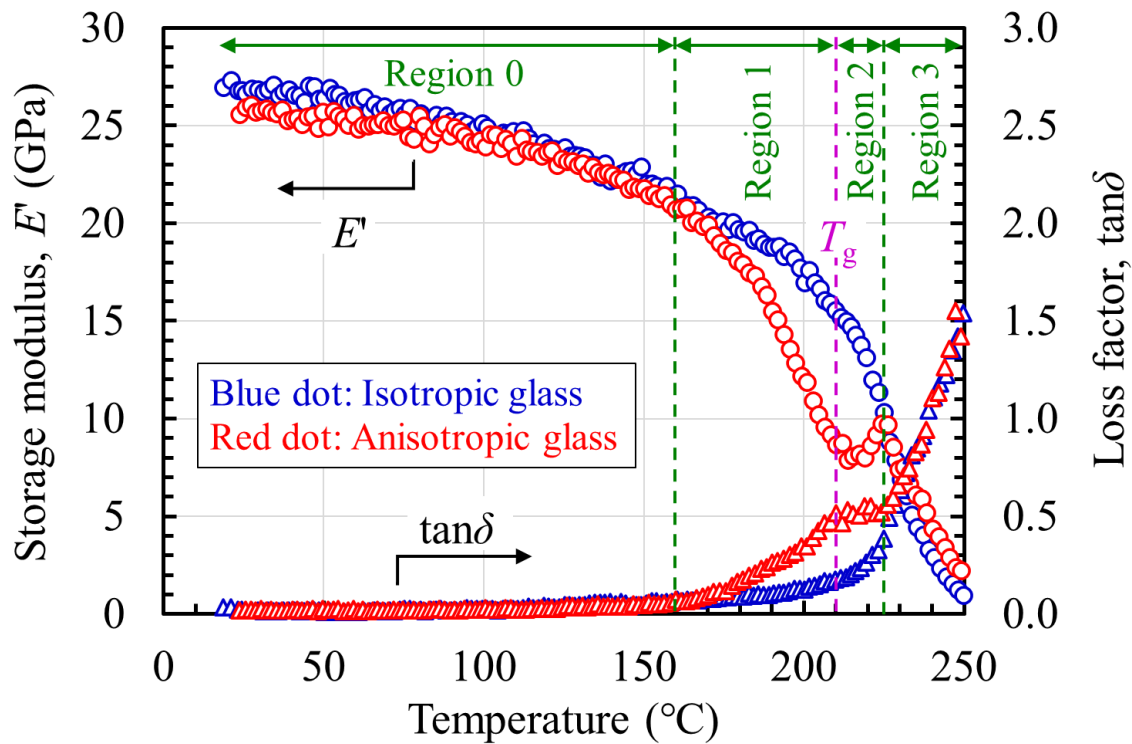


Fig. 3.3 Temperature dependence of storage moduli (E') and loss factors ($\tan\delta$) for isotropic and anisotropic (Li,Na,K,Cs)PO₃ glasses measured by DMA at 10 Hz.

To investigate the structural change related to the dynamic mechanical properties, the temperature dependence of Raman spectra was evaluated in the range from room temperature to 260 °C, shown in **Fig. 3.4 (a) and (b)**. The bands at 620–820 cm⁻¹ and 1070–1220 cm⁻¹ are assigned to symmetric stretching vibrations of in-chain –P–O–P– and out-of-chain O⁻–P–O⁻, respectively [2].

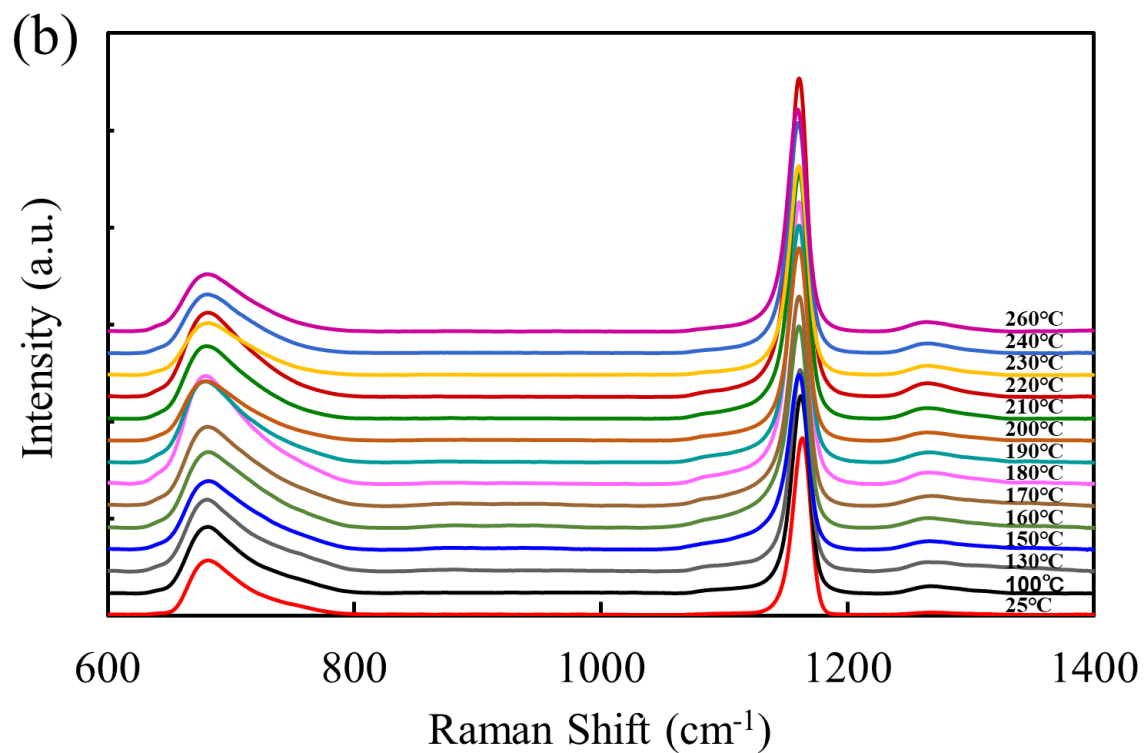
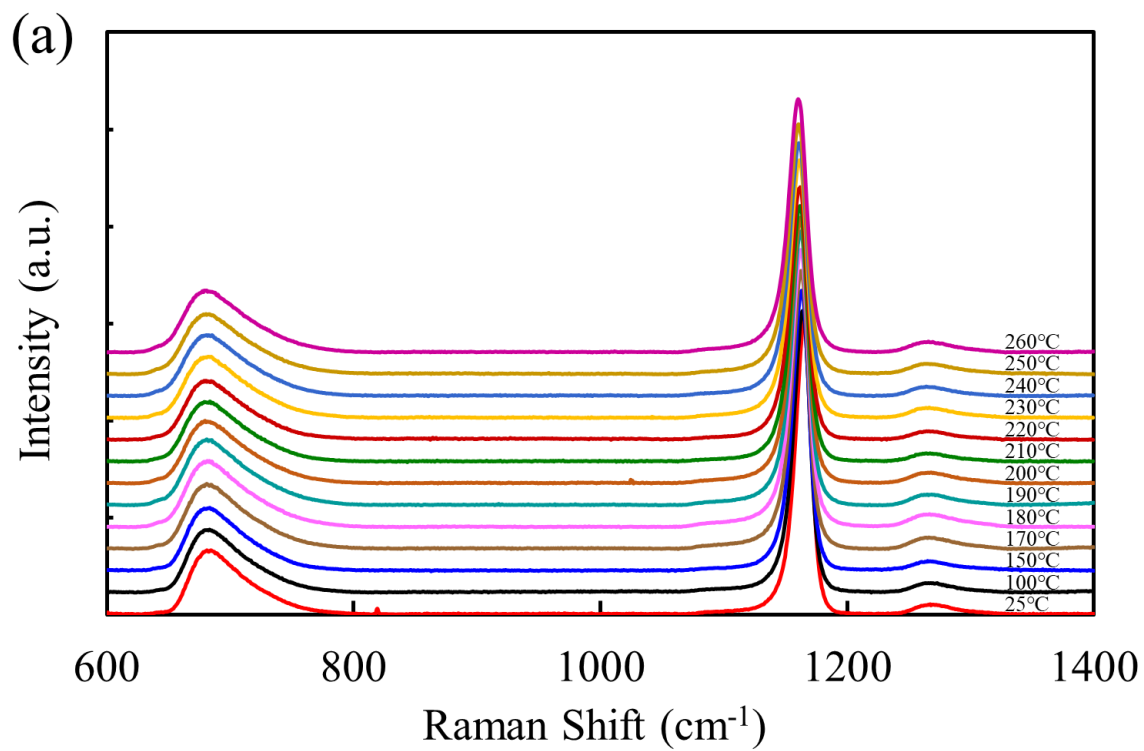


Fig. 3.4 Raman spectra for (a) isotropic and (b) anisotropic $(\text{Li,Na,K,Cs})\text{PO}_3$ glasses.

Figure 3.5 shows the temperature dependence of the peak position for the band between 1070–1220 cm^{-1} (ν_{max}). The ν_{max} for alkali metaphosphate glasses is known to depend on the force constant between alkali cation and oxygen ($F_{\text{M-O}}$) and the out-of-chain O^- -P-O $^-$ bond angle (ϕ) shown in **Fig. 3.6**. The value shifts toward lower wavenumber with decreasing $F_{\text{M-O}}$ and/or with increasing ϕ [3]. The $F_{\text{M-O}}$ for the anisotropic glass must be nearly equal to that for the isotropic glass at room temperature because both had nearly the same E' at room temperature. Since the ϕ for the alkali metaphosphate crystals with oriented -P-O-P- chain structures is larger than that for isotropic alkali metaphosphate glasses [3–5], the higher orientation of the chain may lead to larger ϕ ; i.e., the anisotropic glass has a larger ϕ . The lower ν_{max} for the anisotropic glass at room temperature likely resulted from the larger ϕ compared with the isotropic glass.

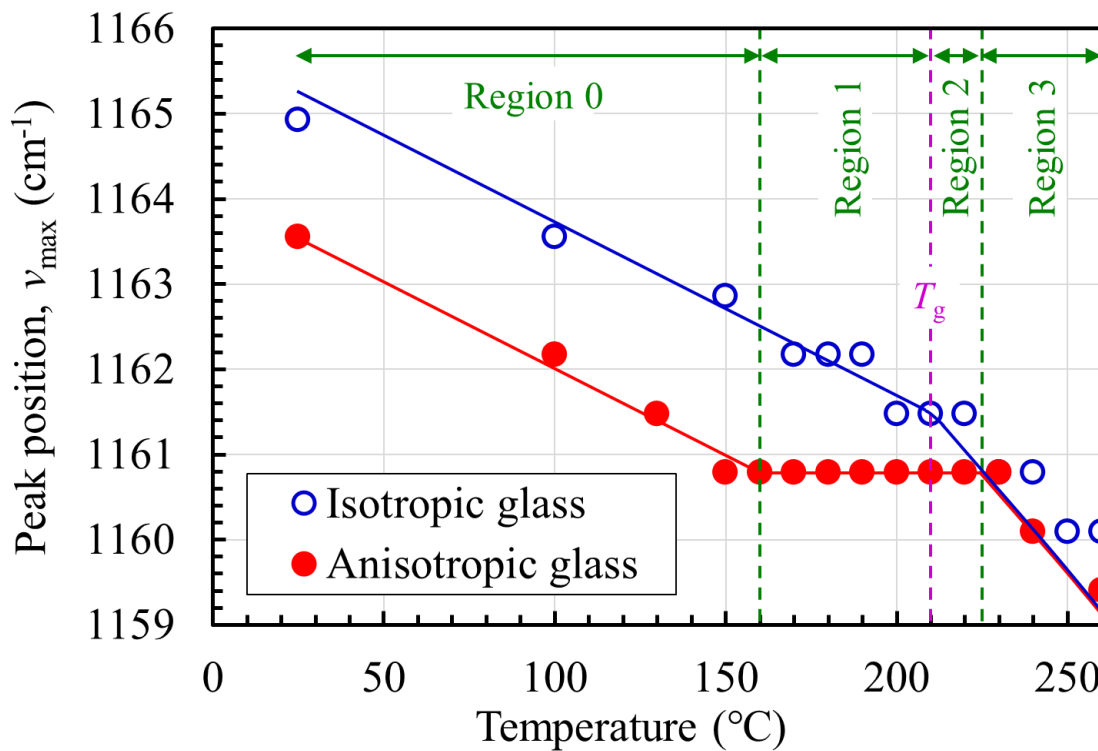


Fig. 3.5 Temperature dependence of peak position for a band between 1070–1220 cm^{-1} (ν_{max}) for isotropic and anisotropic glasses.

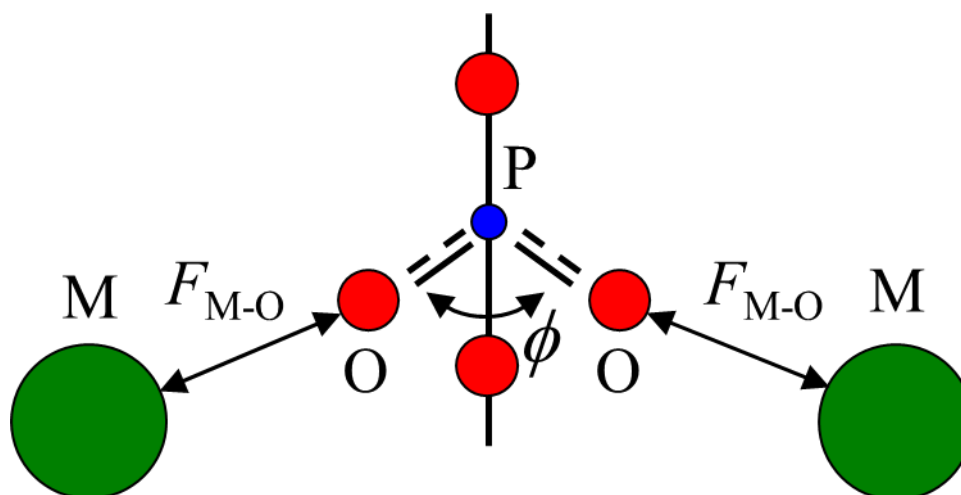


Fig. 3.6 Schematic illustration of the structure of alkali metaphosphate glass. Small (blue), middle-sized (red), and large (green) closed circles represent phosphorus, oxygen, and alkali cations, respectively.

Figure 3.7 shows the temperature dependence of peak intensity between $1100\text{--}1200\text{ cm}^{-1}$, normalized by peak intensity between $620\text{--}820\text{ cm}^{-1}$ (I_R) for both glasses. The larger number of --P--O--P-- chains oriented in the polarization direction of the excitation laser for the anisotropic glass resulted in smaller I_R at room temperature compared to the isotropic glass, as reported previously (**Fig. 3.8**) [1].

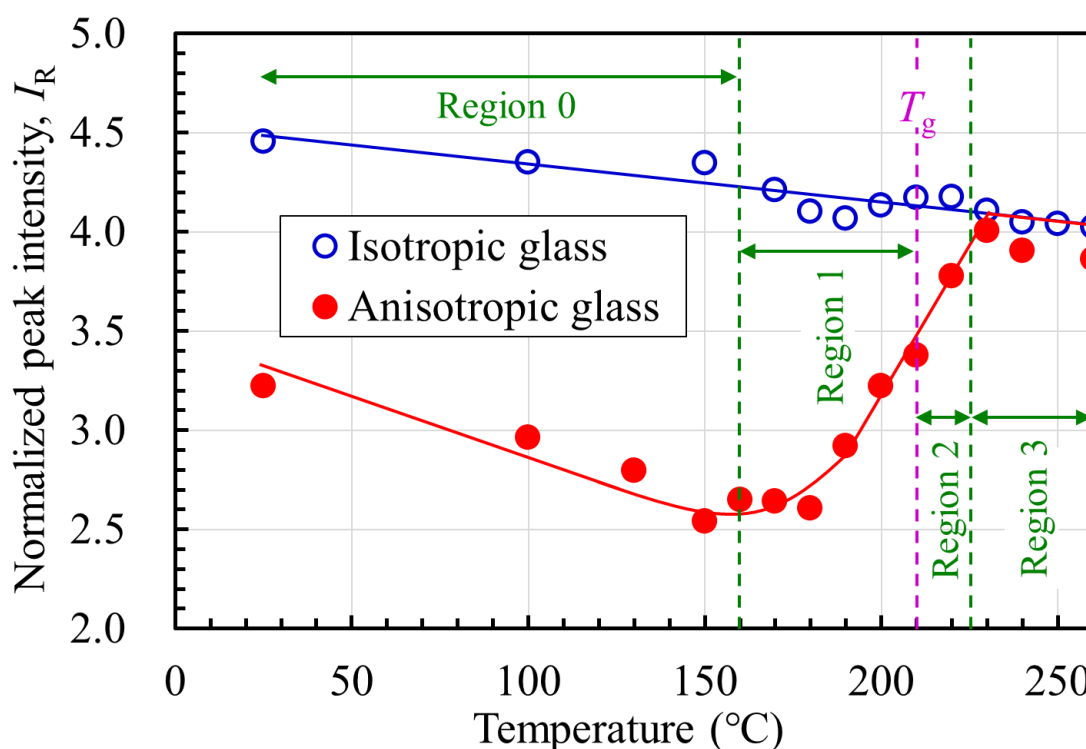


Fig. 3.7 Temperature dependence of peak intensity between $1100\text{--}1200\text{ cm}^{-1}$ normalized by peak intensity between $620\text{--}820\text{ cm}^{-1}$ (I_R) for both glasses.

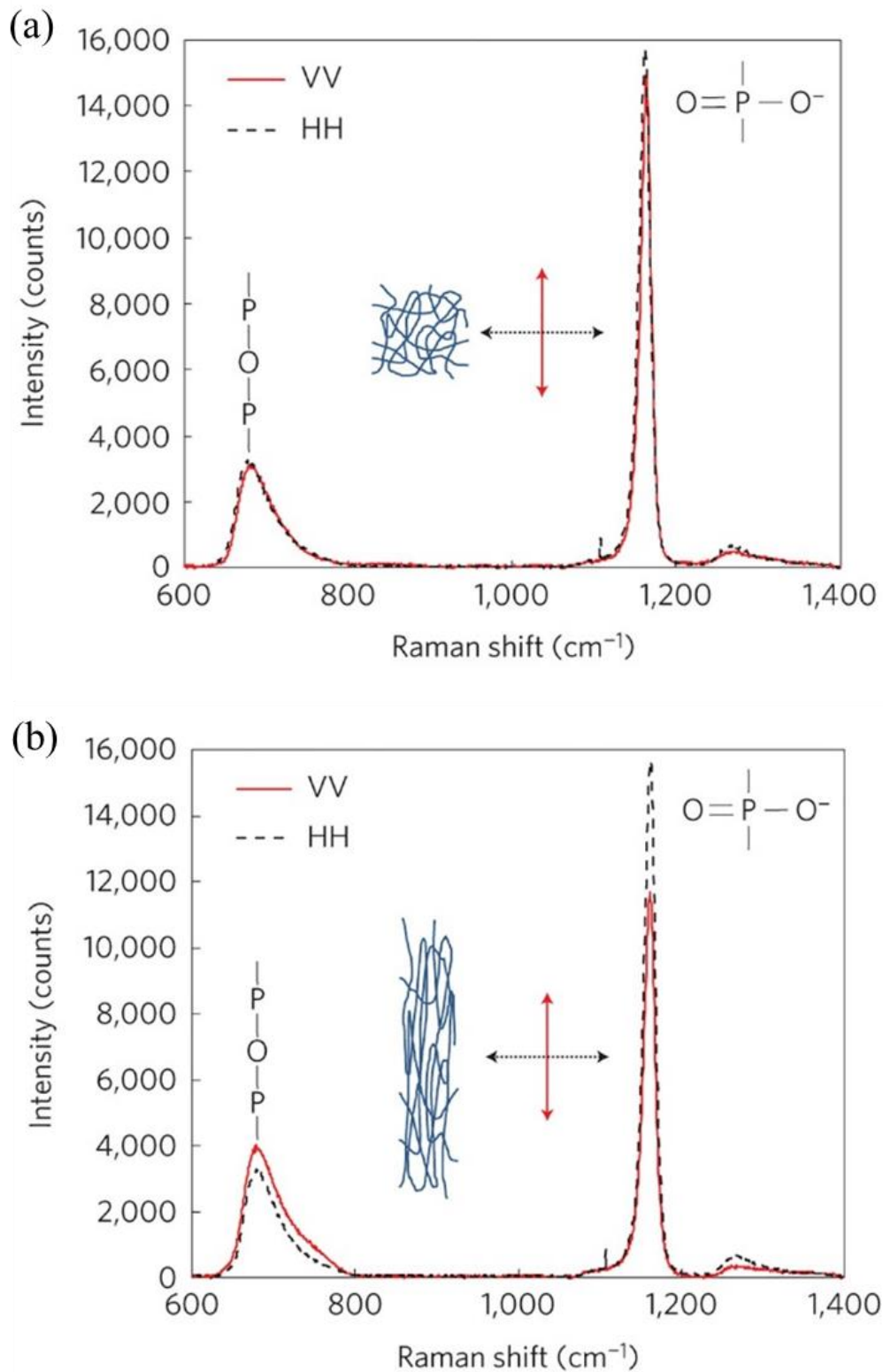


Fig. 3.8 Polarized Raman scattering parallel (VV) and perpendicular (HH) to the longitudinal axis of (a) isotropic (Li,Na,K,Cs)PO₃ fiber and (b) anisotropic (Li,Na,K,Cs)PO₃ fiber with birefringence of 0.0133 (= 13300 nm/mm), respectively. Reproduced with permission from Ref. [1]. Copyright 2014, Nature Publishing Group.

The monotonic decrease in the peak position ν_{\max} with increasing temperature in region 0 for both glasses (**Fig. 3.5**), and the constant difference of ν_{\max} between the two glasses, may be caused by a decrease in F_{M-O} and a constant ϕ for both glasses. Since the peak intensity I_R for alkali metaphosphate glasses is reported to decrease as the $P-O^-$ bond becomes more ionic [2], the decrease in I_R in region 0 is likely caused by increasing ionicity of the $P-O^-$ bond, with no coincident increase in the number of oriented $-P-O-P-$ chains.

Constant ν_{\max} for the anisotropic glass in regions 1 and 2 may be due to the onset of a decrease in ϕ . In these regions, the F_{M-O} of some of the $O^-P-O^- M^+$ local structures becomes smaller than the threshold F_{M-O} for maintaining the chain orientation ($F_{\text{threshold}}$), and hence ϕ becomes smaller. The number of local structures with these smaller F_{M-O} (N_{LS}) should increase with increasing temperature because there is a distribution of F_{M-O} depending on the different alkali cations and each F_{M-O} becomes smaller than $F_{\text{threshold}}$ in order of weakness of F_{M-O} with increasing temperature (**Fig. 3.9 (b) and (c)**). Consequently, the decrease in F_{M-O} and ϕ leads to the constant ν_{\max} . The increase in I_R for the anisotropic glass in regions 1 and 2 indicates a decrease in the number of oriented $-P-O-P-$ chains, and an increase in the $P-O^-$ bond strength, i.e. a decrease in the ionicity of $P-O^-$ bond, with the decrease in F_{M-O} . These changes lead to entropy relaxation from the anisotropic to the isotropic structure. Since shrinkage is small below T_g [1], a large proportion of the anisotropic structures must be maintained in region 1, but they convert rapidly to the isotropic structure in region 2. Therefore, the remarkable decrease in E' and increase in $\tan\delta$ for the anisotropic glass in region 1 was caused by the formation of local structures with small F_{M-O} and small ϕ , which enabled easy deformation of the oriented chain direction for the anisotropic glass in region 1 (**Fig. 3.9 (b)**). The highly oriented structure cannot be maintained in region 2 due to the increase of N_{LS} , and hence the glass shrinks in the direction of the oriented chains (**Fig. 3.9 (c)**). Therefore, the unusual increase in E' for the anisotropic glass in region 2 was caused by this significant shrinkage. Consequently, the relaxation of the anisotropic glass is induced by a partial loss of cross-linking between the oriented chains in region 1 and by a disordering of the oriented chain in region 2.

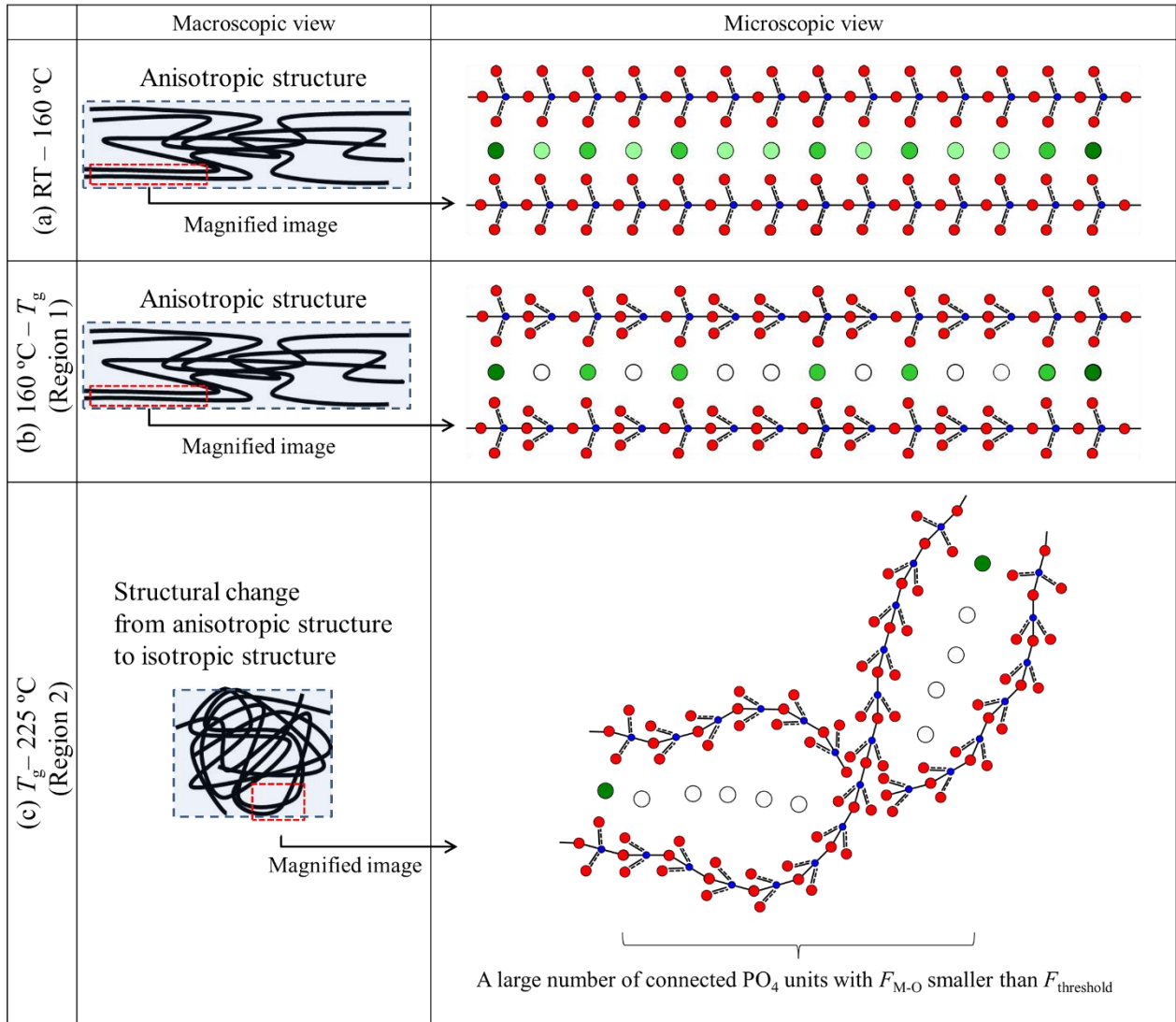


Fig. 3.9 Schematic illustrations of chain structures for anisotropic (Li,Na,K,Cs)PO₃ glass. Blue squares and black lines in the macroscopic view represent the shape of the glass and –P–O–P– chains. Darker green circles represent alkali cations with higher F_{M-O} . Large open circles represent alkali cations with F_{M-O} smaller than the $F_{threshold}$.

3.4 Conclusions

To clarify the relaxation mechanism for anisotropic (Li,Na,K,Cs)PO₃ glass, the change of dynamic mechanical property and structure was investigated from room temperature to above T_g for both anisotropic and isotropic glasses. Although E' for the isotropic glass gradually decreased with increasing temperature, E' for the anisotropic glass dropped markedly in region 1, and then increased to the value for the isotropic glass in region 2. From Raman spectra it was found that some local structures, which have smaller F_{M-O} than $F_{threshold}$, and smaller ϕ , appeared in oriented –P–O–P– chains around 160 °C. The N_{LS} increased with increasing temperature in regions 1 and 2. These results suggest that the relaxation mechanism for the anisotropic glass in region 1 was the partial loss of cross-linking between the oriented chains as some portion of the F_{M-O} exceed the $F_{threshold}$. At higher temperatures, in region 2, the ordering of the –P–O–P– chains was

largely lost as most of the F_{M-O} exceed the $F_{\text{threshold}}$. The coexistence of local structures with F_{M-O} smaller than $F_{\text{threshold}}$ and local structures with F_{M-O} larger than $F_{\text{threshold}}$ was play an important role in the unique relaxation of anisotropic (Li,Na,K,Cs)PO₃ glass. The results support the adequacy of the model of relaxation of oriented chains in anisotropic (Li,Na,K,Cs)PO₃ glass above T_g proposed by Inaba et al.

References

1. S. Inaba, H. Hosono, and S. Ito, Entropic shrinkage of an oxide glass, *Nat. Mater.* **14** 312–317 (2015).
2. B. N. Nelson and G. J. Exarhos, Vibrational spectroscopy of cation-site interactions in phosphate glasses, *J. Chem. Phys.* **71** 2739–2747 (1979).
3. G. B. Rouse, P. J. Miller, and W. M. Risen, Mixed alkali glass spectra and structure, *J. Non-Cryst. Solids* **28** 193–207 (1978).
4. D. E. C. Corbridge, Crystallographic data on some Kurrol salts, *Acta Crystallogr.* **8** 520 (1955).
5. E. V. Murashova and N. N. Chudinova, Synthesis and crystal structures of lithium polyphosphates, LiPO₃, Li₄H(PO₃)₅, and LiMn(PO₃)₃, *Crystallogr. Rep.* **46** 942–947 (2001).

Chapter 4: Unusual indentation behavior of alkali metaphosphate glass above the glass transition temperature

4.1 Introduction

Oxide glass can be formed into various shapes by applying compressive stress above the glass transition temperature (T_g) because glass exhibits viscous deformation above T_g . For example, there are cases that glasses are formed around 30–50°C higher than T_g in cutting-edge technologies, such as microlens molding [1], hot embossing [2,3], and nanoimprinting [4]. The shape of formed glasses is typically maintained in the annealed or cooled process above T_g after removing the forming stress.

Unique deformation behaviors due to entropic elasticity of 12.5Li₂O–12.5Na₂O–12.5K₂O–12.5Cs₂O–50P₂O₅ (mol%, (Li,Na,K,Cs)PO₃) metaphosphate glass under uniaxial tensile stress above T_g was observed [5]. On the other hand, although chains of (Li,Na,K,Cs)PO₃ glass is expected to orient by compressive stress and to show self-restoring behavior above T_g during removal of the compressive stress, deformation behaviors of (Li,Na,K,Cs)PO₃ glass under compressive stress above T_g is still unknown.

Depth-sensing indentation (DSI) techniques, in which the indentation load (P) and penetration depth of indentation probe (h) are monitored during both loading and unloading, have been used to measure not only the elastic–plastic behavior of oxide glasses at room temperature [6–12] but also the viscoelastic behavior of oxide glasses above T_g [13–15]. The merit of DSI techniques for materials showing viscous, elastic, and plastic deformation is that these deformations during indentation can be clarified by analyzing the P – h curves [16].

In this study, deformation behaviors of (Li,Na,K,Cs)PO₃ glass under compressive stress above T_g were investigated by analyzing viscoelastic–plastic behaviors during indentation above T_g because clarification of the behaviors will be useful knowledge for the development of applications of the glass which shows entropic elasticity above T_g .

4.2 Experimental procedure

(Li,Na,K,Cs)PO₃ glass shows much larger birefringence (significant anisotropic structures) compared to 50Li₂O–50P₂O₅ (mol%, LiPO₃) metaphosphate glass due to highly oriented –P–O–P– chains when the glasses were deformed under uniaxial tensile stress above T_g [5]. In this study, to investigate the deformation and self-restoring mechanism during indentation, the (Li,Na,K,Cs)PO₃ glass and LiPO₃ glass as a reference were used. Both glasses were prepared by melting mixtures of LiPO₃, 50Na₂O–50P₂O₅, 50K₂O–50P₂O₅ (mol%) (>99.7%, Rasa Industries), Cs₂CO₃ (>95%, FUJIFILM Wako Pure Chemical Corporation), and NH₄H₂PO₄ (>99%, FUJIFILM Wako Pure Chemical Corporation) in a 95%Pt–5%Au crucible at 1273 K for 1 h. To prepare the (Li,Na,K,Cs)PO₃ and LiPO₃ glasses, the melts were cast in a graphite mold, annealed at 503 or 613 K for 1 h, respectively, and then gradually cooled to room temperature. For the (Li,Na,K,Cs)PO₃ and LiPO₃ glasses, the transition temperatures measured by differential scanning calorimetry are 482 and 607

K, respectively.

The columnar sample of 4.95 mm in diameter and 5.57 mm in thickness for the annealed (Li,Na,K,Cs)PO₃ glass was compressed with a universal testing machine (Autograph AGS-X, Shimadzu Co., Ltd., Kyoto, Japan) to a load of 2.5 kN at a crosshead speed of 0.2 mm/s at 513 K and then cooled to room temperature maintaining their compressed lengths. The compressed glass with 3.11 mm in thickness and uncompressed glass were heated in a furnace from room temperature to above T_g to measure the change in the length during heating. For the measurement of the change in length, the contact load of the crosshead was 0.1 N.

Annealed (Li,Na,K,Cs)PO₃ and LiPO₃ glass samples of 10 mm in diameter and 3 mm in thickness were used to measure load–displacement ($P-h$) curves during indentation with a Berkovich indenter [14,15] above T_g . **Figure 4.1** shows a schematic illustration of the Berkovich indenter. The loading and unloading rate during indentation was 10 mN/s. The indentation load was monitored by a water-cooled load cell with a precision of ± 5 mN. The penetration depth is detected by an electro-optical extensometer via monitoring the separation of the slit made by a pair of silicon nitride tabs cemented at the side surfaces of the test specimen and indenter. Measurement of this slit-separation is very essential to eliminate undesirable displacements and mechanical clearances resulting from compliant test frames, test fixtures, and mechanical joints involved in the test system [6,14]. The precision and reproducibility of the measured penetration depth are within ± 0.5 μm . The peak load was 2 N. Viscous, elastic, and plastic deformation was analyzed using the $P-h$ curve. **Figure 4.2 (a) and (b)** shows the geometry of Berkovich and Vickers indenters, respectively [6]. Since the Berkovich geometry is easier to fabricate with a sharp tip than that for Vickers, the Berkovich indenter is widely utilized in depth-sensing nanoindentation systems than Vickers is [6].

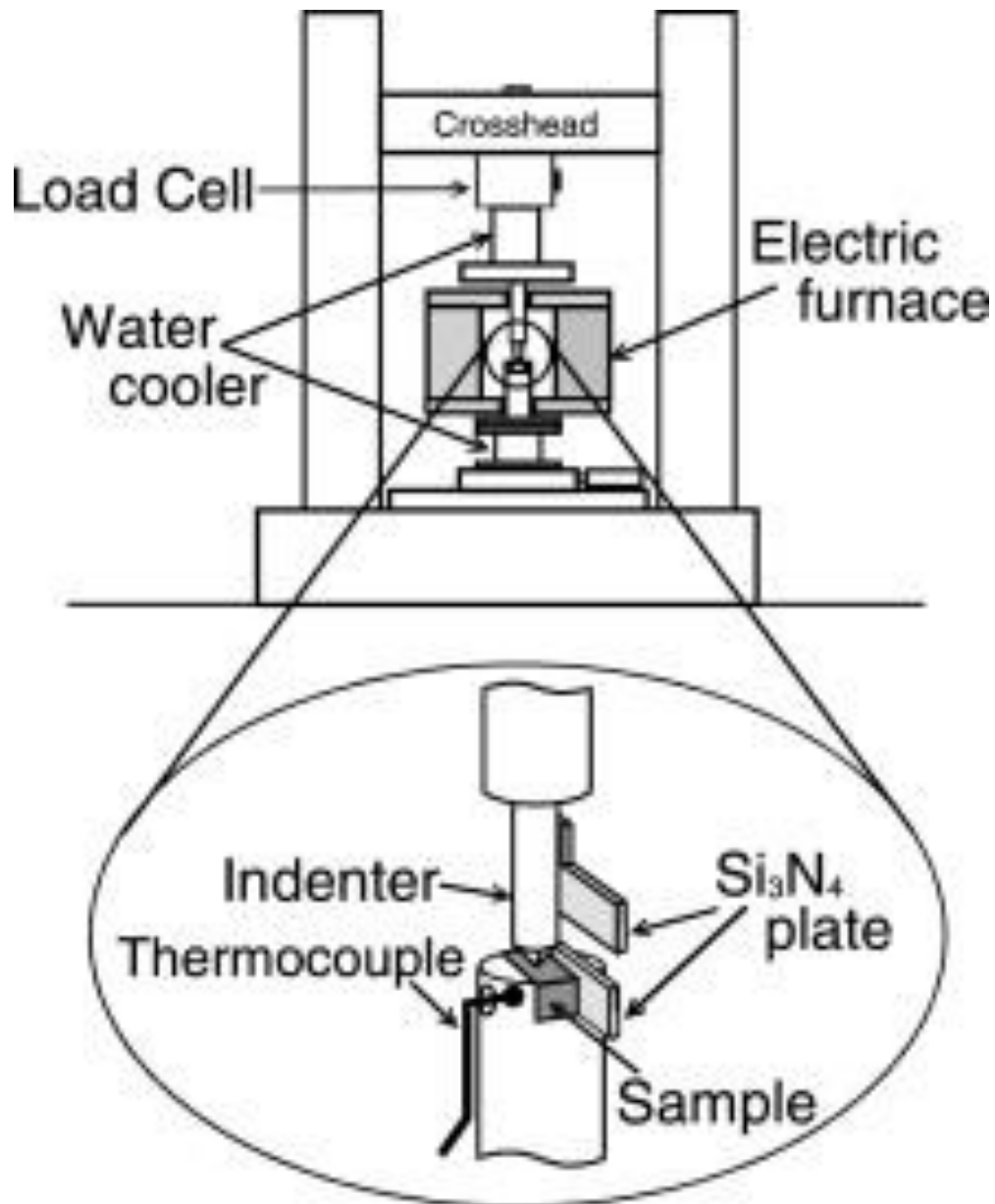
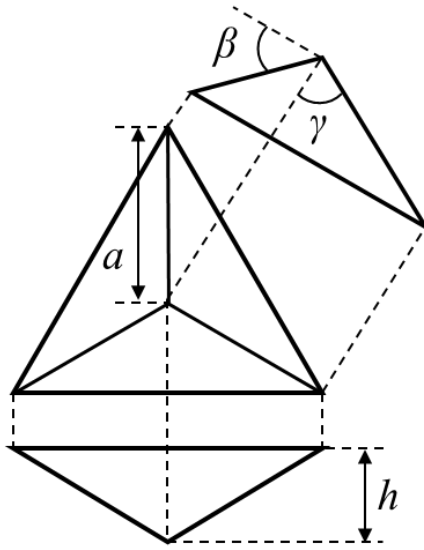


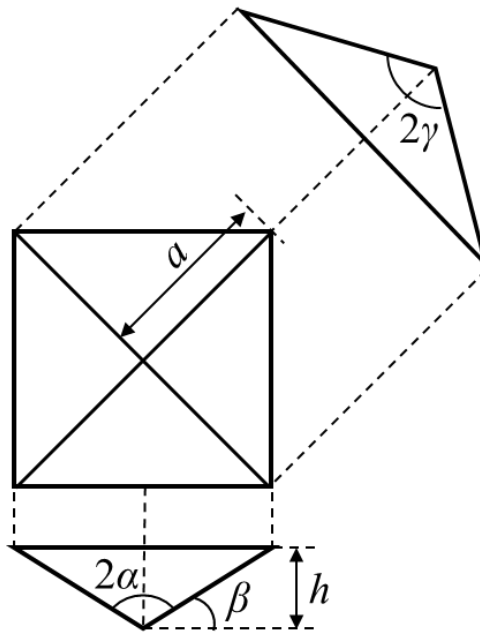
Fig. 4.1 Schematic illustration of a Berkovich indenter. Reproduced with permission from Ref. [14]. Copyright 2001, Elsevier Science B.V.

(a) Berkovich indenter



$$a = \frac{2}{\tan \beta} h, \beta = 24.7^\circ, \gamma = 77.1^\circ$$

(b) Vickers indenter



$$a = \frac{\sqrt{2}}{\tan \beta} h, \alpha = 136.0^\circ, \beta = 22.0^\circ, \gamma = 74.05^\circ$$

Fig. 4.2 Geometry of (a) Berkovich and (b) Vickers indenters. Reproduced with permission from Ref. [6]. Copyright 1999, Materials Research Society.

4.3 Results

Figure 4.3 shows the change in length of the (Li,Na,K,Cs)PO₃ glass uniaxially compressed at 513 K and uncompressed (Li,Na,K,Cs)PO₃ glass during heating. In the case of the compressed (Li,Na,K,Cs)PO₃ glass, a large increase in the length is observed above T_g . The recovery of the compressed length (2.46 mm) is about 11% (i.e., 0.28 mm). In the case of the uncompressed (Li,Na,K,Cs)PO₃ glass, a decrease in length caused by a decrease in viscosity is observed above T_g .

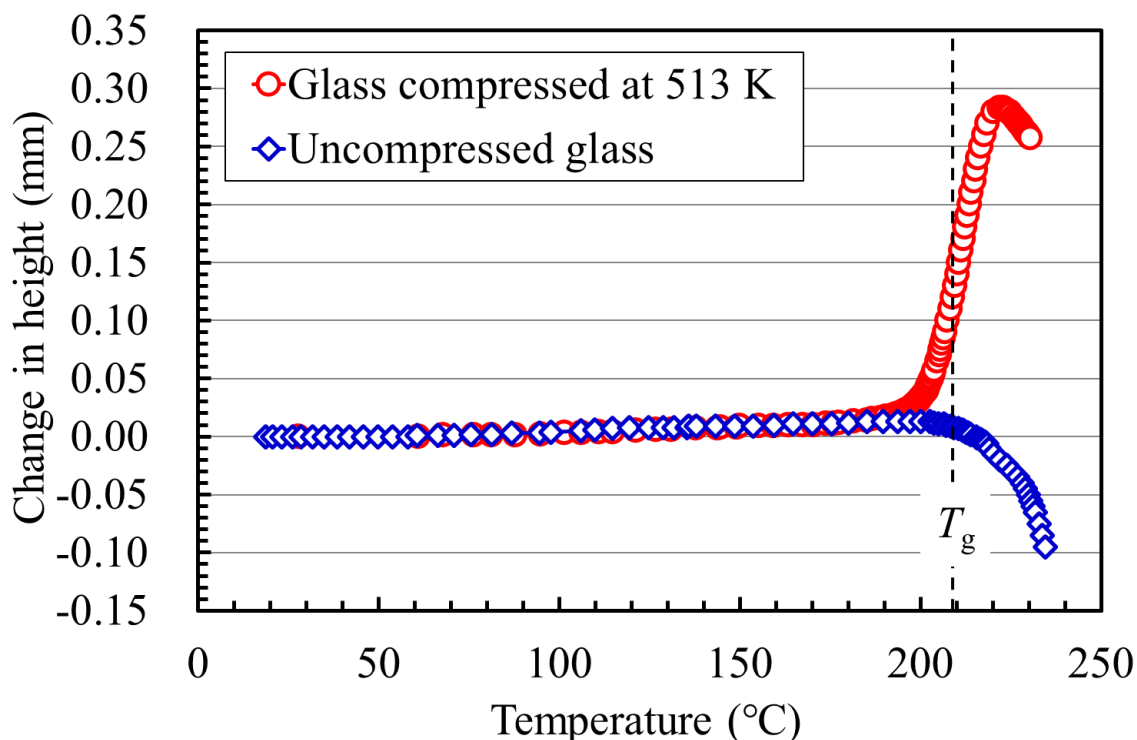


Fig. 4.3 Change in the height of (Li,Na,K,Cs)PO₃ glass compressed at 513 K and uncompressed (Li,Na,K,Cs)PO₃ glass during heating.

Figure 4.4 shows load–displacement ($P-h$) curves of (Li,Na,K,Cs)PO₃ glass at 493–523 K and LiPO₃ glass at 613 K. The penetration depth during loading increases with increasing temperature. The initial slopes of the unloading curves of (Li,Na,K,Cs)PO₃ glass at 503–523 K and LiPO₃ glass at 613 K are negative. The negative slopes are caused by viscous deformation. The recovery in the penetration depth of (Li,Na,K,Cs)PO₃ glass at 513 K during unloading is much larger than that of LiPO₃ glass at 613 K, although the penetration depth at the peak load of (Li,Na,K,Cs)PO₃ glass at 513 K is almost the same as that of LiPO₃ glass at 613 K.

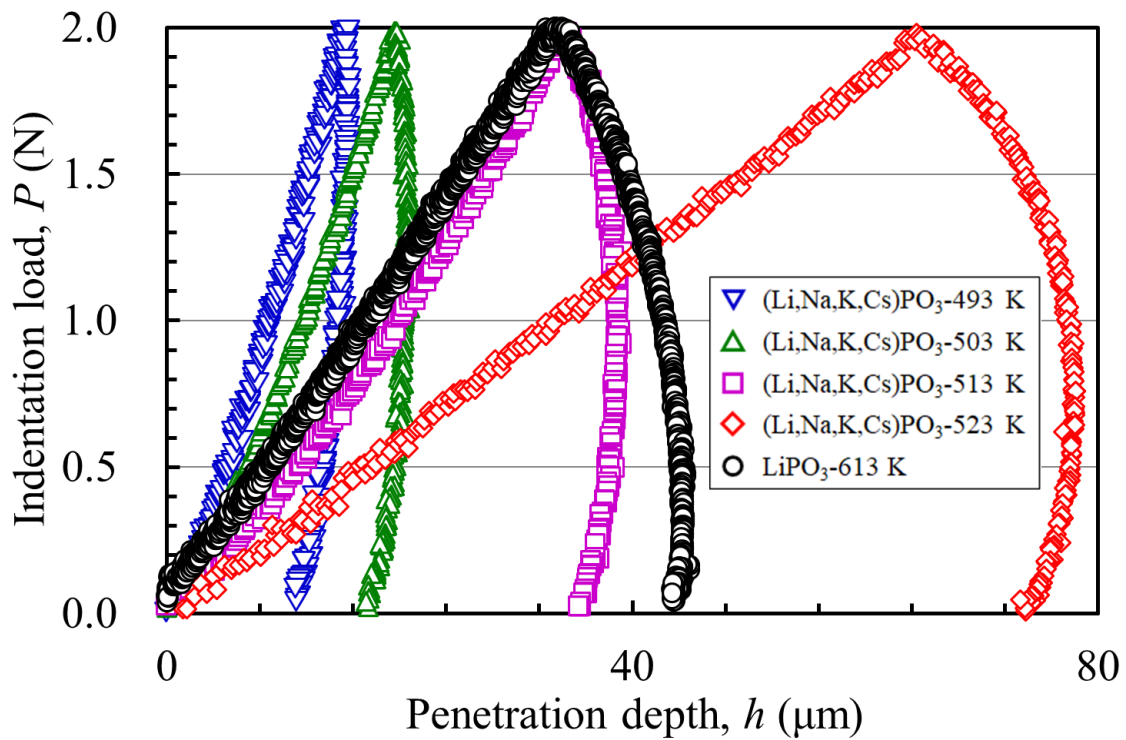


Fig. 4.4 Load–displacement curves of (Li,Na,K,Cs)PO₃ glass at 493, 503, 513, and 523 K, and LiPO₃ glass at 613 K.

Figure 4.5 shows P – h curves normalized by the penetration depth at the peak load for both glasses. The recovery in the penetration depth of (Li,Na,K,Cs)PO₃ glass during unloading decreases with increasing temperature. The recoveries of (Li,Na,K,Cs)PO₃ glass are larger than that of LiPO₃ glass, although the T (K)/ T_g (K) values of (Li,Na,K,Cs)PO₃ glass at 493–523 K are higher than that of LiPO₃ glass at 613 K (**Table 4.1**). The differences in the normalized P – h curves during unloading can be attributed to different contributions of elastic and permanent deformation (i.e., plastic and viscous deformation) to total deformation during unloading.

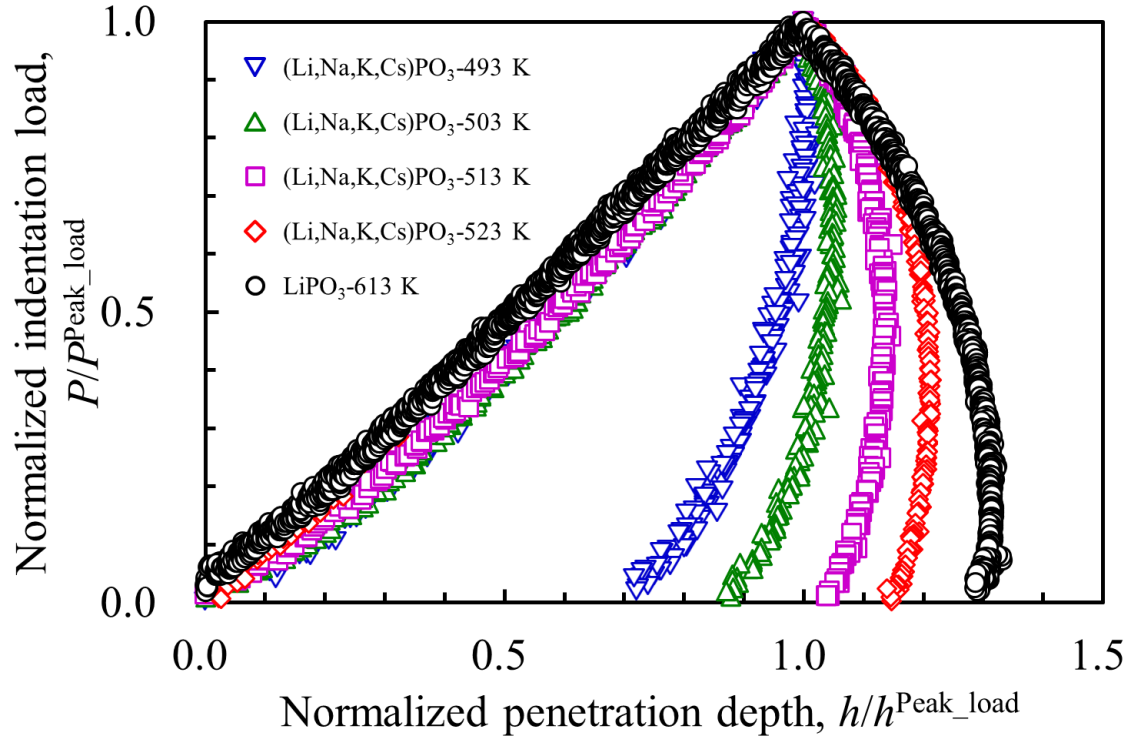


Fig. 4.5 Normalized load–displacement curves of (Li,Na,K,Cs)PO₃ glass at 493, 503, 513, and 523 K, and LiPO₃ glass at 613 K.

Table 4.1 Total, viscous, elastic, and plastic deformation at peak load of (Li,Na,K,Cs)PO₃ glass at 493–523 K and LiPO₃ glass at 613 K calculated using the viscous–elastic–plastic (VEP) model.

Glass	Temperature, T (K)	T/T_g (K)	$h_{cal}^{Peak_load}$ (μm)	$h_{V_cal}^{Peak_load}$ (μm)	$h_{E_cal}^{Peak_load}$ (μm)	$h_{P_cal}^{Peak_load}$ (μm)
(Li,Na,K,Cs)PO ₃	493	1.02	15.5	2.7	8.3	4.5
	503	1.04	19.7	5.5	9.7	4.6
	513	1.06	34.8	13.3	16.2	5.3
	523	1.09	66.8	30.1	30.0	6.7
LiPO ₃	613	1.01	34.1	18.0	10.8	5.2

h^{Peak_load} , $h_V^{Peak_load}$, $h_E^{Peak_load}$, and $h_P^{Peak_load}$ are the calculated total, viscous, elastic, and plastic deformation at peak load, respectively.

4.4 Discussion

To understand the mechanism of the large increase in length of the compressed (Li,Na,K,Cs)PO₃ glass during heating, the P – h curves of the (Li,Na,K,Cs)PO₃ and LiPO₃ glasses were analyzed. As shown in **Fig. 4.5**, a large indentation recovery occurs in (Li,Na,K,Cs)PO₃ glass during unloading above T_g compared with LiPO₃ glass. Such recovery is unusual indentation behavior in oxide glasses, although it is known for organic glasses [17–19].

The P – h curves of (Li,Na,K,Cs)PO₃ glass at 493–523 K and LiPO₃ glass at 613 K were analyzed with

the viscous–elastic–plastic (VEP) model [16], which describes the sharp indentation behavior of time-dependent materials. **Figure 4.6** shows a schematic illustration of the model. In **Fig. 4.6**, viscous, elastic, and plastic deformation are represented as dashpot, spring, and slider, respectively. P – h curves calculated using this model have been reported to agree well with experimental data of polymers at room temperature [16].

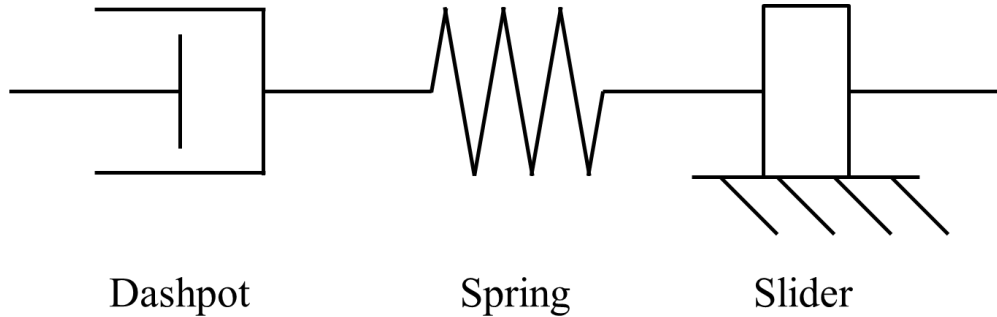


Fig. 4.6 Schematic illustration of the viscous–elastic–plastic (VEP) model.

The model constitutive equation is constructed from a series of quadratic mechanical elements with independent viscous (dashpot), elastic (spring), and plastic (slider) responses. In the case of constant loading-rate deformation, the loading (h^{Load}) and unloading (h^{Unload}) displacements are described by

$$h^{\text{Load}}(t) = h_V^{\text{Load}} + h_E^{\text{Load}} + h_P^{\text{Load}} = \frac{2}{3} \left(\frac{\dot{P}}{\alpha_3 \eta_Q} \right)^{\frac{1}{2}} t^{\frac{3}{2}} + \left(\frac{\dot{P}}{\alpha_2 E'} \right)^{\frac{1}{2}} t^{\frac{1}{2}} + \left(\frac{\dot{P}}{\alpha_1 H} \right)^{\frac{1}{2}} t^{\frac{1}{2}} \quad (4.1)$$

$$h^{\text{Unload}}(t) = h_V^{\text{Unload}} + h_E^{\text{Unload}} = \frac{2}{3} \left(\frac{\dot{P}}{\alpha_3 \eta_Q} \right)^{\frac{1}{2}} \left[t_R^{\frac{3}{2}} - (2t_R - t)^{\frac{3}{2}} \right] + \left(\frac{\dot{P}}{\alpha_2 E'} \right)^{\frac{1}{2}} \left[(2t_R - t)^{\frac{1}{2}} - t_R^{\frac{1}{2}} \right] + h^{\text{Load}}(t_R) \quad (4.2)$$

where h_V^{Load} , h_E^{Load} , and h_P^{Load} are the displacement of, respectively, viscous, elastic, and plastic deformation during loading, h_V^{Unload} and h_E^{Unload} are the displacement of, respectively, viscous and elastic deformation during unloading, \dot{P} is the loading rate [N/s], t is the time [s], t_R is the time at the peak load [s], μ_Q is the quadratic viscosity coefficient [Pa s²], $\eta_Q = \mu_Q/\alpha_3$ is the quadratic viscosity [Pa s²], E' is the plane strain modulus [GPa], H is the hardness [GPa], and α_1 , α_2 , and α_3 are geometry factors. The calculated h^{Load} , h_V^{Load} , h_E^{Load} , and h_P^{Load} values at peak load are shown in **Table 4.1**.

Figure 4.7 (a) and (b) show P – h curves of (Li,Na,K,Cs)PO₃ glass at 513 K and LiPO₃ glass at 613 K, respectively. Both glasses have almost the same penetration depth at 2 N. The measured total curves are well fitted with the calculated total curves except at low load, and they can be separated into three parts for viscous, elastic, and plastic deformation using Eqs. (4.1) and (4.2). Although $T/T_g = 1.06$ for (Li,Na,K,Cs)PO₃ glass is higher than $T/T_g = 1.01$ for LiPO₃ glass, the viscous and elastic deformations determined by Eqs. (4.1) and (4.2) for (Li,Na,K,Cs)PO₃ glass are much smaller and larger than those for LiPO₃ glass, respectively. Plastic deformation is almost the same for the two glasses.

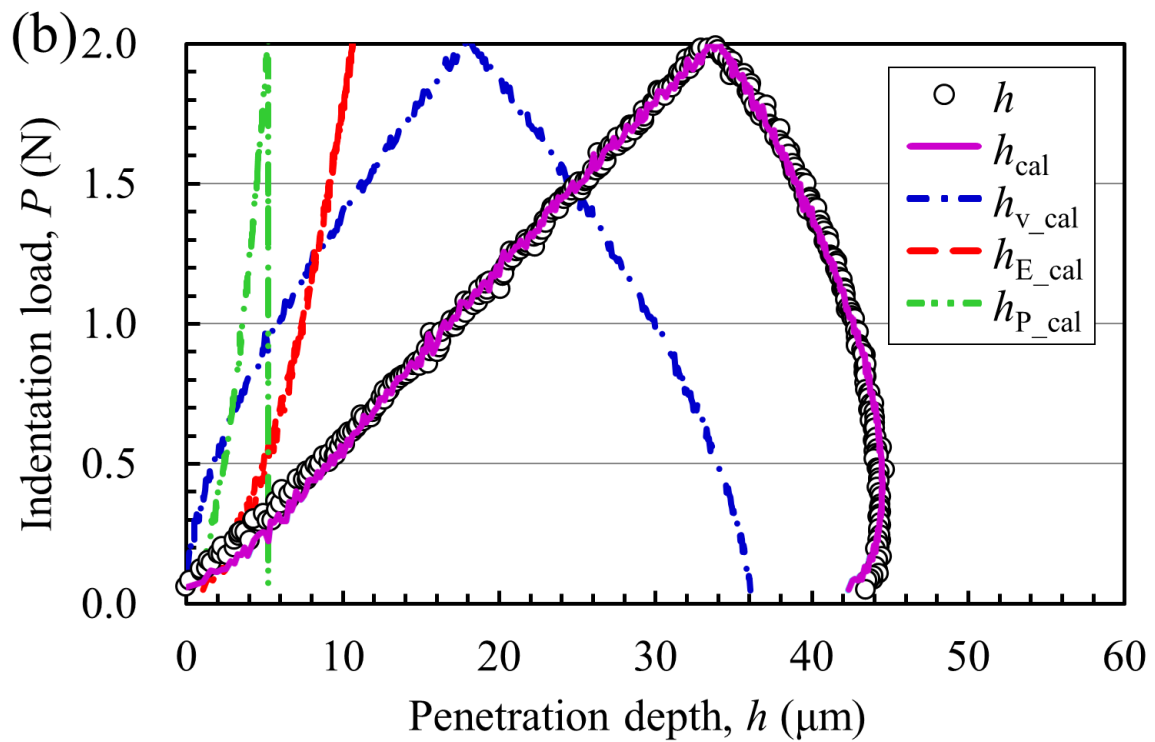
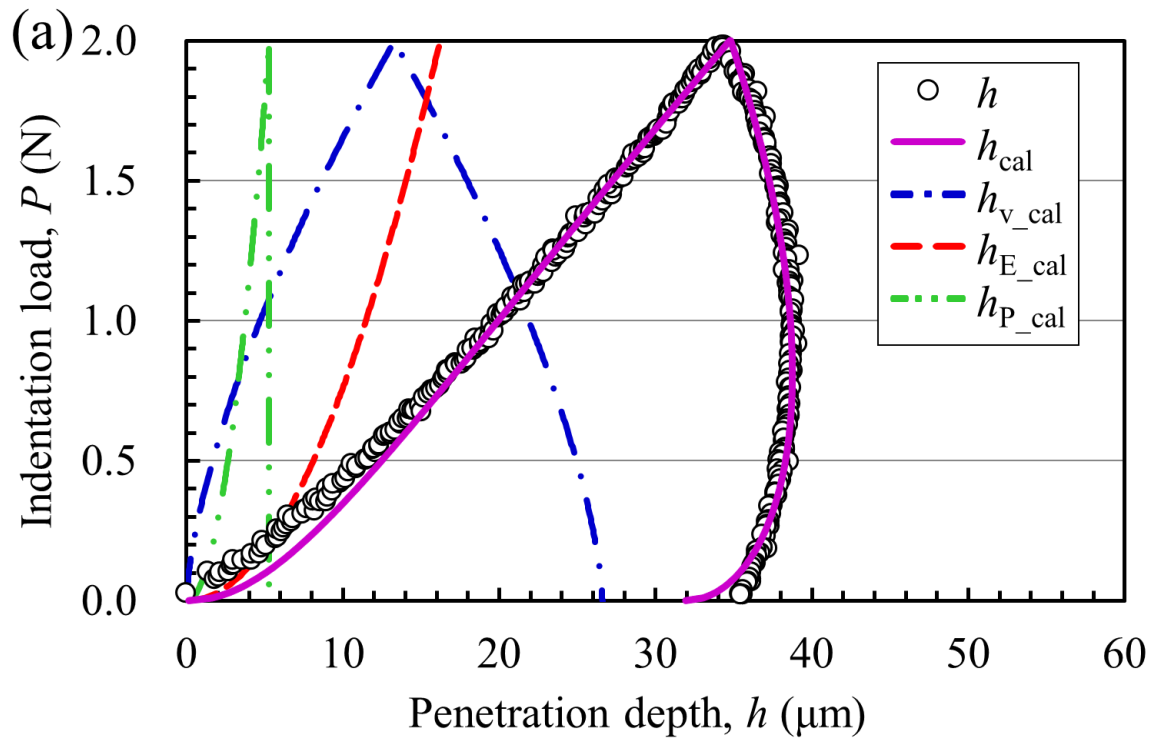


Fig. 4.7 Measured and calculated P - h , P - h_{v} , P - h_{E} , and P - h_{P} curves of (a) $(\text{Li,Na,K,Cs})\text{PO}_3$ glass at 513 K and (b) LiPO_3 glass at 613 K.

The contribution ratios of the elemental deformation to the total deformation at peak load were calculated using the following equations:

$$CR_V = \frac{h_V^{\text{Peak_load}}}{h_E^{\text{Peak_load}} + h_P^{\text{Peak_load}} + h_V^{\text{Peak_load}}} \times 100 \quad (4.3)$$

$$CR_E = \frac{h_E^{\text{Peak_load}}}{h_E^{\text{Peak_load}} + h_P^{\text{Peak_load}} + h_V^{\text{Peak_load}}} \times 100 \quad (4.4)$$

$$CR_P = \frac{h_P^{\text{Peak_load}}}{h_E^{\text{Peak_load}} + h_P^{\text{Peak_load}} + h_V^{\text{Peak_load}}} \times 100 \quad (4.5)$$

where CR_V , CR_E , and CR_P are the contribution ratios of viscous, elastic, and plastic deformation at the peak load, and $h_V^{\text{Peak_load}}$, $h_E^{\text{Peak_load}}$, and $h_P^{\text{Peak_load}}$ are the viscous, elastic, and plastic deformation at peak load (**Fig. 4.8**), respectively.

Figure 4.9 shows the contribution ratios for (Li,Na,K,Cs)PO₃ glass as a function of T/T_g . The contribution ratio for LiPO₃ glass at 613 K is plotted as a reference. For (Li,Na,K,Cs)PO₃ glass, the CR_E and CR_P values monotonically decrease and CR_V monotonically increases with increasing T/T_g . Since CR_P does not affect the behavior during unloading, it will not be discussed here. The CR_V and CR_E values of (Li,Na,K,Cs)PO₃ glass are much lower and higher than those of LiPO₃ glass, respectively, although the T/T_g values of (Li,Na,K,Cs)PO₃ glass are higher than that of LiPO₃ glass. Generally, CR_E is less than CR_V above T_g similar to those of LiPO₃ glass, and CR_E and CR_V , respectively, decreases and increases with increasing T/T_g . However, the unusually large recovery of (Li,Na,K,Cs)PO₃ glass during unloading (**Fig. 4.5**) is mainly attributed to the low CR_V and high CR_E values. In the case of (Li,Na,K,Cs)PO₃ glass at 493–523 K, these values indicate that the spring in the VEP model is easier to deform by applying stress during loading than the dashpot, and the contracted spring easily expands during unloading. In contrast, in the case of LiPO₃ glass at 613 K, the spring is more difficult to deform by applying stress during loading than the dashpot, and hence large viscous deformation remains without self-restoring after unloading. Consequently, the larger deformation of the spring than the dashpot takes place even above T_g for (Li,Na,K,Cs)PO₃ glass, and leads to the large recovery.

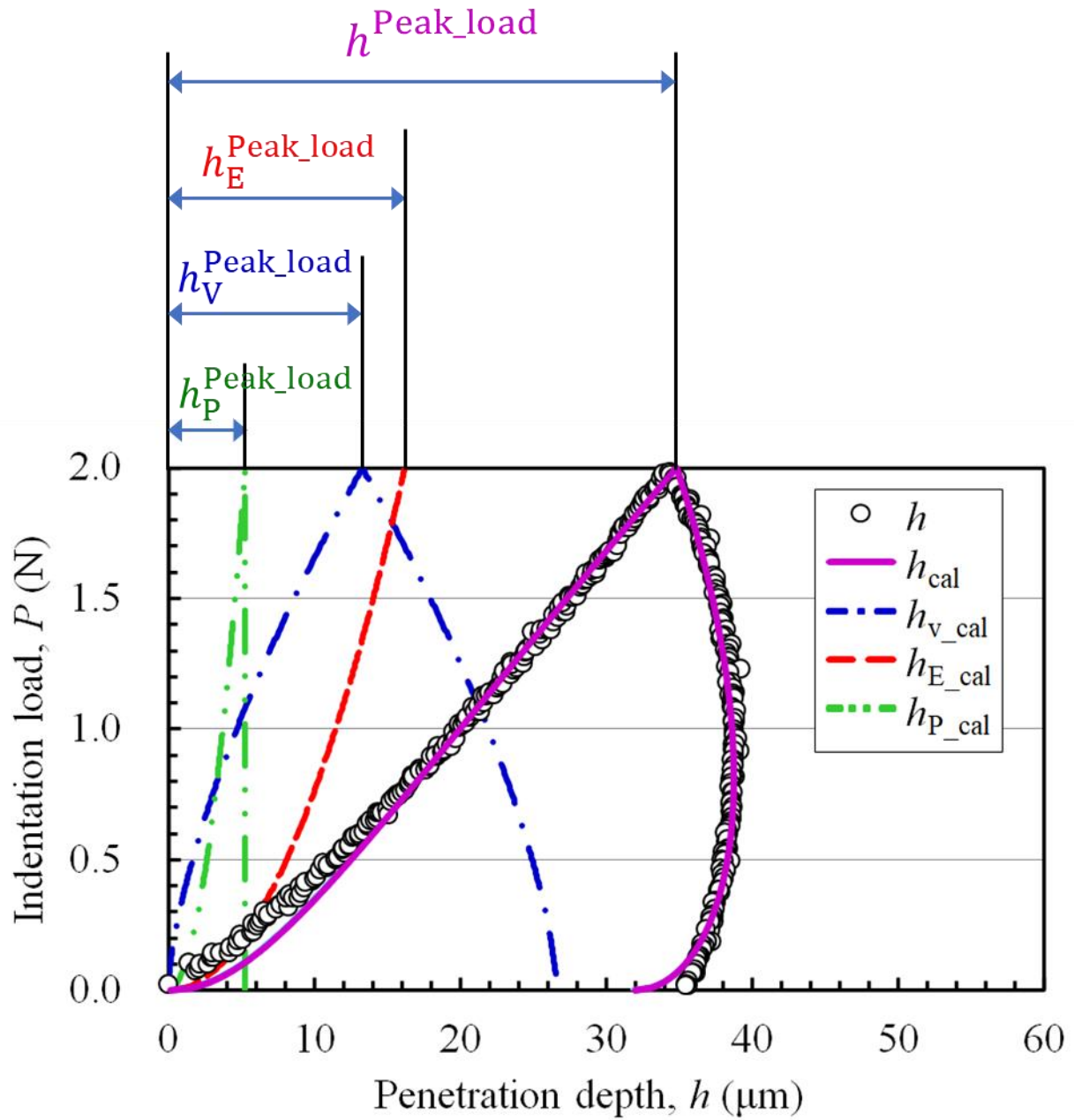


Fig. 4.8 Total ($h^{\text{Peak_load}}$), viscous ($h_v^{\text{Peak_load}}$), elastic ($h_E^{\text{Peak_load}}$), and plastic ($h_P^{\text{Peak_load}}$) deformation at the peak load

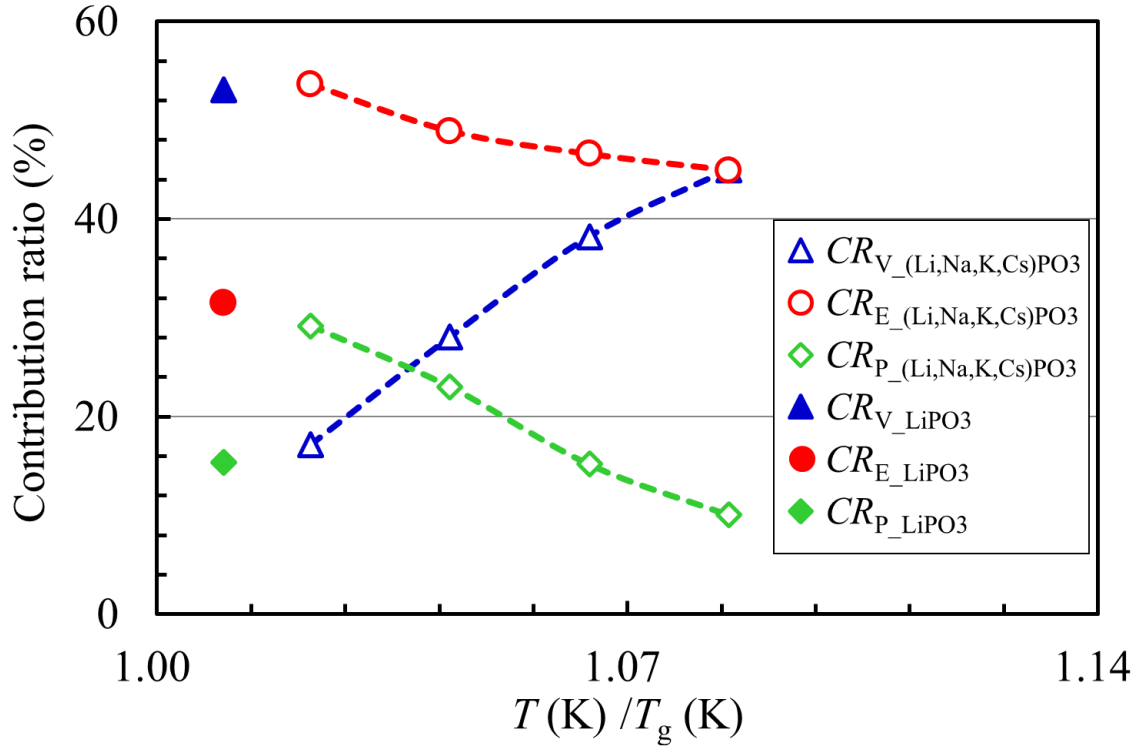


Fig. 4.9 Temperature (T/T_g) dependence of the contribution ratios of viscous, elastic, and plastic deformation of (Li,Na,K,Cs)PO₃ glass, and the contribution ratios of viscous, elastic, and plastic deformation of LiPO₃ glass.

Since (Li,Na,K,Cs)PO₃ glass shows a large anisotropy due to a highly oriented –P–O–P– chain structure formed under uniaxial tensile stress above T_g [5], compressive stress induced by indentation causes the orientation of –P–O–P– chains in (Li,Na,K,Cs)PO₃ glass; that is, a disordered structure of –P–O–P– chains gradually changes into an oriented structure with the increasing load during indentation up to peak load. As shown in **Fig. 4.7 (a)**, the measured and calculated P – h curves for (Li,Na,K,Cs)PO₃ glass at 513 K are not well fitted at low load during loading. This discrepancy should be caused by the change of orientation of –P–O–P– chains with increasing load. After that, a relaxation of the oriented structure of –P–O–P– chains to the original disordered structure occurs with a large elastic recovery in penetration depth during unloading. Consequently, the large CR_E values observed above T_g can be attributed to entropic elasticity caused by the orientation of –P–O–P– chains during loading and the relaxation of the oriented chains during unloading.

Uniaxial compressive stress above T_g also causes the orientation of –P–O–P– chains in the columnar sample of (Li,Na,K,Cs)PO₃ glass (**Fig. 4.10**). Relaxation of the oriented –P–O–P– chains occurs during heating above T_g (**Fig. 4.10**). The large shape recovery of the (Li,Na,K,Cs)PO₃ glass compressed above T_g shown in **Fig. 4.3**, therefore, results from the large contribution ratio of elastic deformation due to relaxation of the –P–O–P– chain structure oriented under uniaxial compressive stress above T_g (i.e., entropic elasticity).

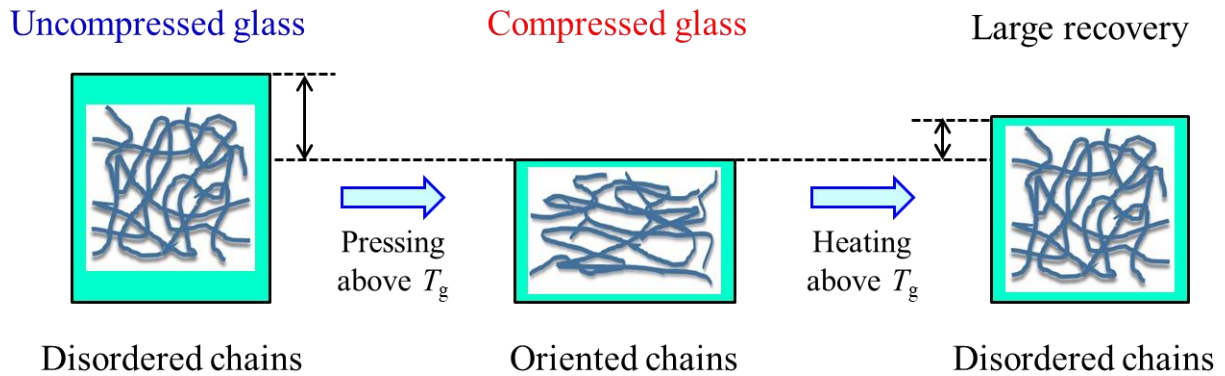


Fig. 4.10 Shape deformation of the columnar sample of $(\text{Li,Na,K,Cs})\text{PO}_3$ glass, and orientation and relaxation of chains of $(\text{Li,Na,K,Cs})\text{PO}_3$ glass.

4.5 Conclusions

The metaphosphate $(\text{Li,Na,K,Cs})\text{PO}_3$ chain-structured glass showed a self-restoring behavior from compressed deformation during heating above T_g . The viscoelastic–plastic behavior of $(\text{Li,Na,K,Cs})\text{PO}_3$ glass was investigated by depth-sensing indentation. The glass showed a large recovery in penetration depth during unloading above T_g in the range of 493–523 K. The recovery is much larger than that of LiPO_3 glass, although the relative temperature $T(\text{K})/T_g(\text{K})$ values of $(\text{Li,Na,K,Cs})\text{PO}_3$ glass at 493–523 K are higher than that of LiPO_3 glass at 613 K. By analyzing the P – h curves with the VEP model, the unusually large recovery of $(\text{Li,Na,K,Cs})\text{PO}_3$ glass is found to be due to a smaller and larger contribution of, respectively, viscous deformation and elastic deformation compared with LiPO_3 glass. The large elastic recovery observed above T_g in this study is attributed to entropic elasticity related to the orientation and relaxation of $-\text{P}-\text{O}-\text{P}-$ chain under indentation.

References

1. Y.-C. Tsai, C. Hung, and J.-C. Hung, Glass material model for the forming stage of the glass molding process, *J. Mater. Proc. Technol.* **201** 751–754 (2008).
2. J. Hung, Y. Tsai, and C. Hung, Development of a new apparatus for ultrasonic vibration-assisted glass hot embossing process, *Prec. Eng.* **37** 222–227 (2013).
3. M. Yasui, M. Takahashi, S. Kaneko, T. Tsuchida, Y. Hirabayashi, K. Sugimoto, J. Uegaki, and R. Maeda, Micro press molding of borosilicate glass using plated Ni–W molds, *Jpn. J. Appl. Phys.* **46** 6378–6381 (2007).
4. Y. Hirai, K. Kanakugi, T. Yamaguchi, K. Yao, S. Kitagawa, and Y. Tanaka, Fine pattern fabrication on glass surface by imprint lithography, *Microelectron. Eng.* **67–68** 237–244 (2003).
5. S. Inaba, H. Hosono, and S. Ito, Entropic shrinkage of an oxide glass, *Nat. Mater.* **14** 312–317 (2015).
6. M. Sakai, S. Shimizu, and T. Ishikawa, The indentation load–depth curve of ceramics, *J. Mater. Res.* **14** 1471–1484 (1999).
7. M. Sakai and Y. Nakano, Elastoplastic load–depth hysteresis in pyramidal indentation, *J. Mater. Res.* **17**

- 2161–2173 (2002).
8. M. Sakai, Elastic recovery in the unloading process of pyramidal microindentation, *J. Mater. Res.* **18** 1631–1640 (2003).
 9. M. Sakai, N. Hakiri, and T. Miyajima, Instrumented indentation microscope: A powerful tool for the mechanical characterization in microscales, *J. Mater. Res.* **21** 2298–2303 (2006).
 10. K. O. Kese, Z. C. Li, and B. Bergman, Influence of residual stress on elastic modulus and hardness of soda-lime glass measured by nanoindentation, *J. Mater. Res.* **19** 3109–3119 (2004).
 11. M. Radovic, E. Lara-Curzio, and L. Riester, Comparison of different experimental techniques for determination of elastic properties of solids, *Mater. Sci. Eng. A* **368** 56–70 (2004).
 12. J. A. Howell, J. R. Hellmann, and C. L. Muhlstein, Nanomechanical properties of commercial float glass, *J. Non-Cryst. Solids* **354** 1891–1899 (2008).
 13. C. Bernard, V. Keryvin, J.-C. Sangleboeuf, and T. Rouxel, Indentation creep of window glass around glass transition, *Mech. Mater.* **42** 196–206 (2010).
 14. M. Sakai and S. Shimizu, Indentation rheometry for glass-forming materials, *J. Non-Cryst. Solids* **282** 236–247 (2001).
 15. M. Sakai, S. Shimizu, and S. Ito, Viscoelastic indentation of silicate glasses, *J. Am. Ceram. Soc.* **85** 1210–1216 (2002).
 16. M. L. Oyen and R. F. Cook, Load–displacement behavior during sharp indentation of viscous–elastic–plastic materials, *J. Mater. Res.* **18** 139–150 (2003).
 17. R. V. S. Tatiraju and C.-S. Han, Rate dependence of indentation size effects in filled silicone rubber, *J. Mech. Mater. Struct.* **5** 277–288 (2010).
 18. C.-S. Han, S. H. R. Sanei, and F. Alisafaei, On the origin of indentation size effects and depth dependent mechanical properties of elastic polymers, *J. Polym. Eng.* **36** 103–111 (2015).
 19. Z. Li, J. C. M. Brokken-Zijp, and G. de With, Determination of the elastic moduli of silicone rubber coatings and films using depth-sensing indentation, *Polymer* **45** 5403–5406 (2004).

Chapter 5: Mechanical properties of anisotropic metaphosphate glass

5.1 Introduction

Glass is a typical brittle material and its fracture toughness is very low compared with that of ceramics, plastics, and metals. Glass is likely to break and its fracture strength markedly decreases when a flaw forms at its surface by contact damage with hard materials. As methods for increasing the fracture strength of glasses, (a) formation of composite structures in which crystal phases are dispersed in a glass matrix by controlling crystallization of glass, (b) formation of compressive stress layers by chemical strengthening in which smaller alkali cations in a glass surface are exchanged with larger alkali cations, and (c) thermal tempering in which a glass heated to near softening temperature is quenched are used. In the case of plastics composed of molecules with chain structures, fracture strength and Young's modulus are known to increase when the chain molecules are oriented uniaxially [1,2]. Although the orientation of $-P-O-P-$ chains in alkali metaphosphate glasses should increase fracture strength and Young's modulus similarly to the chain organic polymers, increase in fracture strength and Young's modulus by anisotropic structures in oxide glasses has not been reported so far.

Stockhorst et al. [3] obtained glasses with birefringence using the nozzle drawing method and reported that $25Li_2O-25Na_2O-50P_2O_5$ (mol%, $(Li,Na)PO_3$) glass in thin fibers less than $8\ \mu m$ in diameter had high birefringence ($\Delta n = 10000\ \text{nm/mm}$). However, it is difficult to obtain thick fibers with large anisotropy by the nozzle drawing method. The thickness of the $(Li,Na)PO_3$ fibers is too small to measure mechanical properties. Inaba et al. [4] found that the metaphosphate glass of $12.5Li_2O-12.5Na_2O-12.5K_2O-12.5Cs_2O-50P_2O_5$ (mol%, $(Li,Na,K,Cs)PO_3$) showed a large anisotropy, i.e., highly oriented $-P-O-P-$ chain structure, when the glass was deformed under uniaxial stress above the glass-transition temperature using a fiber elongation method followed by freezing of the deformed structure. In that method, glass fibers thicker than $60\ \mu m$ in diameter were obtained. The thick anisotropic fibers of $(Li,Na,K,Cs)PO_3$ glass showed high birefringence of $10600\ \text{nm/mm}$, whereas thick anisotropic fibers of $(Li,Na)PO_3$ glass prepared the same preparation conditions showed low birefringence of $1000\ \text{nm/mm}$.

In this study, the effect of the anisotropic structure of glasses on fracture strength and Young's modulus was investigated using $(Li,Na,K,Cs)PO_3$ glasses with different birefringence values for the development of a new method to improve fracture strength and Young's modulus of oxide glasses.

5.2 Experimental Procedure

A metaphosphate glass of $(Li,Na,K,Cs)PO_3$ was prepared by melting a mixture of $50Li_2O-50P_2O_5$, $50Na_2O-50P_2O_5$, and $50K_2O-50P_2O_5$ (mol%) ($> 99.7\%$, Rasa Industries), Cs_2CO_3 ($> 95\%$, FUJIFILM Wako Pure Chemical Corporation), and $NH_4H_2PO_4$ ($> 99\%$, FUJIFILM Wako Pure Chemical Corporation) in a $95Pt-5Au$ crucible at $1000^\circ C$ for 1 h. The melt was cast in a graphite mold, annealed at $230^\circ C$ for 1 h, and then cooled gradually to room temperature. An annealed glass plate of $50 \times 50 \times 3.5\ \text{mm}^3$ was used to measure the density, elastic modulus, and fracture toughness. The density was measured in dehydrated

ethanol using an Archimedean method. The speeds of the longitudinal and transverse waves passing through the glass plate were measured using an ultrasonic pulse method. Young's modulus (E), shear modulus (G), and Poisson's ratio (ν) are calculated by the following equations:

$$E = \frac{\rho V_L^2 (1 + \nu)(1 - 2\nu)}{1 - \nu} \quad (5.1)$$

$$G = \rho V_T^2 \quad (5.2)$$

$$\nu = \frac{1 - 2 \left(\frac{V_T}{V_L}\right)^2}{2 - 2 \left(\frac{V_T}{V_L}\right)^2} \quad (5.3)$$

with, V_L , speeds of the longitudinal wave; V_T , speeds of the transverse wave; ρ , density, respectively.

The fracture toughness was measured using an indentation fracture method. Halfpenny cracks are generated by indentation as shown in **Fig. 5.1**. The indentation load, temperature, and relative humidity were 500 gf, 22°C, and 0.4%, respectively. Equation (5.4), reported by Miyoshi *et al.* (JIS-R1607), was used to calculate the indentation fracture toughness (K_c) [5]:

$$K_c = 0.018 \left(\frac{E}{H_v}\right)^{\frac{1}{2}} \left(\frac{P}{c^{\frac{3}{2}}}\right) = 0.026 \frac{E^{\frac{1}{2}} P^{\frac{1}{2}} a}{c^{\frac{3}{2}}} \quad (5.4)$$

with, E , Young's modulus; H_v , Vickers hardness; P , the indentation load; c and a , the half-length of the crack and the indentation diagonal, respectively.

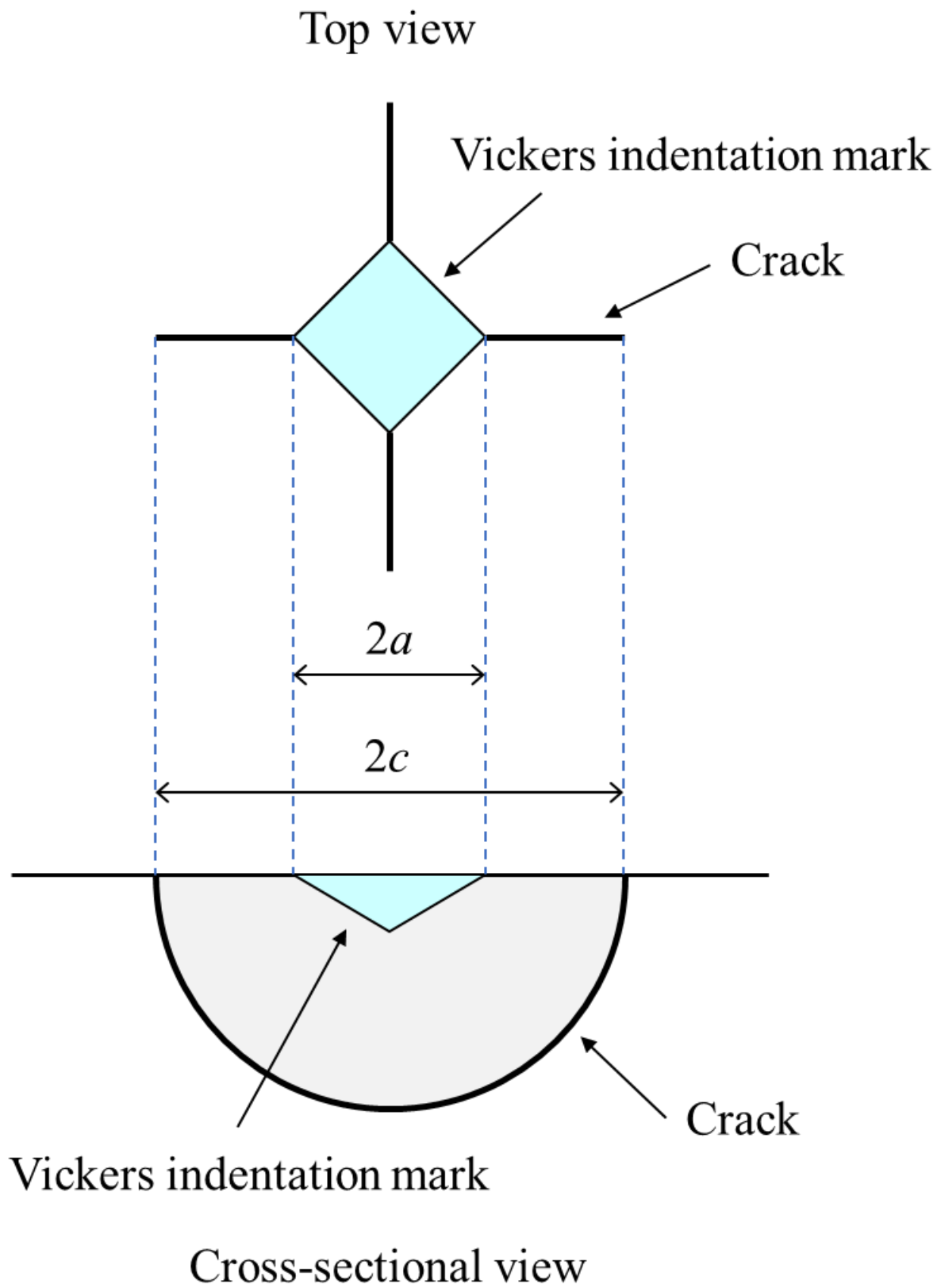


Fig. 5.1 Indentation mark and halfpenny cracks generated by Vickers indentation

Fibers of 60–90 μm in diameter were prepared by pulling a silica bar that was inserted into the glass melt. The cooling rate, which depended on the pulling speed of the fiber, was less than 3×10^2 K/s. The birefringence of the glass fibers was controlled by changing the temperature of the glass melt, pulling speed, and stress [3,4,6,7]. The birefringence (Δn) was determined from phase retardation (δ) measured using a polarization microscope with a quartz wedge and a de Sénarmont compensator. The birefringence is given by

$$\Delta n = \frac{\lambda \delta}{\pi d} \quad (5.5)$$

where d , δ , and λ are the fiber diameter, the phase retardation, and the light wavelength, respectively. The fracture strength and Young's modulus were measured with a three-point bending method with a span of 2.00 mm at 22°C in a relative humidity of 40% using a Micro Autograph (Shimadzu Co., Ltd., Kyoto, Japan). The crosshead speed was 1.0 mm/min.

5.3 Results

Figure 5.2 shows polarization microscope images of isotropic and anisotropic (Li,Na,K,Cs)PO₃ glass fibers. The birefringence of the glass fibers was controlled by changing the pulling conditions. Anisotropic fibers with birefringence values of 0–10600 nm/mm were obtained. The standard deviation of the measured birefringence values was 150 nm/mm. Although birefringence in glass is known to be generated through thermal stress during cooling, such large birefringence cannot be caused by the thermal stress induced under the experimental conditions, e.g., fiber thickness, thermal conductivity, and cooling rate in this study. The birefringence, therefore, must be caused by the anisotropic structure in the glass [4].

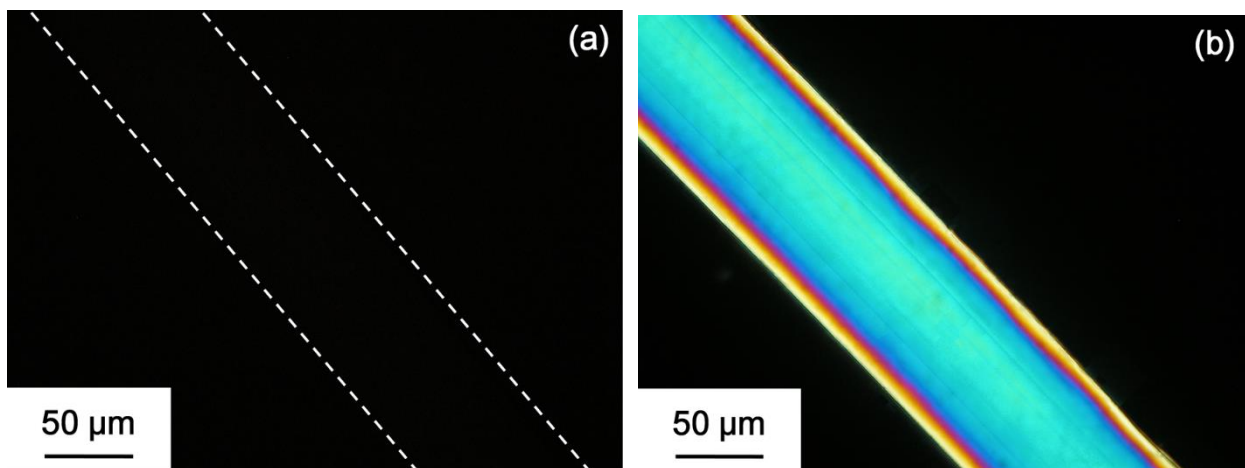


Fig. 5.2 Polarization microscope images of (a) isotropic and (b) anisotropic (Li,Na,K,Cs)PO₃ glass fibers. The birefringence of the anisotropic glass was 7200 nm/mm. The white dashed lines show the edges of the isotropic glass fiber.

Figure 5.3 shows a Weibull plot of the fracture strength for the isotropic (Li,Na,K,Cs)PO₃ glass fiber. The average fracture strength and standard deviation were 890 and 70 MPa, respectively; the fracture strength showed a slight deviation at low fracture strength values.

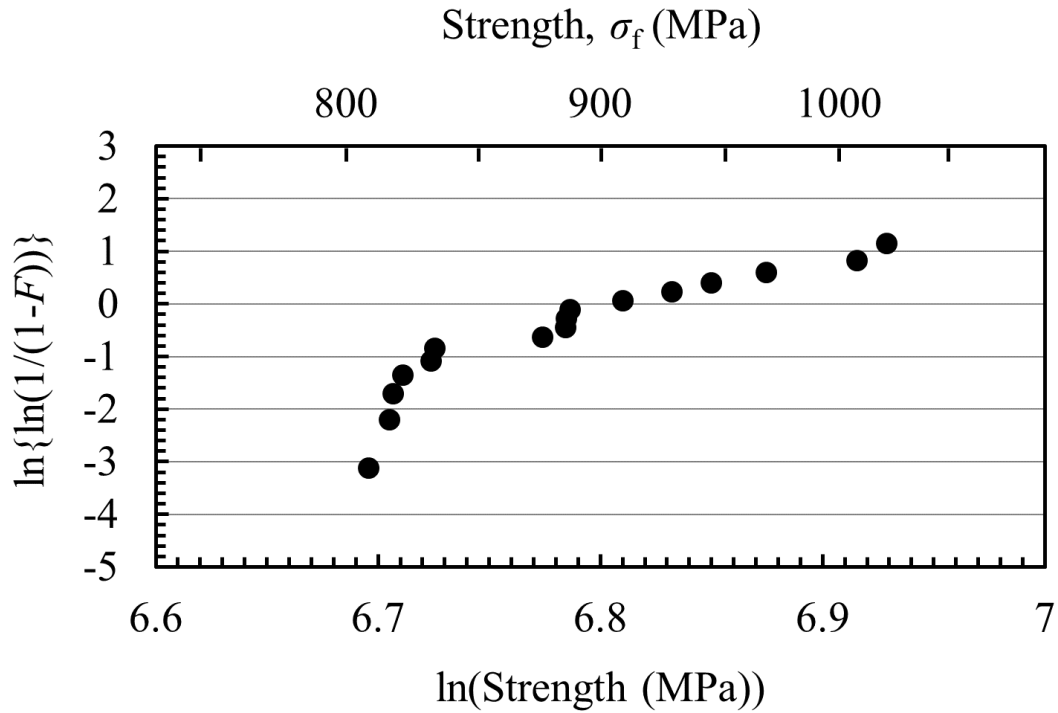


Fig. 5.3 Weibull plot of the fracture strength of isotropic (Li,Na,K,Cs)PO₃ glass fiber. F is the cumulative failure probability.

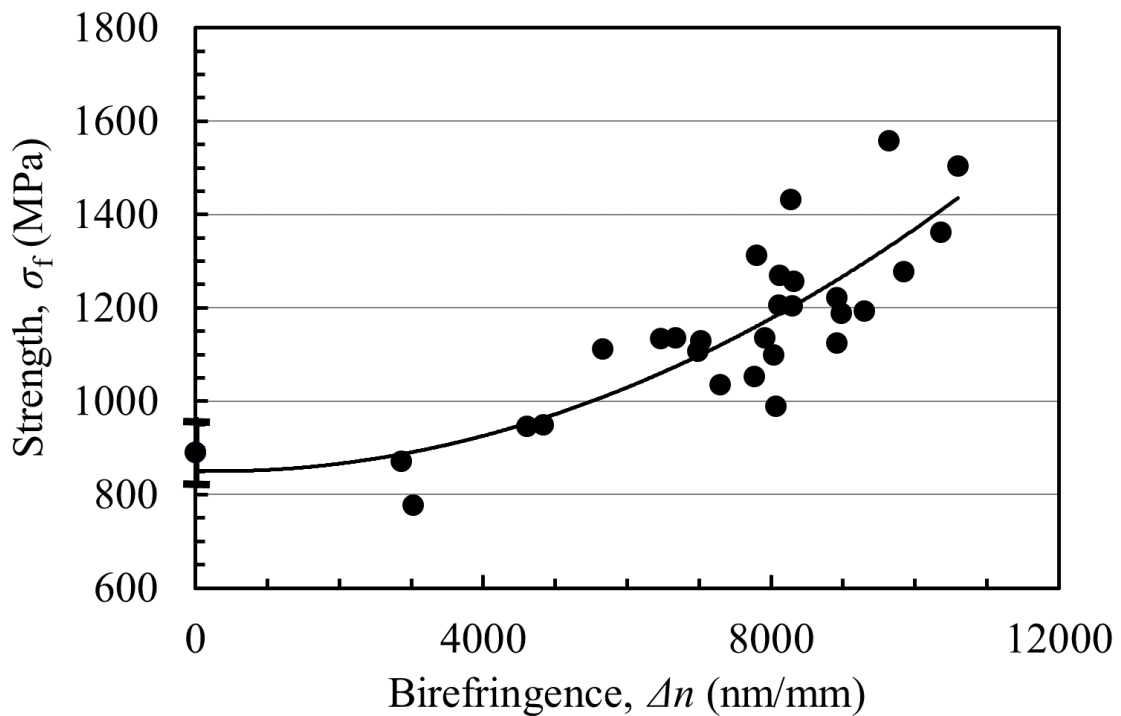


Fig. 5.4 Fracture strength of (Li,Na,K,Cs)PO₃ glass fibers for different birefringence values. An error bar is shown for the isotropic glass fiber. The spreading of the data points of anisotropic glasses is attributed to the experimental errors caused mainly by the diameter uniformity of fiber. The line is a guide for the eyes.

Figure 5.4 shows the relationship between the birefringence and fracture strength. The fracture strength of the anisotropic glass fiber increased with increasing birefringence, especially above 5000 nm/mm, and reached about 160% of the fracture strength of the isotropic glass fiber.

Table 5.1 shows the density, Young’s modulus, Poisson’s ratio, and indentation fracture toughness measured using an ultrasonic pulse method for the isotropic bulk glass of (Li,Na,K,Cs)PO₃. The Young’s modulus and indentation fracture toughness are almost consistent with the values reported for alkali metaphosphate glasses by Ashizuka *et al* [8].

Table 5.1 Properties of isotropic bulk (Li,Na,K,Cs)PO₃ glass

Glass	ρ (g/cm ³)	E (GPa)	ν	K_c (MPa·m ^{1/2})	Reference
(Li,Na,K,Cs)PO ₃	2.81	34	0.29	0.46	This work
50Li ₂ O–50P ₂ O ₅ (mol%)		50		0.57	Ashizuka et al. [8]
50Na ₂ O–50P ₂ O ₅ (mol%)		36		0.35	Ashizuka et al. [8]

ρ , E , ν , and K_c are the density, Young’s modulus, Poisson’s ratio, and indentation fracture toughness, respectively.

Figure 5.5 shows stress–strain curves measured by the three-point bending method for the isotropic and anisotropic glass fibers of (Li,Na,K,Cs)PO₃. The Young’s moduli of the glasses were calculated from the slope of the curves at a strain of 1%.

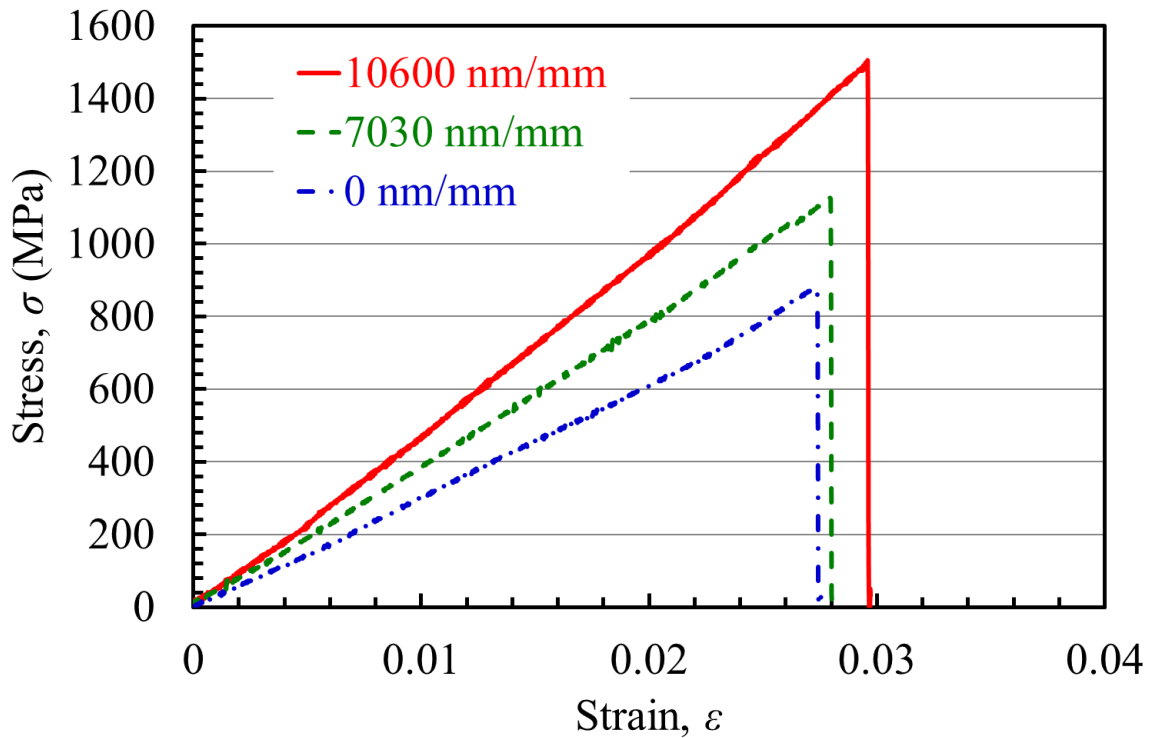


Fig. 5.5 Stress–strain curves of (Li,Na,K,Cs)PO₃ glass fibers.

The Young's modulus and standard deviation of the isotropic glass fiber were 32 and 2 GPa, respectively. This value was approximately equal to the modulus of the isotropic bulk glass as shown in **Table 5.1**. The moduli of the anisotropic glass fibers, however, were larger than that of the isotropic glass fiber.

Figure 5.6 shows Young's modulus parallel to the fiber axis as a function of birefringence. The modulus was found to increase with increasing birefringence and reached about 140% of the modulus of the isotropic glass fiber.

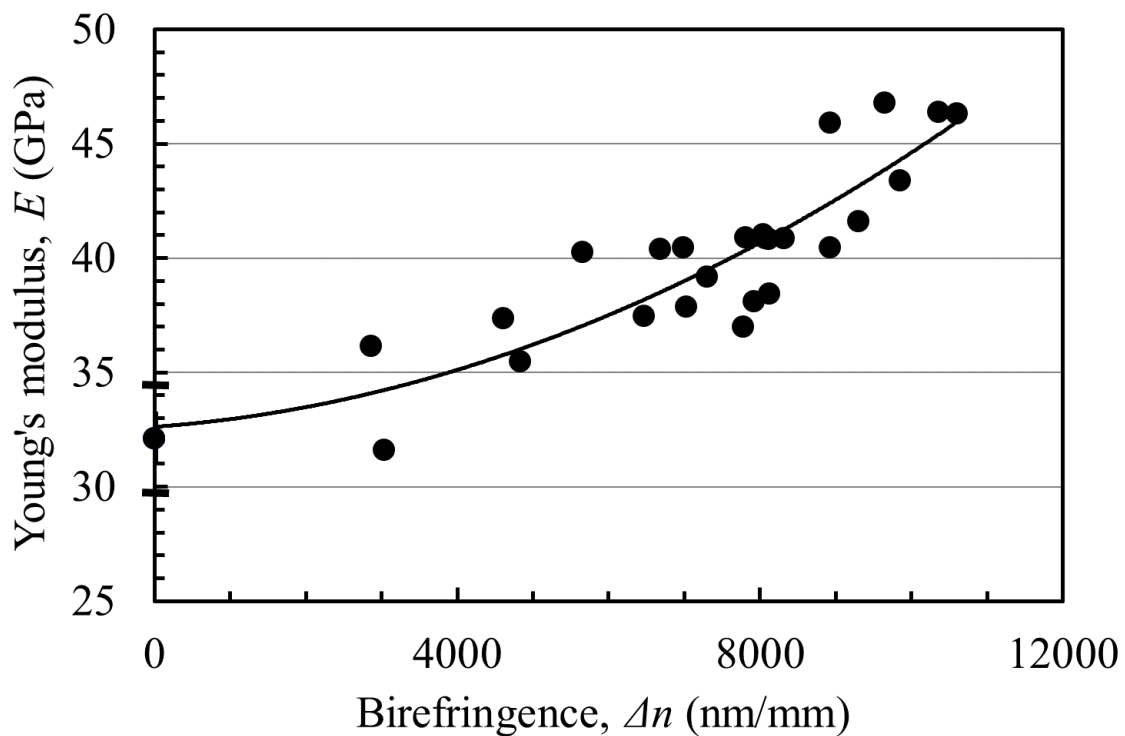


Fig. 5.6 Young's moduli parallel to the axis of (Li,Na,K,Cs)PO₃ glass fibers as a function of birefringence. An error bar is shown for the isotropic (Li,Na,K,Cs)PO₃ glass fiber. The spreading of the data points of anisotropic glasses is attributed to the experimental errors caused mainly by the diameter uniformity of fiber. The line is a guide for the eyes.

5.4 Discussion

5.4.1 Increase in fracture strength

The structure of the (Li,Na,K,Cs)PO₃ glass obtained in this study consists of chains with considerable length [4] and changes an anisotropic structure with preferentially oriented chains induced by the occurrence of non-Newtonian flow [9–11] under stress.

The fracture strength of the anisotropic glasses increased with increasing birefringence as shown in **Figure 5.4**. Since the increase in fracture strength was much larger than the standard deviation (70 MPa) of the isotropic glass derived from the difference in crack lengths, the increase can be attributed to anisotropic

structures in the glass.

The fracture strength (σ_f) is given by Equation (5.6) because the fracture surface energy is known to be proportional to the Young's modulus [12–14]:

$$\sigma_f = \frac{K_{Ic}}{Y\sqrt{c}} = \frac{1}{Y\sqrt{c}} \sqrt{\frac{2E\gamma}{1-\nu^2}} = \frac{\alpha E}{Y\sqrt{c(1-\nu^2)}} \quad (5.6)$$

with, K_{Ic} : the fracture toughness; Y : the geometry factor; c : the crack length; E : Young's modulus; γ : the fracture surface energy; ν : Poisson's ratio; α : a constant.

According to Equation (5.6), the fracture strength is proportional to Young's modulus. **Figure 5.7** shows the relationship between the normalized fracture strength (σ_f/σ_{f0}) and Young's modulus (E/E_0), where σ_{f0} and E_0 are the fracture strength and Young's modulus of the isotropic glass, respectively. The normalized fracture strength increased with increasing normalized Young's modulus. When the birefringence was 10600 nm/mm, σ_f/σ_{f0} (= 1.6) was larger than E/E_0 (= 1.4). The dashed line in **Fig. 5.7** is drawn according to Equation (5.6) assuming that all other factors except E are constant. The coefficient of determination (R^2) of the line is 0.34, indicating that the line does not fit the data well. This means that although the increase in fracture strength is mainly caused by the increase in Young's modulus, other factors also contribute, as discussed below.

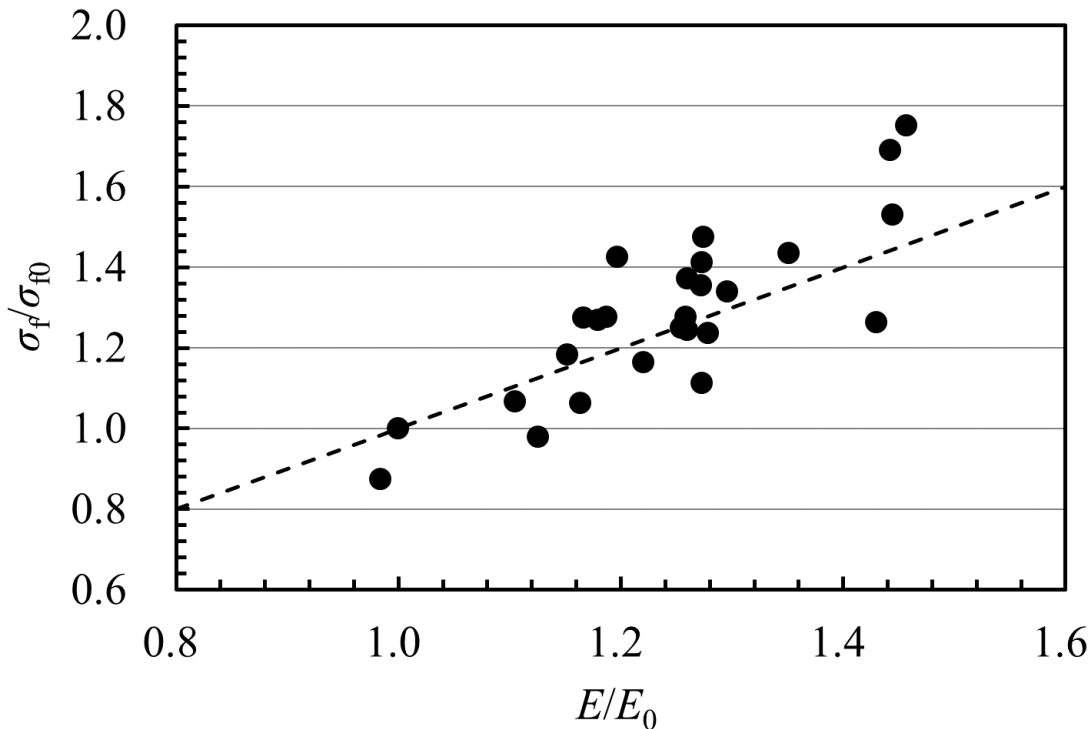


Fig. 5.7 Relationship between the normalized fracture strength and Young's moduli of (Li,Na,K,Cs)PO₃ glass fibers. σ_{f0} and E_0 are the fracture strength and Young's modulus of the isotropic glass fiber, respectively. The dashed line is drawn according to Equation $\sigma_f/\sigma_{f0} = E/E_0$.

5.4.2 Increase in Young's modulus

The chain in the metaphosphate glass is known to comprise a $-P-O-P-$ main chain with $-P-O-M$ side chains. The force constants of the $M-O$ bonds (0.08–0.27 N/cm) [15] are much smaller than that of the $P-O$ bond (6 N/cm) [16,17]; that is, the force constant of the $P-O$ bond is more than one order of magnitude larger than those of $M-O$ bonds. The Young's modulus in the parallel direction to the direction of the main chain, therefore, is expected to be higher than that in the perpendicular direction as shown in **Fig. 5.8**.

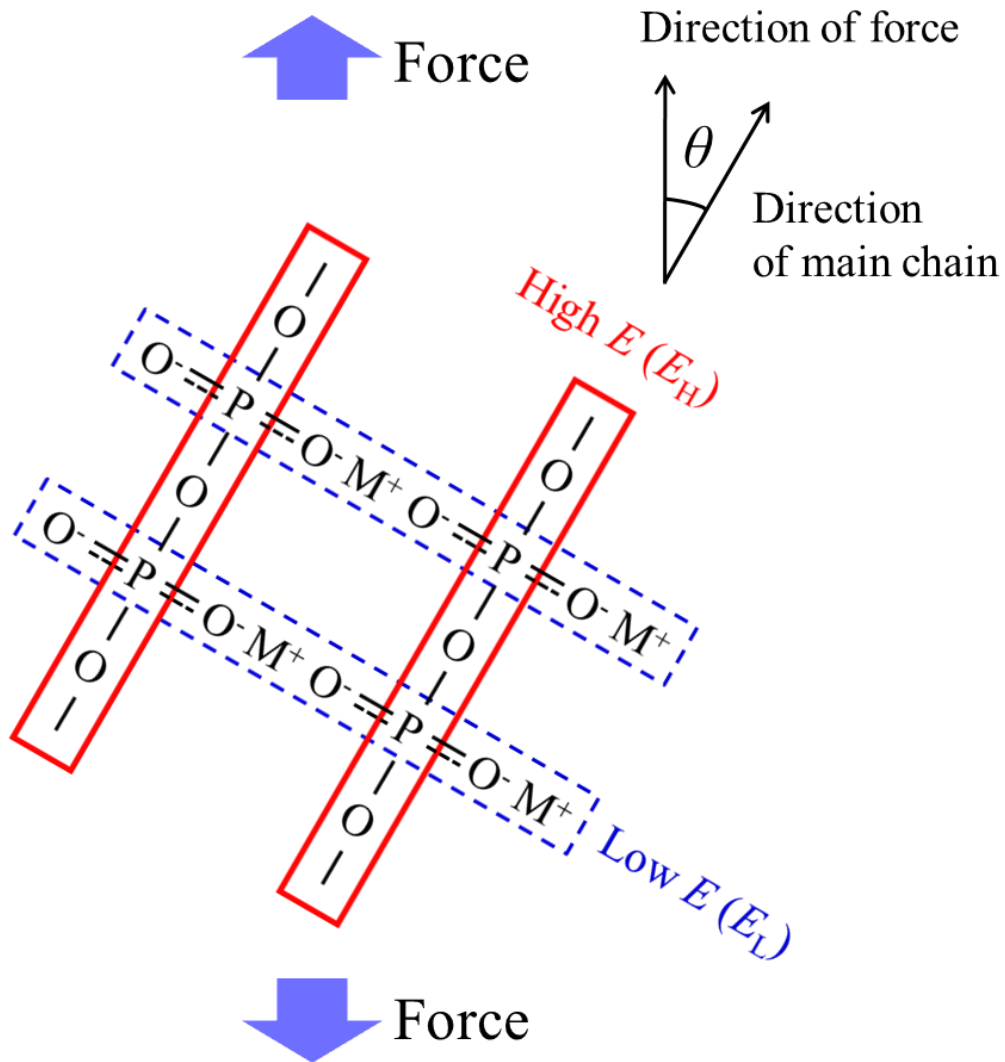


Fig. 5.8 Schematic illustration of the chain structure of $(Li,Na,K,Cs)PO_3$ glass. Alkali cations are represented as M^+ . E_H and E_L are Young's moduli in the parallel and perpendicular directions to the chain axis, respectively.

If a polymer has a uniaxial structure composed of an assembly of extended polymer chains, Young's modulus in the tensile direction increases with decreasing angle between the tensile direction and the

direction of the chain axis [18]. Therefore, in the case of a metaphosphate glass like an organic polymer, Young's modulus is expected to increase with a decrease in angle (i.e., an increase in birefringence), as shown in Fig. 5.8.

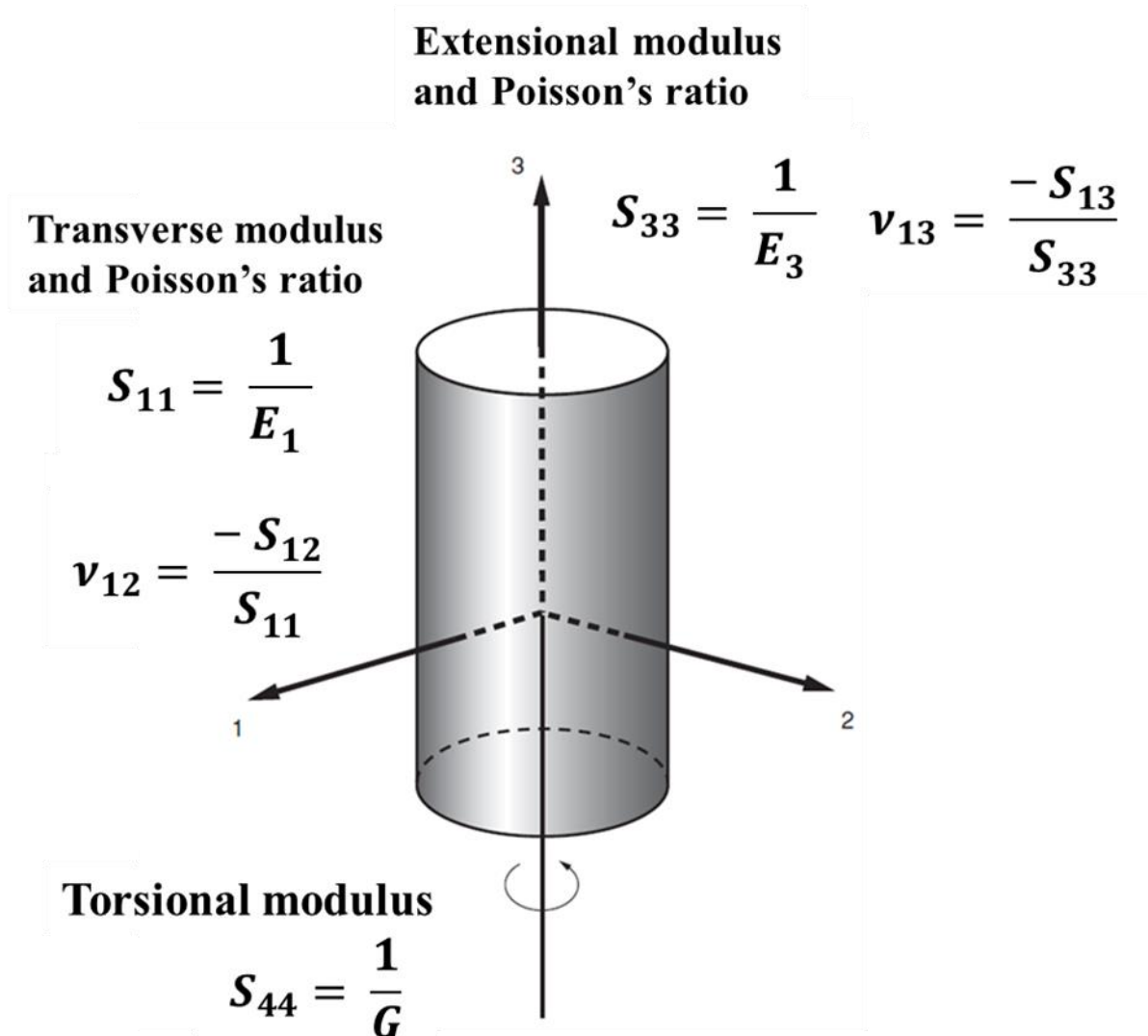


Fig. 5.9 The fiber compliance constants. Reproduced with permission from Ref. [19]. Copyright 2013, John Wiley & Sons, Ltd.

The compliance matrix S_{ij} for specimens possessing fiber symmetry is represented below [19].

$$\begin{pmatrix} S_{11} & S_{12} & S_{13} & 0 & 0 & 0 \\ S_{12} & S_{11} & S_{13} & 0 & 0 & 0 \\ S_{13} & S_{13} & S_{33} & 0 & 0 & 0 \\ 0 & 0 & 0 & S_{44} & 0 & 0 \\ 0 & 0 & 0 & 0 & S_{44} & 0 \\ 0 & 0 & 0 & 0 & 0 & 2(S_{11} - S_{12}) \end{pmatrix}$$

The compliance in the tensile direction for a uniaxial structure composed of an assembly of extended

polymer chains ($S'_{33} = 1/E$) is given by Equation (5.7) [19]:

$$S'_{33} = S_{11}\sin^4\theta + S_{33}\cos^4\theta + (2S_{13} + S_{44})\sin^2\theta\cos^2\theta \quad (5.7)$$

where S_{33} ($= 1/E_{33} = 1/E_H$) and S_{11} ($= 1/E_{11} = 1/E_L$) are the compliance, respectively, in the parallel and perpendicular directions to the chain axis, E_H and E_L are Young's moduli in the parallel and perpendicular directions to the chain axis, respectively, and θ is the angle between the tensile direction and the direction of the chain axis.

Equation (5.7) can be expressed as Equation (5.8) using the Poisson's ratio (ν_{13}):

$$S'_{33} = S_{11}\sin^4\theta + S_{33}\cos^4\theta + (-2\nu_{13}S_{33} + S_{44})\sin^2\theta\cos^2\theta \quad (5.8)$$

The degree of orientation (F) is given by Equation (5.9) [19]:

$$F = \frac{\Delta n}{\Delta n_{\max}} = 1 - \frac{3}{2}\sin^2\theta \quad (5.9)$$

where Δn_{\max} is the maximum birefringence between the parallel and perpendicular directions to the chain.

Combining Equations (5.8) and (5.9) leads to Equation (5.10):

$$S'_{33} = \frac{4}{9}\left(1 - \frac{\Delta n}{\Delta n_{\max}}\right)^2 S_{11} + \frac{4}{9}\left(\frac{1}{2} + \frac{\Delta n}{\Delta n_{\max}}\right)^2 S_{33} + \frac{4}{9}\left(1 - \frac{\Delta n}{\Delta n_{\max}}\right)\left(1 - \frac{\Delta n}{\Delta n_{\max}}\right)(-2\nu_{13}S_{33} + S_{44}) \quad (5.10)$$

To obtain Young's modulus of an anisotropic glass, it is necessary to know the value of Δn_{\max} of the glass. However, because the Δn_{\max} of (Li,Na,K,Cs)PO₃ glass is not known, the value for KPO₃ crystal was used, which has a similar force constant of M–O bonds (0.11 N/cm) [15] to the average force constant (0.16 N/cm) [15] of M–O bonds in the (Li,Na,K,Cs)PO₃ glass. The distance between the –P–O–P– main chains of the crystal is expected to be similar to that in (Li,Na,K,Cs)PO₃ glass [4]. Therefore, it is assumed that Δn_{\max} is approximately 20000 nm/mm, which is the birefringence of the KPO₃ crystal. Using this value, the degree of orientation (F) of the anisotropic glass with a birefringence of 10600 nm/mm is estimated to be 0.53. The angle between the tensile direction and the direction of the chain axis, therefore, is estimated to be 34°. **Table 5.2** shows the values of E_H ($= 1/S_{33}$), E_L ($= 1/S_{11}$), and G ($= 1/S_{44}$) calculated by fitting the measured data to Equation (5.10), assuming that ν_{13} of the anisotropic glass increases from 0.29 to 0.40 because the reported maximum Poisson's ratio of phosphate glass is about 0.40 [20].

Table 5.2 Calculated E_H , E_L , and G of (Li,Na,K,Cs)PO₃ glass fiber.

ν_{13}	E_H (GPa)	E_L (GPa)	G (GPa)
0.29	148	30	13
0.40	162	32	13

ν_{13} , E_H , E_L , and G ($=1/S_{44}$) are the Poisson's ratio, Young's modulus in parallel and perpendicular directions to the chain axis, and shear modulus, respectively. The ν_{13} is taken from **Table 5.1** and Ref. [20].

Figure 5.10 shows the fitting curves and measured Young's moduli. The fitting curves do not differ significantly even when ν_{13} is increased from 0.29 to 0.40.

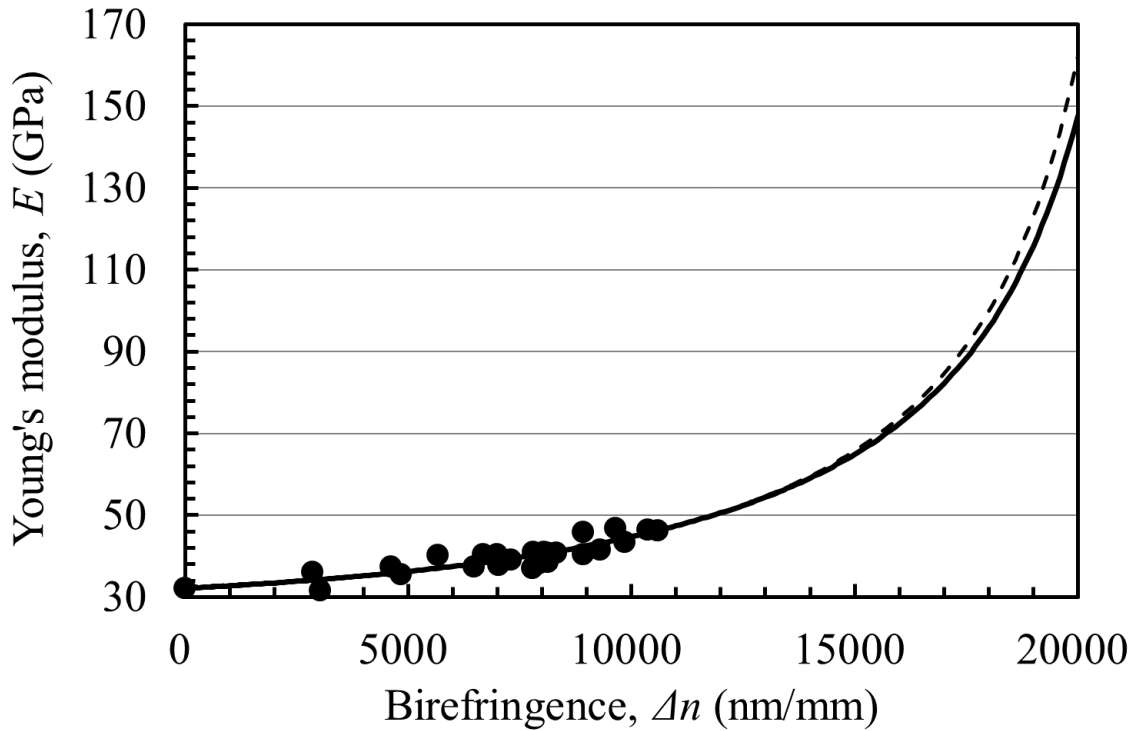


Fig. 5.10 Measured Young's moduli of (Li,Na,K,Cs)PO₃ glass fibers as a function of birefringence. The solid and dashed lines are the fitting curve calculated using Equation (5.10) where ν_{13} of the anisotropic glass is 0.29 and 0.40, respectively.

The calculated value of E_H is about five times larger than that of E_L . Consequently, anisotropic glass fibers with larger Δn have higher Young's moduli parallel to the fiber axis owing to the high degree of orientation of the $-P-O-P-$ chains with high E_H and low E_L corresponding to strong intrachain bonds and weak interchain bonds, respectively. This generates greater fracture strength in the direction parallel to the chain axis. If the degree of orientation of the $-P-O-P-$ main chains becomes higher than that of the anisotropic glass prepared in this test (i.e., if the birefringence exceeds 10600 nm/mm), further enhancement of the fracture strength and Young's modulus ($E = 1/S'_{33}$) is expected, as shown **Figure 5.10**.

In addition, as the difference between Young's moduli parallel and perpendicular to the tensile

direction increases, crack propagation becomes difficult because of the high frequency of deflection and branching of cracks during propagation. This phenomenon contributes to the high fracture strength of the anisotropic glasses.

However, the increase in fracture strength is still larger than the increase in Young's modulus as shown in **Fig. 5.7**. This means that the changes in the Poisson's ratio and crack length also take place and contribute to the increase in the fracture strength, as estimated from Equation (5.6). Assuming that the Poisson's ratio changes from 0.29 to 0.40, this accounts for only about 4% of the fracture strength increase. Changes in crack length, therefore, are deduced to be another predominant factor that causes the increase in fracture strength. **Table 5.3** shows the calculated fracture toughness, fracture surface energy, and crack length determined from Equation (5.6) when the Poisson's ratio of the anisotropic glass changes from 0.29 to 0.40. Fracture toughness was calculated under the assumption that fracture toughness (K_{Ic}) is equal to indentation fracture toughness (K_c). The calculated crack length of the anisotropic glass with a birefringence of 10600 nm/mm is about 30% shorter than that of isotropic glass. The higher degree of orientation of the –P–O–P– chain leads to the shorter crack length. Larger surface free energy (γ) of the anisotropic glass compared to the isotropic glass results from an increase in the difficulty of propagation of cracks in the direction perpendicular to the length direction of the glass due to orientation of the –P–O–P– chain (**Fig. 5.11**).

Table 5.3 Calculated properties of isotropic and anisotropic ($\Delta n = 10600$ nm/mm) (Li,Na,K,Cs)PO₃ glass fibers

	ν	K_{Ic} (MPa·m ^{1/2})	γ (J/m ²)	c
Anisotropic glass	0.29	0.63	3.9	$0.65c_{iso}$
	0.40	0.65	3.9	$0.71c_{iso}$
Isotropic glass	0.29 [†]	0.46 [†]	2.9 [†]	c_{iso}

ν , K_{Ic} , γ , and c are the Poisson's ratio, fracture toughness, fracture surface energy, and crack length, respectively. c_{iso} is the original crack length of the isotropic glass. The properties were calculated under the assumption that the properties of isotropic glass fiber are equal to those of bulk isotropic glass.

[†]The values experimentally obtained are shown for the bulk isotropic glass.

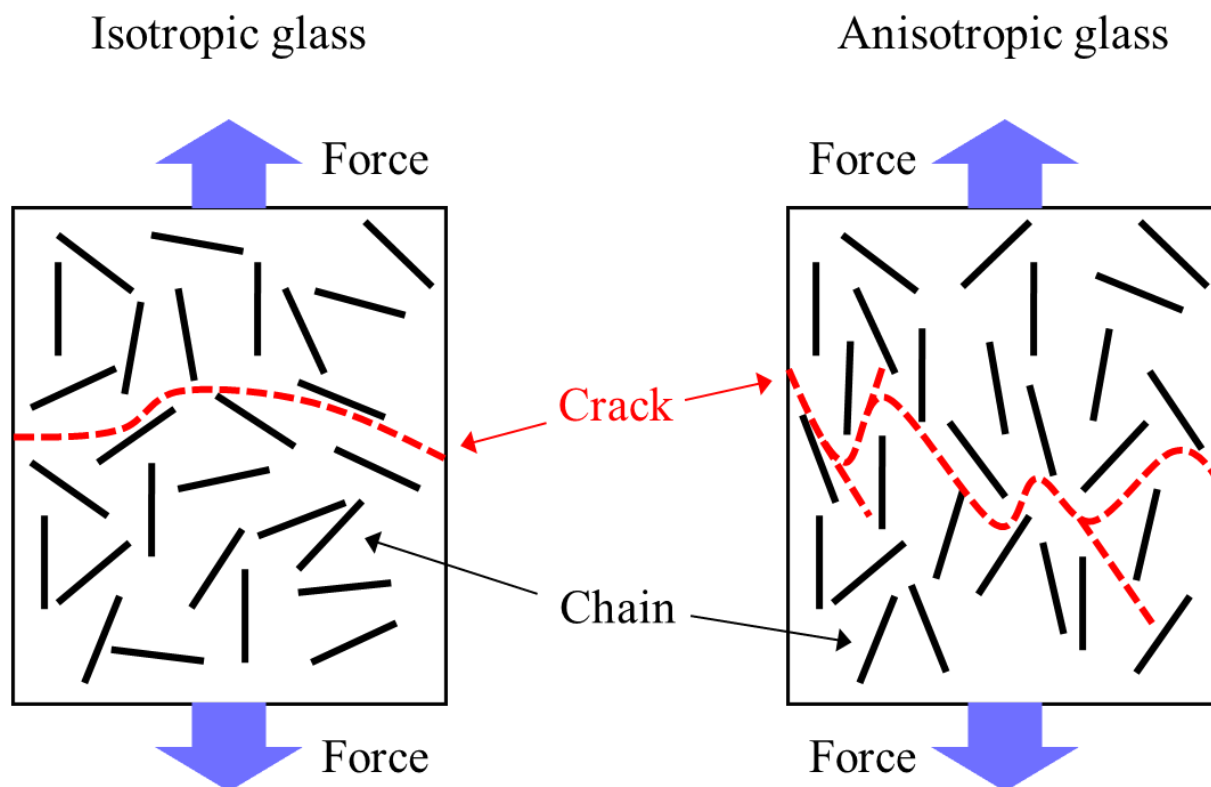


Fig. 5.11 Crack propagation of isotropic and anisotropic glasses during application of external force

5.5 Conclusions

The effect of anisotropy of a $12.5\text{Li}_2\text{O}-12.5\text{Na}_2\text{O}-12.5\text{K}_2\text{O}-12.5\text{Cs}_2\text{O}-50\text{P}_2\text{O}_5$ (mol%) glass fiber on its mechanical properties was investigated. It was found that the fracture strength and Young's modulus parallel to the fiber axis increased with increasing birefringence (i.e., increasing anisotropy) reaching 160% and 140% of the respective values of isotropic glass. The main reason for the enhancement in fracture strength is the increase in Young's modulus. Since the force constant of the P–O bond is larger by more than one order of magnitude than those of M–O bonds, Young's modulus parallel to the fiber axis increases with increasing orientation of the –P–O–P– main chains. The increase in chain orientation leads to a higher frequency of deflecting and branching of cracks during propagation, which contributes to the increased fracture strength. Furthermore, changes in other factors, such as the Poisson's ratio and crack length, also contribute to the increased fracture strength.

References

1. R. Schellekens and C. Bastiaansen, The drawing behavior of polyvinylalcohol fibers, *J. Appl. Polym. Sci.* **43** 2311–2315 (1991).
2. P. Smith and P. J. Lemstra, Ultra-high-strength polyethylene filaments by solution spinning/drawing, *J. Mater. Sci.* **15** 505–514 (1980).
3. H. Stockhorst and R. Brückner, Structure sensitive measurements on phosphate glass fibers, *J. Non-*

- Cryst. Solids **85** 105–126 (1986).
4. S. Inaba, H. Hosono, and S. Ito, Entropic shrinkage of an oxide glass, *Nat. Mater.* **14** 312–317 (2015).
 5. T. Miyoshi, N. Sagawa, and T. Sassa, A study on evaluation of K_{Ic} for structural ceramics, *Trans. Jpn. Soc. Mech. Eng., Ser. A.* **51A** 2489–2497 (1985).
 6. F. Muñoz, O. Pritula, J. Sedláček, and C. Rüssel, A study on the anisotropy of phosphate glass fibres, *Eur. J. Glass Sci. Technol. Part A: Glass Technol.* **49** 47–52 (2008).
 7. R. Brückner, J. Murach, and S. Hao, Generation and relaxation of flow birefringence of high-viscous alkali phosphate glass melts, *J. Non-Cryst. Solids* **208** 228–236 (1996).
 8. M. Ashizuka and R. C. Bradt, Fracture toughness of metaphosphate glasses, *J. Am. Ceram. Soc.* **65** C-70 (1982).
 9. Y. Yue, G. Carl, and C. Rüssel, Rheological properties of calcium metaphosphate melts during extrusion, *Glastech. Ber. Glass Sci. Technol.* **72** 67–75 (1999).
 10. Y. Yue, C. Rüssel, G. Carl, M. Braun, and C. Jäger, Structural order of extruded calcium metaphosphate glasses, *Phys. Chem. Glasses* **41** 12–16 (2000).
 11. M. Braun, Y. Yue, C. Rüssel, and C. Jäger, Two-dimensional nuclear magnetic resonance evidence for structural order in extruded phosphate glasses, *J. Non-Cryst. Solids* **241** 204–207 (1998).
 12. A. A. Griffith, The phenomena of rupture and flow in solids, *Philos. Trans. R. Soc. London, A* **221** 163–198 (1920).
 13. G. R. Irwin, Analysis of stresses and strains near the end of a crack traversing a plate, *J. Appl. Mech.* **24** 361–364 (1957).
 14. N. Shinkai, R. C. Bradt, and G. E. Rindone, Elastic modulus and fracture toughness of ternary PbO–ZnO–B₂O₃ glasses, *J. Am. Ceram. Soc.* **65** 123–126 (1982).
 15. G. J. Exarhos, P. J. Miller, and W. M. Risen, Interionic vibrations and glass transitions in ionic oxide metaphosphate glasses, *J. Chem. Phys.* **60** 4145–4155 (1974).
 16. J. Wong and C. A. Angell, Application of spectroscopy in the study of glassy solids, Part II. Infrared, Raman, EPR, and NMR spectral studies, *Appl. Spectrosc. Rev.* **4** 155–232 (1971).
 17. K. Meyer, Characterization of the structure of binary zinc ultraphosphate glasses by infrared and Raman spectroscopy, *J. Non-Cryst. Solids* **209** 227–239 (1997).
 18. S. R. Allen, E. J. Roche, B. Bennett, and R. Molaison, Tensile deformation and failure of poly (p-phenylene terephthalamide) fibers, *Polymer* **33** 1849–1854 (1992).
 19. I. M. Ward and J. Sweeney, *Mechanical properties of solid polymers*, Wiley (2012).
 20. L. Börjesson, S. W. Martin, L. M. Torell, and C. A. Angell, Brillouin scattering in AgI rich glasses, *Solid State Ion.* **18–19** 431–436 (1986).

Chapter 6: Summary and Conclusions

Formation of anisotropic structure in oxide glasses is typically difficult even if an external force is applied to oxide glasses above the glass transition temperature (T_g) due to three-dimensional network structures. However, 16.7Li₂O–16.7Na₂O–16.7K₂O–50P₂O₅ (mol%, (Li,Na,K)PO₃) and 12.5Li₂O–12.5Na₂O–12.5K₂O–12.5Cs₂O–50P₂O₅ (mol%, (Li,Na,K,Cs)PO₃) mixed alkali metaphosphate glasses composed of –P–O–P– chains formed by Q² units recently were found to show significant anisotropy when uniaxial tensile stress is applied to the glasses above T_g due to formation of highly oriented –P–O–P– chains. The objective of this thesis is the clarification of important structural factors for the formation of significant anisotropy above T_g and the effect of the anisotropic structures on the mechanical properties of alkali metaphosphate glasses for the development of new anisotropic oxide glasses with new properties not reported in oxide glasses and new methods to improve mechanical properties of oxide glasses.

In chapter 2, the structural features causing the formation of the significant anisotropic structure in (Li,Na,K)PO₃ glass were investigated by analyzing ³¹P MAS NMR, Raman, and FTIR spectra. Results of the analysis are summarized in **Table 6.1**. Although the birefringence of (Li,Na,K)PO₃ glass elongated above T_g is much larger than that of 50Na₂O–50P₂O₅ (mol%, NaPO₃) glass elongated above T_g , only T_g and Δ_{PW} notably differ between NaPO₃ and (Li,Na,K)PO₃ glasses. According to Gibbs-DiMarzio theory, the flexibility of chain for (Li,Na,K)PO₃ glass is higher than that for NaPO₃ glass because (A) T_g of (Li,Na,K)PO₃ glass (222°C) is lower than that of NaPO₃ glass (292°C) and (B) average F_{M-O} of (Li,Na,K)PO₃ glass is equivalent to that of NaPO₃ glass. The distribution of F_{M-O} and highly flexible chains for (Li,Na,K)PO₃ glass, therefore, are important factors for the formation of significant anisotropy during deformation of the glass under uniaxial tensile stress above T_g . Formation of the significant anisotropic structure of (Li,Na,K)PO₃ glass under uniaxial tensile stress above T_g results from orientation of highly flexible local structures with small F_{M-O} during the suppression of shear flow between chains by local structures with large F_{M-O} as shown in **Fig. 6.1**. The results support the adequacy of the model of the orientation of chains of (Li,Na,K,Cs)PO₃ glass under uniaxial tensile stress above T_g proposed by Inaba et al.

Table 6.1 Birefringence, T_g , average force constant between alkali cation and oxygen (F_{M-O}), the difference of peak wavenumbers between a peak originated from Li–O motion and a peak observed below 300 cm^{-1} (Δ_{PW}), the relative fraction of Q^2 units, and relative fraction of Q^2 units in chains to total Q^2 units (A_R) for LiPO_3 , NaPO_3 , $(\text{Li,Na})\text{PO}_3$, and $(\text{Li,Na,K})\text{PO}_3$ metaphosphate glasses.

		LiPO_3	NaPO_3	$(\text{Li,Na})\text{PO}_3$	$(\text{Li,Na,K})\text{PO}_3$
Birefringence (nm/mm)	Glass fiber elongated at tensile stress of 40MPa above T_g	39	233	519	1679
T_g ($^{\circ}\text{C}$)		334	292	251	222
Average F_{M-O} (N/cm)		0.269	0.177	0.223	0.186
Δ_{PW} (cm^{-1})	Absorption coefficient spectra in the range 100–600 cm^{-1}	0	0	192	210
Relative fraction of Q^2 units (%)	^{31}P MAS NMR Spectra	96.6	100 (no detectable Q^1 peak)	97.3	98.7
A_R (%)	Raman spectra in the range 600–850 cm^{-1}	21	36	28	36
A_R (%)	Raman spectra in the range 1050–1250 cm^{-1}	37	48	42	48
A_R (%)	Absorption coefficient spectra in the range 800–1400 cm^{-1}	13	28	20	27

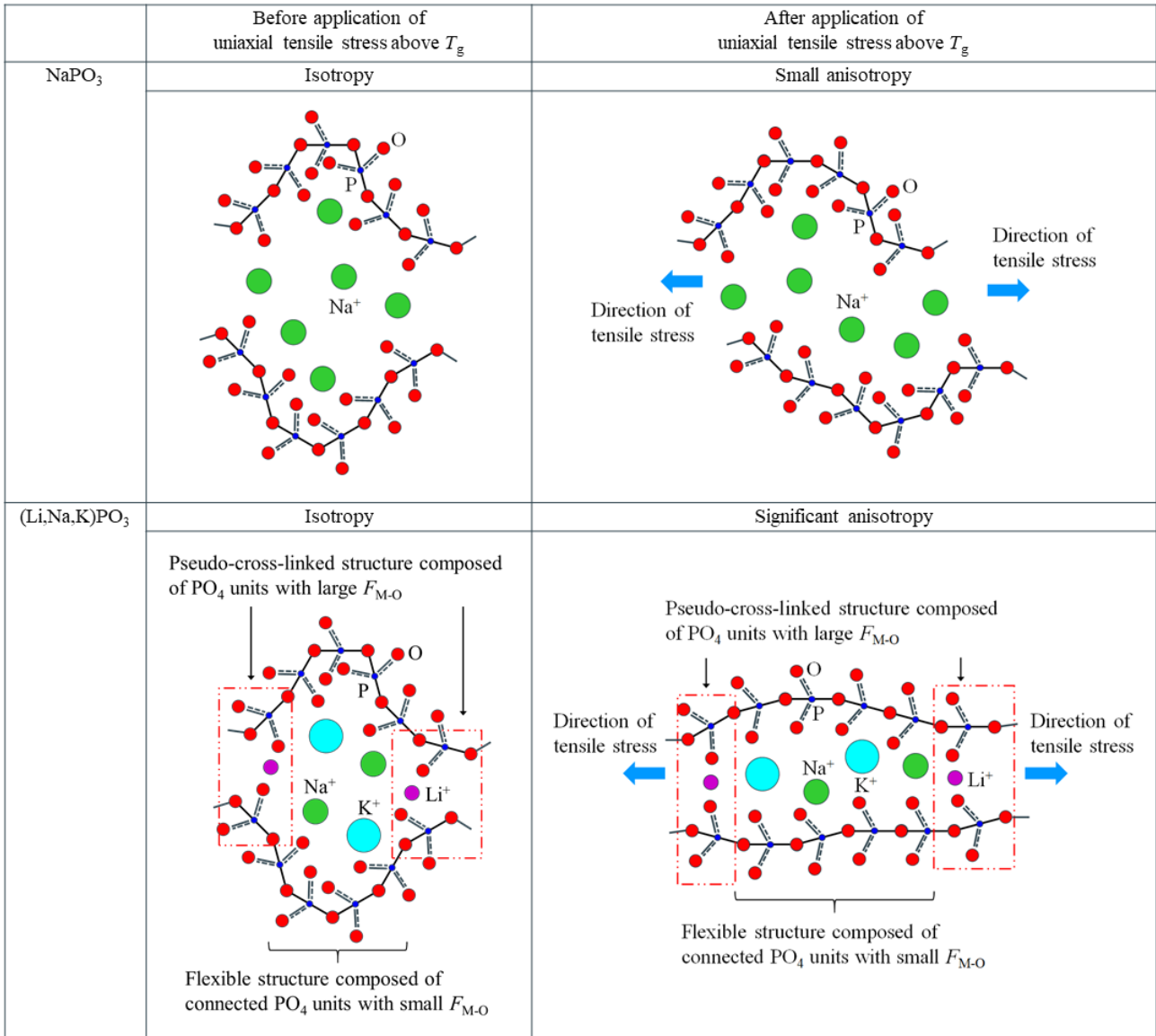


Fig. 6.1 Schematic illustration of chain structures for NaPO_3 and $(\text{Li,Na,K})\text{PO}_3$ glasses. Small deep blue, middle-sized red, middle-sized purple, large green, and large light blue circles represent phosphorus, oxygen, lithium cation, sodium cation, and potassium cation, respectively.

In chapter 3, the relaxation mechanism of anisotropic $(\text{Li,Na,K,Cs})\text{PO}_3$ glass in the range from room temperature to above T_g were investigated by evaluating storage moduli (E') and loss factors ($\tan\delta$) and analyzing Raman spectra in the range from room temperature to above T_g . The results showed that relaxation mechanisms of anisotropic $(\text{Li,Na,K,Cs})\text{PO}_3$ glass were a partial loss of cross-linking between the oriented chains below T_g and a disordering of the oriented chain above T_g as shown in **Fig. 6.2**. The coexistence of local structures with $F_{\text{M-O}}$ smaller than $F_{\text{threshold}}$ and local structures with $F_{\text{M-O}}$ larger than $F_{\text{threshold}}$ was play an important role in the unique relaxation of anisotropic $(\text{Li,Na,K,Cs})\text{PO}_3$ glass. The results support the adequacy of the model of relaxation of oriented chains in anisotropic $(\text{Li,Na,K,Cs})\text{PO}_3$ glass above T_g proposed by Inaba et al.

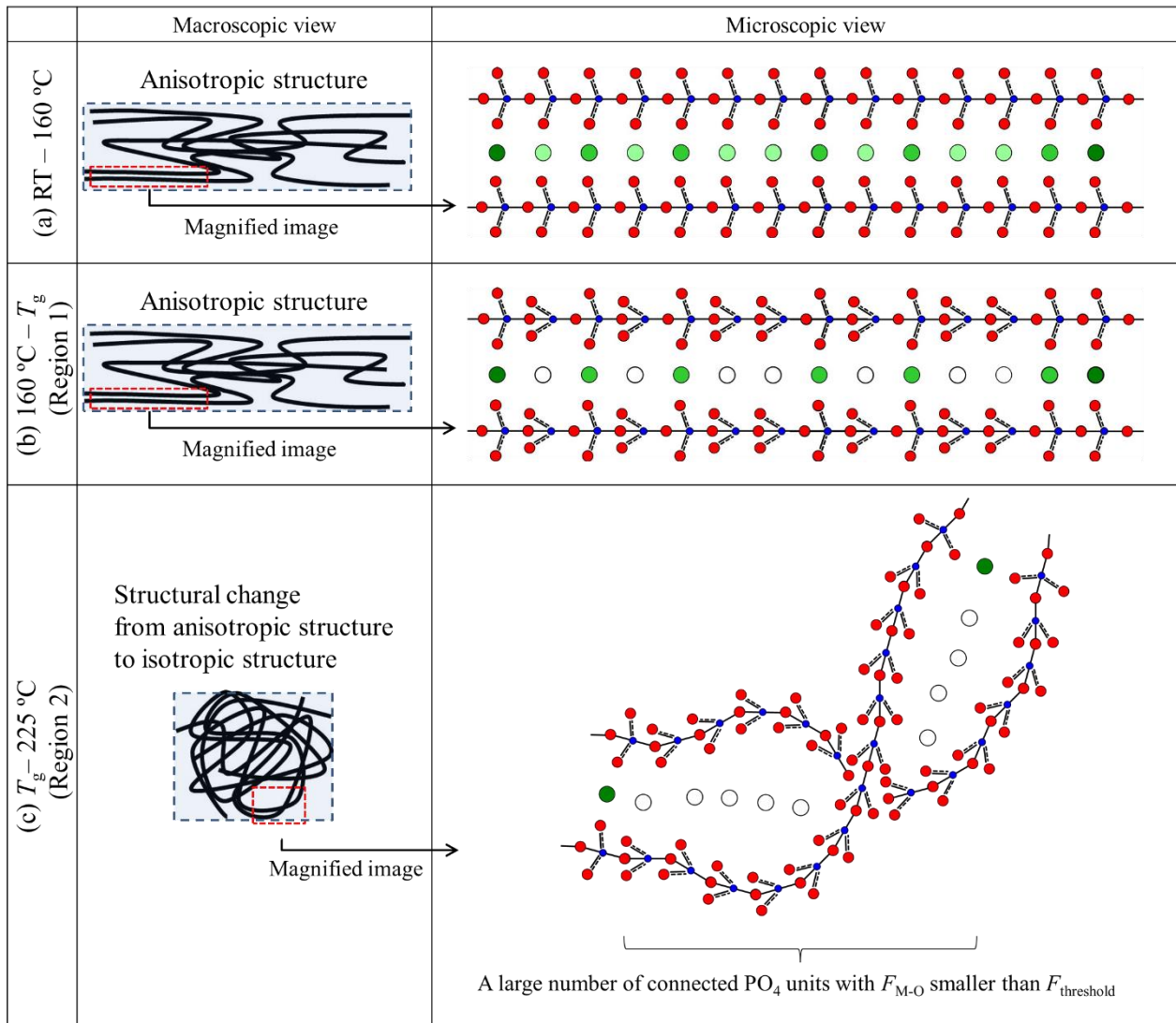


Fig. 6.2 Schematic illustrations of chain structures for anisotropic (Li,Na,K,Cs)PO₃ glass. Blue squares and black lines in the macroscopic view represent the shape of the glass and –P–O–P– chains. Darker green circles represent alkali cations with higher F_{M-O} . Large open circles represent alkali cations with F_{M-O} smaller than the $F_{threshold}$.

In chapter 4, the deformation behaviors of (Li,Na,K,Cs)PO₃ glass under compressive stress above T_g were investigated. (Li,Na,K,Cs)PO₃ glass uniaxially compressed above T_g and then rapidly cooled to room temperature showed a large recovery in length during reheating above T_g (**Fig. 6.3**). The viscoelastic–plastic behavior of (Li,Na,K,Cs)PO₃ glass was investigated by depth-sensing indentation. The (Li,Na,K,Cs)PO₃ glass showed a large recovery in penetration depth during unloading above T_g (**Fig. 6.4**). By analyzing the P – h curves with the viscous–elastic–plastic model, the unusually large recovery of (Li,Na,K,Cs)PO₃ glass is found to be due to a smaller and larger contribution of, respectively, viscous and elastic deformations (**Fig. 6.5**). The large recovery in the length of the compressed (Li,Na,K,Cs)PO₃ glass, therefore, results from a large contribution ratio of elastic deformation due to the orientation and relaxation of chains (**Fig. 6.6**).

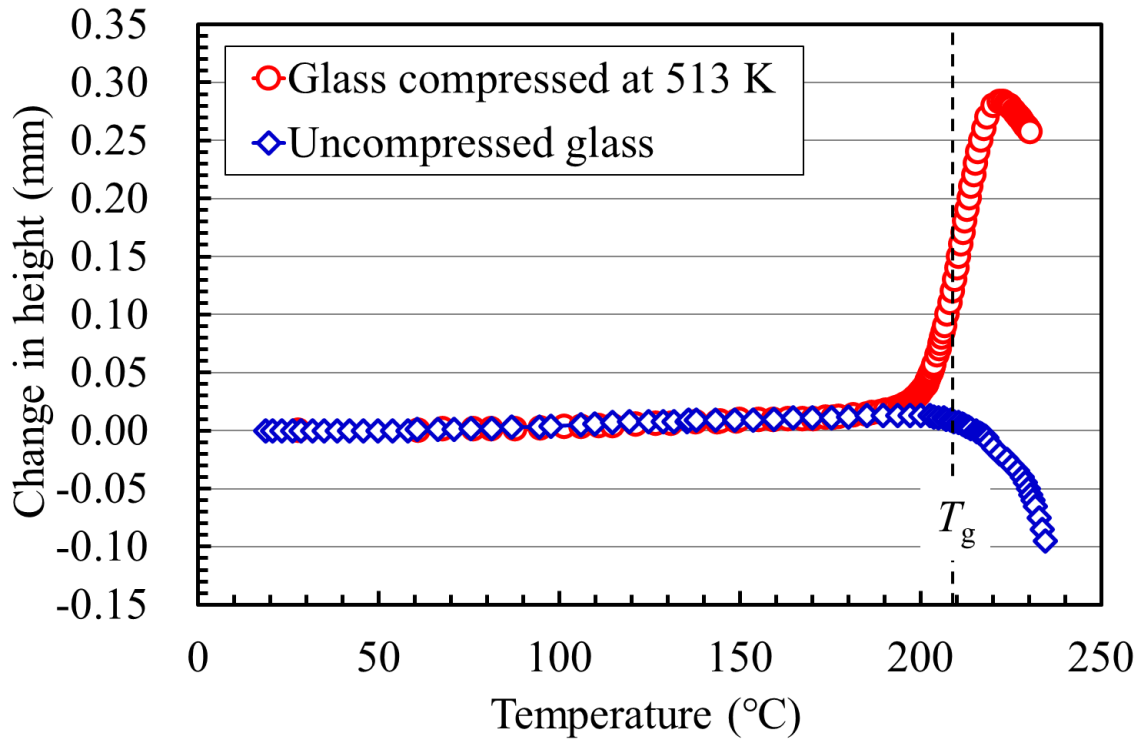


Fig. 6.3 Change in the height of (Li,Na,K,Cs)PO₃ glass compressed at 513 K and uncompressed (Li,Na,K,Cs)PO₃ glass during heating.

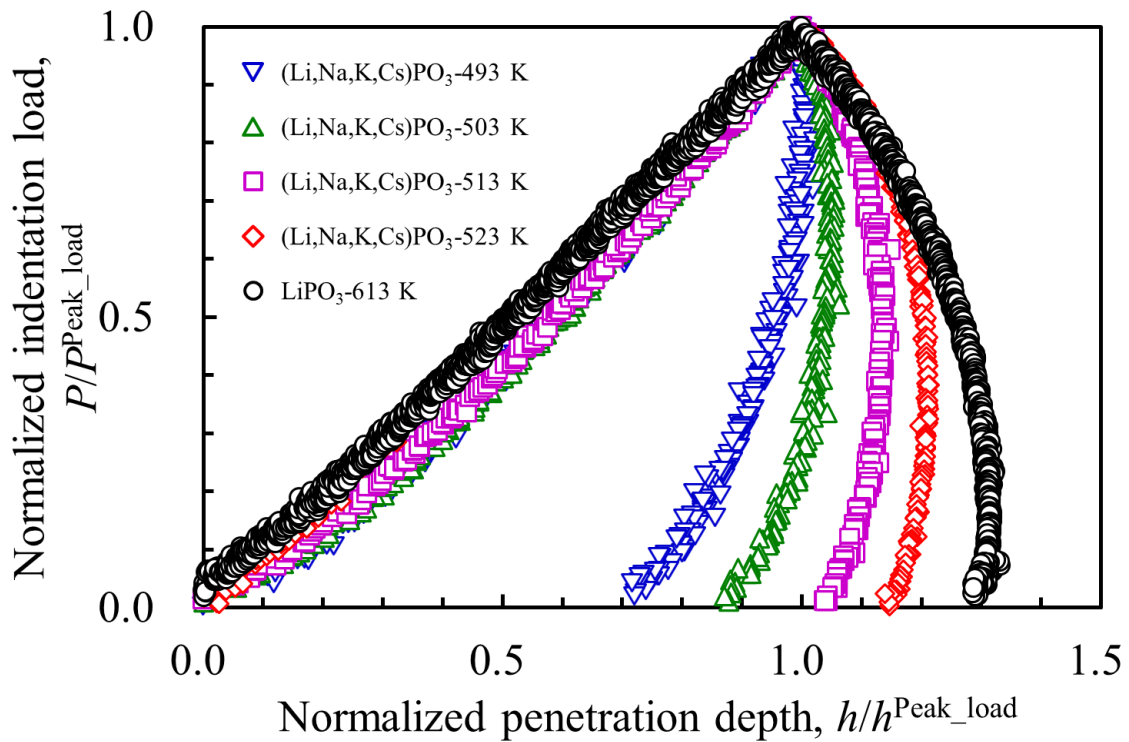


Fig. 6.4 Normalized load–displacement curves of (Li,Na,K,Cs)PO₃ glass at 493, 503, 513, and 523 K ($T/T_g = 1.02, 1.04, 1.06, \text{ and } 1.09$), and LiPO₃ glass at 613 K ($T/T_g = 1.01$).

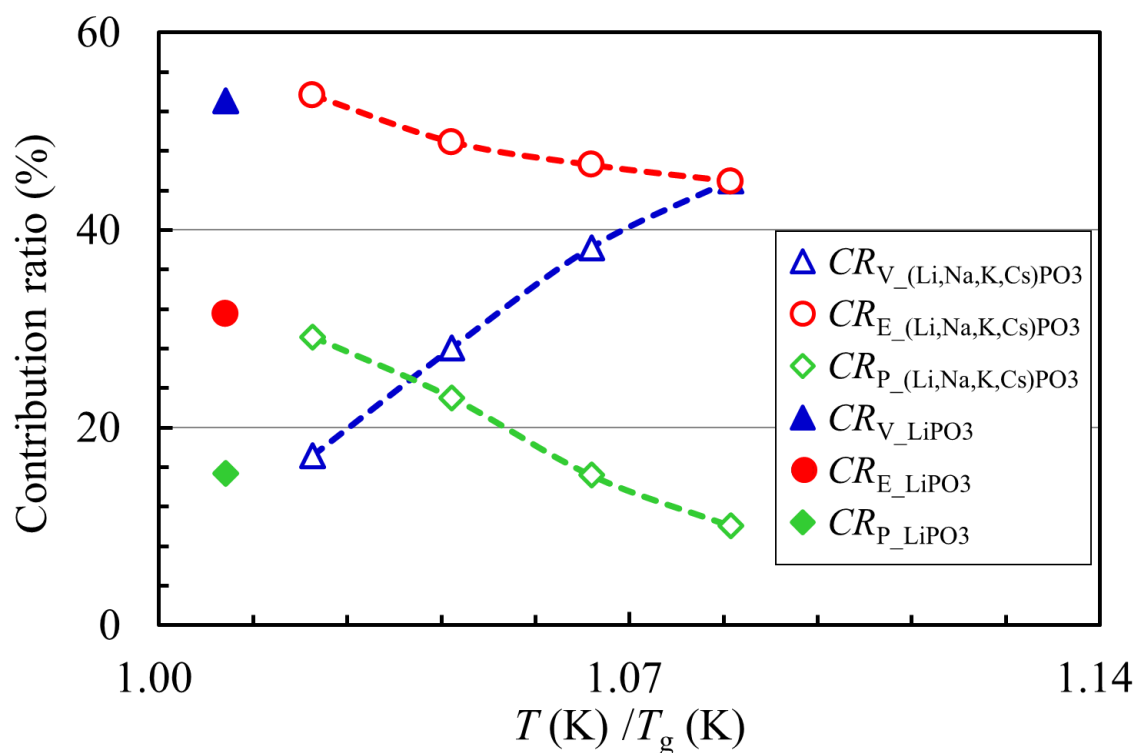


Fig. 6.5 Temperature (T/T_g) dependence of the contribution ratios of viscous ($CR_{V_{(Li,Na,K,Cs)PO_3}}$), elastic ($CR_{E_{(Li,Na,K,Cs)PO_3}}$), and plastic ($CR_{P_{(Li,Na,K,Cs)PO_3}}$) deformation of $(Li,Na,K,Cs)PO_3$ glass, and the contribution ratios of viscous ($CR_{V_{LiPO_3}}$), elastic ($CR_{E_{LiPO_3}}$), and plastic ($CR_{P_{LiPO_3}}$) deformation of $LiPO_3$ glass.

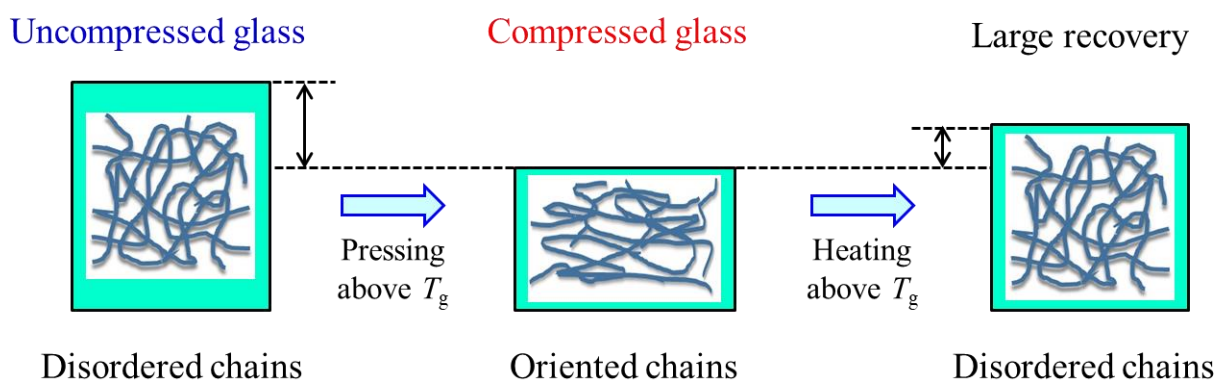


Fig. 6.6 Shape deformation of the columnar sample of $(Li,Na,K,Cs)PO_3$ glass, and orientation and relaxation of chains of $(Li,Na,K,Cs)PO_3$ glass.

In chapter 5, the effects of the anisotropic structures of $(Li,Na,K,Cs)PO_3$ glass fibers on fracture strength and Young's modulus were investigated by measuring stress-strain curves of the glass fibers with a three-point bending method. The results showed that fracture strength and Young's modulus for $(Li,Na,K,Cs)PO_3$ glass fibers increased with increasing birefringence (**Fig. 6.7**). The increase in Young's modulus was caused by the increase in the degree of orientation of $-P-O-P-$ chains in the parallel direction to the length direction of fibers (**Fig. 6.8**). The increase in fracture strength resulted from the increase in

Young's modulus. The results showed that the formation of anisotropic structure in oxide glasses becomes a new method to improve fracture strength and Young's modulus of oxide glasses.

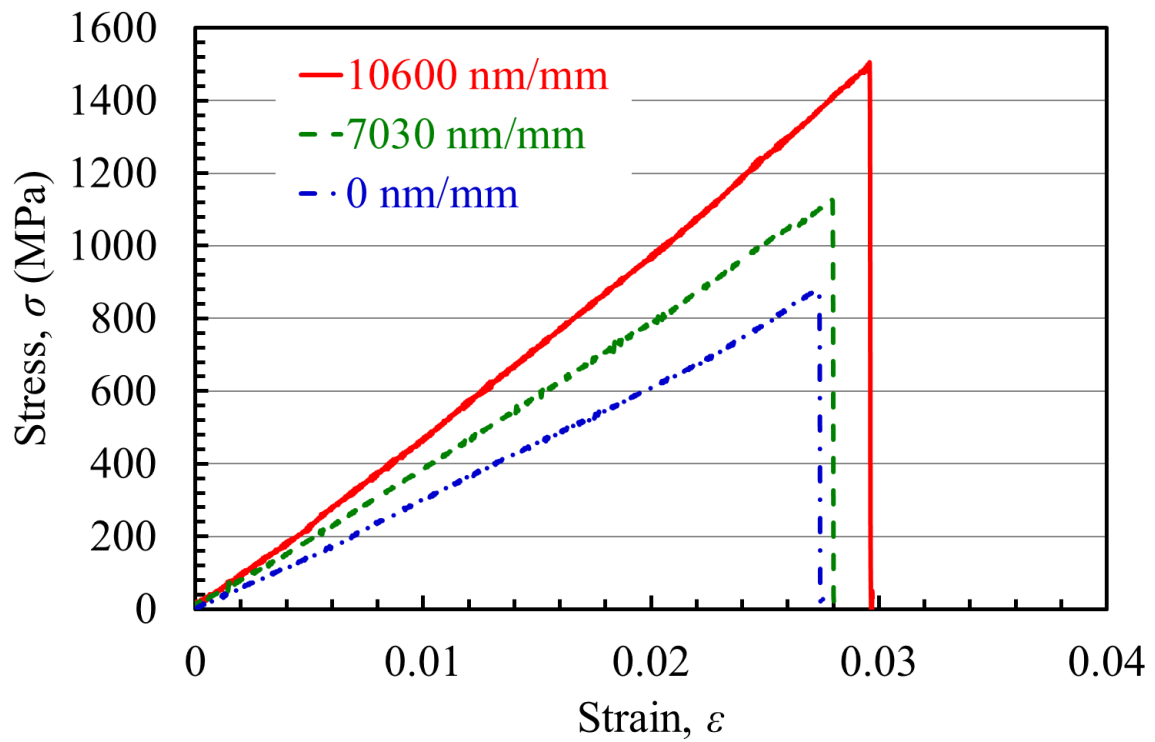


Fig. 6.7 Stress–strain curves of (Li,Na,K,Cs)PO₃ glass fibers.

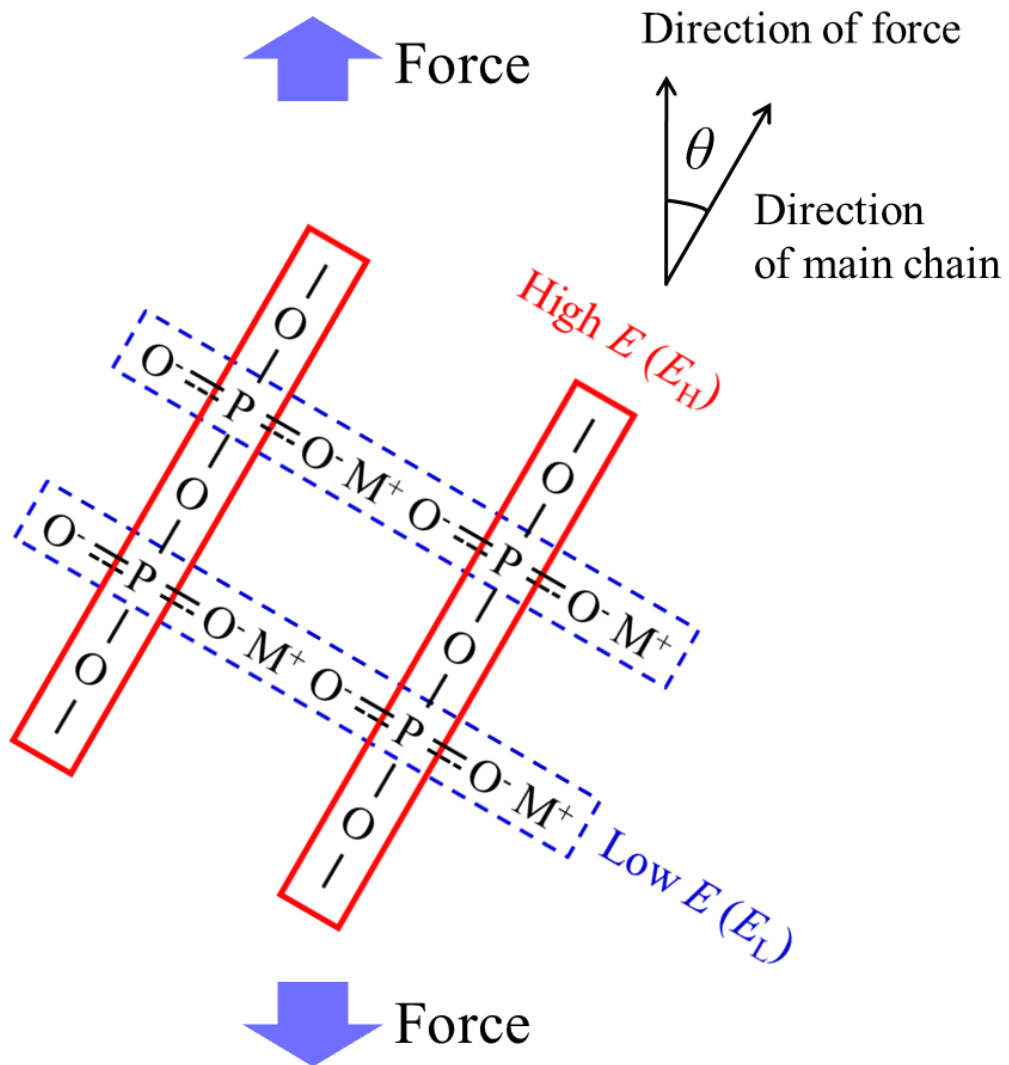


Fig. 6.8 Schematic illustration of the chain structure of $(\text{Li,Na,K,Cs})\text{PO}_3$ glass. Alkali cations are represented as M^+ . E_H and E_L are Young's moduli in the parallel and perpendicular directions to the chain axis, respectively.

Achievements

List of publications

1. **Jun Endo**, Seiji Inaba, Osamu Homma, and Yoshikazu Suzuki, Structural features of (Li,Na,K)PO₃ mixed alkali metaphosphate glass for significant anisotropy, *Journal of the American Ceramic Society* **105** 217–224, 758–759 (2022), DOI:10.1111/jace.18063, DOI:10.1111/jace.18137.
2. **Jun Endo** and Yoshikazu Suzuki, Reassessment of vibration spectra in alkali phosphate crystals, *Journal of the Ceramic Society of Japan*. (in press)
3. **Jun Endo**, Seiji Inaba, and Setsuro Ito, Relaxation of anisotropic alkali metaphosphate glass, *Materials Letters* **283** 128762 (2021), DOI:10.1016/j.matlet.2020.128762.
4. **Jun Endo**, Seiji Inaba, Hiroyuki Muto, and Setsuro Ito, Unusual indentation behavior of alkali metaphosphate glass above glass transition temperature, *Journal of the American Ceramic Society* **100** 81–85 (2017), DOI:10.1111/jace.14489.
5. **Jun Endo**, Seiji Inaba, and Setsuro Ito, Mechanical properties of anisotropic metaphosphate glass, *Journal of the American Ceramic Society* **98** 2767–2771 (2015), DOI:10.1111/jace.13682.

Conference

International

1. **Jun Endo**, Seiji Inaba, and Setsuro Ito, Anisotropy and mechanical property of metaphosphate glass, The 10th Pacific Rim Conference on Ceramic and Glass Technology (PACRIM 10), San Diego, California, USA (June 2013) (Oral).
2. **Jun Endo**, Seiji Inaba, Hiroyuki Muto, and Setsuro Ito, Large elastic recovery during indentation of alkali metaphosphate glass above glass transition, The 12th Pacific Rim Conference on Ceramic and Glass Technology (PACRIM 12), Waikoloa, Hawaii, USA (May 2017) (Oral).
3. **Jun Endo** and Yoshikazu Suzuki, Reassessment of peak assignment of vibrational spectra for alkali phosphate crystals, The 9th Advanced Functional Materials & Devices and the 4th Symposium for Collaborative Research on Energy Science and Technology, Online (March 2022)

Domestic

1. **Jun Endo**, Seiji Inaba, and Setsuro Ito, Mechanical properties and structure of anisotropic alkali metaphosphate glass, The 54th symposium on glass and photonics materials, Ikeda, Osaka, Japan (November 2013) (Oral).
2. **Jun Endo**, Seiji Inaba, Osamu Homma, and Yoshikazu Suzuki, Structural key factors for formation of significant anisotropy of alkali metaphosphate glass, The 60th symposium on basic science of ceramics, Kumamoto, Kumamoto, Japan (January 2022) (Oral).

Acknowledgment

The author would like to show my greatest appreciation to my supervisor Associate Professor Yoshikazu Suzuki in the Faculty of Pure and Applied Sciences at the Graduate School of Pure and Applied Sciences, the University of Tsukuba for his generous help and excellent guidance in coordinating this study. The author would like to deeply appreciate Professor Kiyoto Matsuishi and Professor Kim Heeyoung in the Faculty of Pure and Applied Sciences at the Graduate School of Pure and Applied Sciences, the University of Tsukuba, and Principal Researcher Hiroyo Segawa in the Electroceramics Group, the National Institute for Materials Science (NIMS) for reviewing this thesis and their helpful suggestion.

The author would like to express sincere gratitude to Professor Hiroyuki Muto at the Institute of Liberal Arts and Science, the Toyohashi University of Technology for collaboration on the evaluation of deformation behaviors of alkali metaphosphate glasses with a Berkovich indenter and his fruitful suggestions.

The author is sincerely grateful to former Technical Advisor Setsuro Ito and Principal Researcher Seiji Inaba of AGC Inc. for their great and kind guidance and cooperation in this study. The author deeply acknowledges Principal Researcher Tatsuya Miyajima and Senior Researcher Osamu Homma of AGC Inc. for their cooperation and great support of the measurement and analysis of the NMR, Raman, and FTIR spectra.

The author would like to express my heartfelt gratitude to everyone who supported this study.

The author acknowledges members of Yoshikazu Suzuki Laboratory for their kind support.

The author appreciates my family for their hearty support and understanding.

Jun Endo

February 2022

Tsukuba, Japan